

ADVERTIMENT. La consulta d'aquesta tesi queda condicionada a l'acceptació de les següents condicions d'ús: La difusió d'aquesta tesi per mitjà del servei TDX (www.tesisenxarxa.net) ha estat autoritzada pels titulars dels drets de propietat intel·lectual únicament per a usos privats emmarcats en activitats d'investigació i docència. No s'autoritza la seva reproducció amb finalitats de lucre ni la seva difusió i posada a disposició des d'un lloc aliè al servei TDX. No s'autoritza la presentació del seu contingut en una finestra o marc aliè a TDX (framing). Aquesta reserva de drets afecta tant al resum de presentació de la tesi com als seus continguts. En la utilització o cita de parts de la tesi és obligat indicar el nom de la persona autora.

ADVERTENCIA. La consulta de esta tesis queda condicionada a la aceptación de las siguientes condiciones de uso: La difusión de esta tesis por medio del servicio TDR (www.tesisenred.net) ha sido autorizada por los titulares de los derechos de propiedad intelectual únicamente para usos privados enmarcados en actividades de investigación y docencia. No se autoriza su reproducción con finalidades de lucro ni su difusión y puesta a disposición desde un sitio ajeno al servicio TDR. No se autoriza la presentación de su contenido en una ventana o marco ajeno a TDR (framing). Esta reserva de derechos afecta tanto al resumen de presentación de la tesis como a sus contenidos. En la utilización o cita de partes de la tesis es obligado indicar el nombre de la persona autora.

WARNING. On having consulted this thesis you're accepting the following use conditions: Spreading this thesis by the TDX (www.tesisenxarxa.net) service has been authorized by the titular of the intellectual property rights only for private uses placed in investigation and teaching activities. Reproduction with lucrative aims is not authorized neither its spreading and availability from a site foreign to the TDX service. Introducing its content in a window or frame foreign to the TDX service is not authorized (framing). This rights affect to the presentation summary of the thesis as well as to its contents. In the using or citation of parts of the thesis it's obliged to indicate the name of the author

UNIVERSITAT POLITÈCNICA DE CATALUNYA

DEPARTAMENT D'ENGINYERIA ELÈCTRICA



Departament d'Enginyeria Elèctrica



UNIVERSITAT POLITÈCNICA DE CATALUNYA



CITCEA - Centre d'Innovació Tecnològica
en Convertidors Estàtics i Accionaments

PhD Thesis

Control of power electronic converters for the operation of wind generation systems under grid disturbances

Author: **Adrià Junyent-Ferré**

Adviser: **Oriol Gomis-Bellmunt**

Barcelona, May 2011

Universitat Politècnica de Catalunya
Departament d’Enginyeria Elèctrica
Centre d’Innovació Tecnològica en Convertidors Estàtics i Accionaments
Av. Diagonal, 647. Pl. 2
08028 Barcelona

Copyright © Adrià Junyent-Ferré, 2011

Primera impressió, Juny 2011

ACTA DE QUALIFICACIÓ DE LA TESI DOCTORAL

Reunit el tribunal integrat pels sota signants per jutjar la tesi doctoral:

Títol de la tesi:

Autor de la tesi:

Acorda atorgar la qualificació de:

- ☐ No apte
- ☐ Aprovat
- ☐ Notable
- ☐ Excel·lent
- ☐ Excel·lent Cum Laude

Barcelona, de/d' de

El President

El Secretari

.....
(nom i cognoms)

.....
(nom i cognoms)

El vocal

El vocal

El vocal

.....
(nom i cognoms)

.....
(nom i cognoms)

.....
(nom i cognoms)

Acknowledgements

The present work was developed in the CITCEA-UPC¹, where I have had the privilege to work since November 2006, and the Control and Power Research Group (C&P) of the Imperial College London, during a research stay from July to October 2010. This thesis was carried out with the support of the *Ministerio de Ciencia e Innovación* under the project ENE2009-08555. Most of the work presented here is also motivated by four years of fruitful collaboration with Alstom Wind formerly Ecotènia s.coop.

I am indebted to a number of people whose help has made it possible to complete this thesis. My adviser, Dr. Oriol Gomis, has always been ready to give me good technical and personal advice. My colleagues from CITCEA have created a really enjoyable and inspiring work atmosphere. I am grateful to Agustí, Edu, Mònica and Yong with whom I feel lucky to work. Professor Tim Green gave me the chance to be in the C&P group and supervised my work along with Dr. Diego Soto. I thank them for sharing their knowledge with me and for always being open for inspiring technical discussion.

I would also like to thank the people from my environment who have been an invaluable source of inspiration. My mother Núria and my grandparents Antonio and Cari have always cared for me and their example taught me to enjoy learning, to embrace challenges and to work hard. Cristina, Paola and Eduard from whom I have learned a lot and have proven to care about me and help me whenever I need it. I also thank Jelena and Ms. Gica Gicic for caring so much about *мрдљива жежина*.

I gratefully thank many people for kindly helping me complete this work but any mistakes or inaccuracies in this thesis remain, of course, my responsibility.

A.J.F.

¹Centre d’Innovació en Tecnologia de Convertidors Estàtics i Accionaments de la Universitat Politècnica de Catalunya (CITCEA-UPC)

Abstract

The present PhD thesis analyzes the modelling and control of the two main topologies of large scale variable speed wind turbines, the doubly fed induction generator and the permanent magnet synchronous generator wind turbines, to operate under different types of voltage sags. The first part of the thesis deals with the modelling of the wind turbine from the mechanics to the different types of generators and the power converter. The second part deals with the control of the wind turbine. First, three different control schemes of the doubly fed induction machine are analyzed, starting with the most basic one, the conventional vector control meant for balanced operation which is simulated and compared to experimental measurements from a voltage sag test, and then moving to the dual synchronous reference frame and the stationary reference frame control, two different schemes that allow the operation of the machine under unbalanced voltage sags. Then, different reference calculation methods for the operation of grid connected voltage source converters under grid unbalances are analyzed and tested on a experimental platform. Finally, the vector control scheme of the permanent magnet synchronous generator and a ride-through strategy for this type of turbine for balanced voltage sags is presented and tested on a small scale experimental platform.

Resum

Aquesta tesi analitza la modelització i el control per a l'operació sota diferents tipus de sots de tensió de les dues topologies més comunes d'aerogeneradors de velocitat variable de gran escala, la basada en generador d'inducció doblement alimentat i la de màquina síncrona d'imants permanents. La primera part de la tesi tracta el modelat de la turbina eòlica des de la mecànica fins als diferents tipus de generadors i el convertidor. La segona part tracta el control de l'aerogenerador. Primer, s'analitzen tres esquemes de control diferents de la màquina d'inducció doblement alimentada, començant pel tipus més bàsic, el control vectorial convencional, pensat per l'operació en equilibri, que és simulat i comparat amb mesures experimentals d'un assaig de sot de tensió, i tractant a continuació l'anomenat control vectorial amb doble referència de sincronisme i el control en referència estacionària, dos esquemes de control diferents que permeten l'operació de la màquina sota sots de tensió desequilibrats. A continuació s'analitzen i comproven experimentalment diferents mètodes de càlcul de referències pel control de convertidors amb font de tensió sota desequilibris de xarxa. Finalment, es presenta l'esquema de control vectorial de màquina síncrona d'imants permanents i una estratègia de *ride-through* per a aquest tipus d'aerogenerador que és avaluada en una plataforma experimental.

Thesis outline

The present PhD thesis is divided in two parts plus an introductory chapter and a conclusion chapter: Part I is centered in the modelling and analysis of the characteristics of the different subsystems of a variable speed wind turbine and contains the Chapters 2, 3, 4 and 5. Part II deals with the control of the wind turbines for the operation under grid disturbances and contains Chapters 6, 7, 8, 9, 10 and 11.

Chapter 2 deals with the modelling of the mechanical subsystem of a variable speed wind turbine, the aerodynamic behaviour of the turbine, the drivetrain dynamics and a simplified speed control to optimize the energy extracted by the turbine.

Chapter 3 discusses the modelling of a doubly fed induction machine. First the dynamic equations of the machine are obtained and then steady state equations are obtained for balanced and unbalanced operating conditions.

Chapter 4 analyzes the modelling of a permanent magnet synchronous machine. First the dynamic equations of the machine are obtained and the steady state equations are derived from the dynamic ones.

Chapter 5 deals with the modelling of the back-to-back converter used in the topologies of doubly fed induction machine and permanent magnet synchronous machine variable speed wind turbines.

Chapter 6 describes and analyzes a conventional vector controller for the DFIG and the grid side of the converter and presents a model validation using existing measurement data from a real test performed on a large scale wind turbine.

Chapter 7 presents an extension of the conventional vector control for the DFIG and the grid side of the converter to operate under unbalanced conditions called the dual synchronous reference frame vector control.

Chapter 8 analyzes the use of the synchronous reference frame for the control of the DFIG and the grid side of the converter to operate under unbalanced conditions while solving some of the drawbacks of the dual synchronous reference frame vector control.

Chapter 9 presents different important problems of the existing current calculation methods for unbalanced operation of grid connected voltage source converters and possible work arounds for them while providing experimental

evaluation of the proposed solutions.

Chapter 10 describes the vector control of a permanent magnet synchronous generator-based wind turbine.

Chapter 11 presents a ride-through strategy for permanent magnet synchronous generator-based wind turbine which allows independent control of both sides of the converter while providing experimental verification of the proposed algorithm.

Finally the Chapter 12 summarizes the conclusions of the present thesis.

Contents

List of Figures	xiii
List of Tables	xix
Nomenclature	xxv
1 Introduction	1
I Modelling of wind turbines	5
2 Wind turbine mechanical system modelling	7
2.1 Introduction	7
2.2 Modeling of the wind turbine aerodynamics	7
2.3 Wind speed modelling	10
2.4 Drivetrain modelling	12
2.5 Wind turbine speed control	14
3 Induction machine modelling	21
3.1 Introduction	21
3.2 Induction machine dynamic equations	21
3.3 Steady state analysis for balanced operation	28
3.3.1 Steady state current reference calculation	31
3.4 Steady state analysis for unbalanced operation	33
3.4.1 Steady state current reference calculation	37
4 Permanent magnet synchronous machine modelling	41
4.1 Introduction	41
4.2 Permanent magnet synchronous machine dynamic equations .	42
4.3 Steady state analysis	49
5 Power converter and grid-side system modelling	51
5.1 Introduction	51
5.2 DC bus dynamic equations	52

Contents

5.3	Grid side system dynamic equations	53
5.4	Steady state analysis for balanced operation	57
5.5	Steady state analysis for unbalanced operation	58
5.6	Three phase transformer with two sets of secondary windings	61

II Control of wind turbines 65

6 Conventional DFIG vector control 67

6.1	Introduction	67
6.2	Machine side control	68
6.3	Grid-side control	73
6.3.1	DC bus voltage regulation	73
6.3.2	AC side current control	75
6.4	Validation of the simulation model using experimental results	79
6.4.1	Controller response	84
6.4.2	Comparison with experimental results	85

7 Dual synchronous reference frame DFIG vector control 91

7.1	Introduction	91
7.2	Machine side control	92
7.3	Grid-side current control	102
7.3.1	AC side current control	102

8 Stationary reference frame DFIG control 109

8.1	Introduction	109
8.2	Machine side control	110
8.2.1	K_d feed-forward compensation design	115
8.2.2	K feedback controller design	119
8.3	Grid-side current control	121
8.3.1	K_d feed-forward compensation design	125
8.3.2	K feedback controller design	129

9 VSC reference calculation issues for unbalanced operation 137

9.1	Introduction	137
9.2	Analysis of the current reference calculation for balanced operation	139
9.3	Analysis of the current reference calculation for unbalanced operation	140
9.4	Simulation testing of the proposed reference calculation scheme	147

Contents

9.5	Experimental testing of the proposed reference calculation scheme	149
9.6	Conclusions	153
10	PMSG vector control	155
10.1	Introduction	155
10.2	Machine side control	155
10.2.1	Discrete time implementation of the controller	157
11	Voltage sag ride-through of PMSG wind turbines using droop control	159
11.1	Introduction	159
11.2	Problem formulation	159
11.3	Generator control strategy formulation	161
11.4	Power reduction controller analysis and design	162
11.5	Simulation testing of the proposed scheme	165
11.6	Experimental results	167
11.7	Conclusions	170
12	Conclusions	171
12.1	Contributions	171
12.2	Future work	172
	Bibliography	173
A	Publications	179

List of Figures

2.1	Power coefficient as a function of the tip speed ratio for $\beta = 0$.	10
2.2	Two mass drivetrain model	14
2.3	Bode plot of the transfer function between the generator torque and the turbine speed	15
2.4	Bode plot of the transfer function between the turbine torque and the turbine speed	16
2.5	Simulated evolution of the turbine speed and the torque applied by the generator during a step increase of the wind speed when controlling the generator using the constant tip speed ratio control technique.	18
2.6	Simulated evolution of the power coefficient of the turbine during the transient produced by a step increase of the wind speed when controlling the generator using the constant tip speed ratio control technique.	18
2.7	Bode plot of the transfer function that relates the generator torque to the wind speed variations. Note the graph is normalized to the nominal generator torque.	19
3.1	Detail of the DFIG connection for a Y-Y configuration without neutral conductor.	22
3.2	DFIG machine equivalent circuit.	31
3.3	DFIG machine equivalent circuit for the unbalanced case.	36
4.1	Detail of the PMSG connection for a Y configuration without neutral conductor.	42
4.2	PMSG machine equivalent circuit.	49
5.1	Back-to-back converter DC bus	52
5.2	Grid side converter connection	54
5.3	Three phase transformer with three-leg core and two secondary winding sets.	62
5.4	Equivalent electric circuit of the three phase transformer with two secondary winding sets.	62

List of Figures

5.5	Equivalent magnetic circuit of the three phase transformer with two secondary winding sets.	63
6.1	Simulated voltage step to test the decoupling feedback loop used by the conventional vector controller of the DFIG	69
6.2	Rotor voltage applied to test the decoupling feedback loop used by the conventional vector controller of the DFIG	70
6.3	Evolution of the rotor current for the test of the decoupling feedback loop used by the conventional vector controller of the DFIG	70
6.4	Evolution of the rotor current of the DFIG to a step reference change when using conventional vector control	72
6.5	DFIG conventional vector control	73
6.6	Evolution DC bus voltage and the current on the DC side of the machine and the grid side inverter for a change in the DC bus voltage reference value and a change in the power injected to the DC bus by the machine inverter.	76
6.7	Simulated voltage step to test the decoupling feedback loop used by the conventional vector controller of the AC side current control. <i>Upper graph:</i> evolution of \hat{v}_l^{qd} . <i>Lower graph:</i> evolution of v_l^{qd} including the voltage applied by the decoupling feedback loop.	78
6.8	Evolution of the AC side current for the test of the decoupling feedback loop used by the conventional vector controller of the AC side current control.	78
6.9	Evolution of the AC side current of the grid side inverter in the qd reference frame to a step reference change when using conventional vector control	80
6.10	Evolution of the AC side current of the grid side inverter in the abc reference frame to a step reference change when using conventional vector control	80
6.11	Evolution of the voltage applied on the AC side of the grid side inverter due to a step change in the current reference when using conventional vector control	80
6.12	Grid-side conventional vector control	81
6.13	Picture of a real ECO74 WTGS. More detail is available on http://www.power.alstom.com	82
6.14	Voltage sag test measurements.	82
6.15	Rms value of the abc voltages on the MV side of the wind turbine transformer during the voltage sag test.	83

List of Figures

6.16	DFIG rotor current. The continuous black line corresponds to the reference value, the continuous grey line corresponds to the actual value and the grey dashed line corresponds to the crowbar connection state.	85
6.17	Machine-side inverter voltages voltage during the voltage sag.	86
6.18	Stator reactive power and generator torque during the voltage sag. The continuous grey line corresponds to the output value, the continuous black line corresponds to the reference value and the grey dashed line corresponds to the crowbar connection state.	87
6.19	Generator torque and angular speed during the voltage sag. .	88
6.20	Grid-side inverter output current during the voltage sag. . . .	88
6.21	Grid-side inverter output voltages during the voltage sag. . .	89
6.22	DC bus voltage during the voltage sag.	89
6.23	Active and reactive power output of the WTGS measured on the MV-side of the transformer	90
6.24	RMS value of the <i>abc</i> currents of the MV-side of the transformer	90
7.1	Rotor voltage applied to test the decoupling feedback loop used by the double synchronous reference frame vector controller of the DFIG	98
7.2	Evolution of the rotor current for the test of the decoupling feedback loop used by the double synchronous reference frame vector controller of the DFIG	99
7.3	Evolution of the rotor current of the DFIG to a step reference change when using dual vector control	100
7.4	Evolution of the DFIG torque to a step reference change when using dual vector control	101
7.5	Bode plot of the first order allpass Hilbert transformation filter.	101
7.6	Simulated voltage step to test the decoupling feedback loop used by the dual synchronous reference frame vector controller of the AC side current control. <i>Upper graph:</i> evolution of \hat{v}_l^{qd} . <i>Lower graph:</i> evolution of v_l^{qd} including the voltage applied by the decoupling feedback loop.	104
7.7	Evolution of the AC side current for the test of the decoupling feedback loop used by the dual synchronous reference frame vector controller of the AC side current control.	105
7.8	Evolution of the AC side current of the grid side inverter in the <i>qd</i> reference frame to a step reference change when using dual synchronous reference frame vector control	106

List of Figures

7.9	Evolution of the AC side current of the grid side inverter in the abc reference frame to a step reference change when using dual synchronous reference frame vector control	106
7.10	Evolution of the voltage applied on the AC side of the grid side inverter due to a step change in the current reference when using dual synchronous reference frame vector control .	107
8.1	Stator voltage applied to test the decoupling feedback loop .	111
8.2	Rotor current evolution during the simulated test of the decoupling feedback loop	111
8.3	Rotor voltage applied by the decoupling feedback loop during its test simulation	112
8.4	Proposed current control structure for the stationary reference frame controller of the DFIG.	114
8.5	Simplified model of the generator control.	114
8.6	Simulated stator voltage disturbance to test the feed-forward compensator used by the stationary frame controller of the DFIG	115
8.7	Simulated evolution of the rotor current under a stator voltage disturbance using the K_{d0} feed-forward controller	116
8.8	Current response for the stator voltage disturbance test of the feed-forward controllers K_{d1} and K_{d2}	117
8.9	Bode plot of the inverse of the transfer function between the stator voltage and the rotor current along with the proposed feed-forward compensators.	118
8.10	Bode plot of the DFIG feedback controller transfer function. .	121
8.11	Bode plot of the closed loop transfer function of the current controller of the DFIG.	122
8.12	Simulated evolution of the DFIG rotor current for a current reference change.	122
8.13	General current control system structure	124
8.14	Simplified current control structure	124
8.15	Grid voltage evolution for the K_d feed-forward controller simulation.	125
8.16	Current response to a voltage disturbance comparing K_{d0} and K_{d1}	126
8.17	Bode plot comparing K_{d0} , K_{d1} and the ideal feed-forward compensator.	129
8.18	Bode plot of the controller transfer function $K(s)$	132
8.19	Bode plots of the open loop and closed loop transfer functions.	133

List of Figures

8.20	Current response to a current reference change comparing the averaged and the switching model evolution. The light grey line on the graph corresponds to the actual current, the dark gray line corresponds to the current measurement sampled by the controller and the black line corresponds to the current reference value.	134
8.21	Scheme of the proposed controller	135
9.1	Current reference calculation methods.	148
9.2	Voltage at the PCC of the converter.	148
9.3	Amplitude of the positive and negative sequence of the voltage at the PCC measured by the PLL.	149
9.4	Comparison of the evolution of the DC bus voltage using I (a), II (b) and III (c) current reference calculation methods.	149
9.5	Comparison of the evolution of the converter output power measured on the inverter versus the power measured on the PCC using I (a,d), II (b,e) and III (c,f) current reference calculation methods.	150
9.6	Comparison of the output current of the converter using I (a), II (b) and III (c) current reference calculation methods.	150
9.7	Picture and schematics of the experimental setup. (1) generator grid-side inverter, (2) grid emulator, (3) converter inductances, (4) generator-side DC power source, (5) grid emulator DC power source and load, (6) generator grid-side inverter voltage v_l^{abc} measurement, (7) grid emulator voltage v_z^{abc} measurement, (8) generator grid-side output current i_l^{abc} measurement, (9) grid connection switch, (10) data acquisition device.	151
9.8	Experimental results for method I. From top to bottom: $v_z^{abc}, i_l^{abc}, P_l$ and P_z	152
9.9	Experimental results for method II. From top to bottom: $v_z^{abc}, i_l^{abc}, P_l$ and P_z	153
9.10	Experimental results for method III. From top to bottom: $v_z^{abc}, i_l^{abc}, P_l$ and P_z	154
11.1	PMSM wind turbine with full power converter.	160
11.2	Droop control ride-through steady state.	162
11.3	Block diagrams of the DC bus dynamics.	163
11.4	Simulation results for a sudden drop of the grid voltage.	166
11.5	Simulation results for a dampened drop in the grid voltage.	167

List of Figures

11.6	WTGS emulator setup	168
11.7	Picture of the real WTGS emulator setup. (A) PMSG generator, (B) PMSM turbine emulator, (C) Turbine emulator converter, (D) grid connection autotransformer, (E) grid side inverter, (F) generator side rectifier, (G) grid connection inductance.	168
11.8	Oscilloscope capture of the voltage sag test. <i>Cyan</i> P_{DCm} power flowing to DC bus from the machine rectifier, <i>dark blue</i> DC bus voltage, <i>red</i> AC grid side current, <i>blue</i> grid voltage. .	169

List of Tables

2.1	Wind turbine characteristic parameters	9
2.2	Values of the z_0 for different types of landscapes. <i>Sources:</i> Panofsky and Dutton, 1984; Simiu and Scanlan, 1986	12
2.3	Drivetrain characteristic parameters	15
3.1	Induction generator parameters from [1]	32
6.1	Characteristic parameters of the WTGS used for the voltage sag test.	81
6.2	Voltage dip parameters	83
8.1	Grid connection converter parameters.	127
8.2	Parameters for the simulation of the current reference value. .	132
9.1	Characteristic parameters of the simulated scenario.	147
11.1	Simulated scenario parameters	166

Nomenclature

Roman symbols

\hat{A}_g	Amplitude of the wind speed gust
\hat{A}_r	Amplitude of the wind speed ramp
\hat{v}_w	Characteristic average wind speed of a location
\underline{I}_r	Generator rotor current phasor
\underline{I}_s	Generator stator current phasor
\underline{V}_r	Generator rotor voltage phasor
\underline{V}_s	Generator stator voltage phasor
A	Wind turbine swept surface
a	$e^{j\frac{2\pi}{3}}$ complex rotation operator
c	Drivetrain characteristic angular damping coefficient
c_i	i -th characteristic coefficient of the turbine aerodynamic model
C_P	Aerodynamic power coefficient
h	Characteristic height of a location
i_r	Induction generator rotor current
i_s	Generator stator current
J_g	Aggregated inertia of the whole mechanical system for the one mass model
J_m	Generator aggregated inertia for the two mass model
J_t	Turbine aggregated inertia for the two mass model
k	Drivetrain characteristic angular stiffness coefficient

Nomenclature

K_{CP}	Constant tip speed ratio speed control law coefficient
l	Characteristic turbulence scale of a location
L_r	Induction generator rotor inductance
L_s	Induction generator stator inductance
L_{lr}	Induction generator rotor leakage inductance
L_{ls}	Induction generator stator leakage inductance
L_{mr}	Induction generator rotor magnetizing inductance
L_{ms}	Induction generator stator magnetizing inductance
L_{rr}	Induction generator rotor autoinductance
L_{rs}	Induction generator maximum rotor to rotor magnetizing inductance
L_{rs}	Induction generator rotor to stator coupling inductance
L_{sr}	Induction generator maximum stator to rotor magnetizing inductance
L_{sr}	Induction generator stator to rotor coupling inductance
L_{ss}	Induction generator stator autoinductance
M	Induction generator magnetizing inductance
N_r	Number of turns of the induction generator rotor windings
N_s	Number of turns of the induction generator stator windings
nr	Neutral point of rotor side inverter
nwr	Neutral point of the rotor windings of the generator
nws	Neutral point of the stator windings of the generator
nwz	Neutral point of the machine side windings of the generator transformer
P_m	Generator mechanical power
P_r	Induction generator rotor power
P_s	Induction generator stator power

Nomenclature

Q_r	Induction generator rotor reactive power
Q_s	Generator stator reactive power
R	Wind turbine radius
r_r	Induction generator rotor winding resistance
r_s	Generator stator winding resistance
S	Fortescue variable transformation matrix
s	Induction generator slip
t	Time
$T(\theta)$	Park variable transformation matrix
T_{eg}	Wind speed gust ending time
T_{et}	Wind speed ramp ending time
T_{sg}	Wind speed gust starting time
T_{st}	Wind speed ramp starting time
v_r	Induction generator rotor voltage
v_s	Generator stator voltage
v_w	Wind speed
v_{wa}	Wind speed average component
v_{wg}	Wind speed gust component
v_{wr}	Wind speed ramp component
v_{wt}	Wind speed turbulence component
z_0	Characteristic terrain roughness length of a location

Greek symbols

β	Wind turbine blade pitch angle
Γ_m	Generator torque

Nomenclature

Γ_t	Wind turbine torque
λ	Tip speed ratio
λ_r	Induction generator rotor flux linkage
λ_s	Induction generator stator flux linkage
ν	Gearbox multiplication ratio
ω_e	Electrical network frequency
ω_m	Generator speed
ω_r	Generator electrical angle speed
ω_t	Wind turbine speed
ρ	Air density
θ_m	Generator shaft angular position
θ_r	Generator rotor electric angle
θ_t	Turbine angular position
φ	Phase of a sinusoidal magnitude
P	Generator pole pairs
P_t	Power extracted by the turbine

Superscripts

'	Reduced variable
*	Reference value
+	Positive sequence value
—	Negative sequence value
<i>abc</i>	Vector of <i>abc</i> components
<i>N</i>	Nominal value
<i>qd0</i>	Vector of <i>qd0</i> components

Nomenclature

ss Steady state value

Subscripts

l Variable related to the grid connection point of the converter

m Variable related to the generator shaft

r Variable related to the generator rotor

s Variable related to the generator stator

t Variable related to the turbine

z Variable related to the grid connection point of the wind turbine

Acronyms

CITCEA Centre d’Innovació Tecnològica en Convertidors Estàtics i Accionaments

DFIG Doubly Fed Induction Generator

IGBT Isolated Gate Bipolar Transistor

PMSG Permanent Magnet Synchronous Generator

UPC Universitat Politècnica de Catalunya

WTGS Wind Turbine Generation System

Chapter 1

Introduction

Wind energy is considered nowadays to be one of the most promising renewable energy sources. The historical data on installed wind power capacity show that it has been growing at an increasing rate for the last 20 years [2]. The growing penetration of wind farms in the grid has arisen a number of issues for the proper operation of the grid. Namely, wind farms are known to be less robust to voltage sags than conventional energy generation plants. In the former days, when a deep voltage sag occurred due to a fault in the grid, wind farms would disconnect from the grid to avoid damaging the turbines. This sudden disconnection of power input to the grid would cause an imbalance which in some situations could lead to network instability. In order to avoid that, modern wind farms are required to be able to ride through voltage sags, that is, to remain connected while the fault is cleared.

Voltage sags are usually classified in two types: balanced and unbalanced. Balanced voltage sags are caused by three phase faults and starting transients of large machines, they are characterized by a symmetrical sudden drop of the voltage of the grid voltages. Unbalanced voltage sags are caused by non symmetrical faults, they are more common than the balanced sags and cause an asymmetrical drop in voltage of each phase.

The first wind farms to be installed were based on fixed speed squirrel cage induction generators. During the last decade of the 20th century, the need to optimize the energy extraction to increase the power rating of the wind turbines and the need to provide reactive power support to the grid led to gradually replace this topology by the so called doubly fed induction generators (DFIG).

The variable speed wind turbines with DFIG are the most common type of wind turbine generation systems (WTGS) installed nowadays. This topology uses a gearbox to adapt the low speed of the turbine to the operating speed of a wound rotor induction generator controlled through a small rated back-to-back voltage source converter (VSC) connected to the rotor of the machine.

The main benefits of this topology compared to the previous squirrel cage

Chapter 1 Introduction

wind turbines without power converter are the ability to operate at a wider range of speeds, thus to optimize the energy extraction from the wind, and the ability to precisely control the active and reactive power injected to the grid.

The most common control scheme for the DFIG-based WTGS, the conventional vector control design [3], have been proven to provide good performance under balanced conditions. The ride-through capabilities of the DFIG for symmetrical voltage sags using this control method plus rotor connected resistors in case of an excess of power flowing through the rotor windings were analyzed in detail in [4]. The performance obtained by this method was also later discussed for a number of different scenarios in [5]. This method can be arguably considered to be the base of the more advanced methods for unbalance operation and will be extensively analyzed in the present thesis.

Unbalanced conditions caused by non symmetrical faults require different approaches as the conventional vector control scheme exhibits poor performance under such conditions. One possible solution was presented in [6], where this problem is solved by using the so called double synchronous reference frame vector control which separately controls the positive and negative sequence of the current by using band-stop filters to separate the positive and the negative sequence of the magnitudes. This approach was later used in [7] where a new current reference calculation method was suggested to coordinate the control of the machine side and the AC grid side of the converter to minimize the DC bus voltage ripple due to the oscillations of active power coming from the machine.

Although this current control scheme has been proven to enable the operation under grid unbalances, its main disadvantage is the need to process the Fortescue decomposition of the measured signals by the use of filters which have a limited frequency operating range and decrease the performance that can be obtained from the system. Different possible alternate designs exist in the literature: first order all-pass filters are used in [8] and the so called generalized second order integrator is used in [9]. Although each of these filters have their own advantages, all of them have a limited bandwidth and add phase lag to the open loop current transfer functions and thus degrade the system performance.

A different approach to avoid the use of these filters was suggested in [10] where unbalanced operation capability is obtained by extending the vector control scheme by adding high gain to the current controllers around the double frequency of the grid thus making the controller suitable to follow current reference signals which also contain negative sequence. This approach has been shown to work well but implies the need of current con-

trollers designed to follow reference signals around two different frequency ranges.

Another different approach is the use of stationary frame current controllers which are designed to have a high gain around the grid frequency to be able to track sinusoidal reference signals. This approach has the same basic advantages of the scheme proposed in [10] and the only main difference is that the resulting controllers have a high gain around a single frequency range, thus they are slightly simpler. Here both the dual synchronous reference frame and a stationary reference frame design will be extensively analyzed and discussed.

Regarding, the reference calculation, several options exist in case of unbalanced voltage sags. The previously mentioned works on control under unbalanced conditions use the reference calculation scheme from [11]. This scheme uses negative sequence current to compensate for the oscillation of the power injected to the grid that appears due to the presence of negative sequence in the grid voltage. Here a critic analysis of the application of this method to the calculation of the current references for the control of a voltage source converter is presented along with remarks on several weak points of this procedure and possible solutions for them.

Recently, the need to reduce the maintenance costs of the wind turbines for offshore wind farms have risen the interest in replacing the DFIG by permanent magnet synchronous generators (PMSG) with full rated power converter in the new wind turbines. The reason to do that is that even though this new topology requires a new type of electrical machine with higher manufacturing costs and a power converter with a higher rating, there are a number of interesting benefits of this configuration. The first feature of the PMSG that caught the attention of the wind turbine manufacturers was the possibility to create PMSGs with a large number of pair poles, rendering the machine able to operate at very low speeds compatible with the operating speeds of the wind turbines [12]. This way a direct drive design of the wind turbine without gearbox could be manufactured to suppress one important source of maintenance costs and failures.

Another important feature of the PMSG topology is that the machine is completely isolated from the grid through the converter unlike the DFIG which has the stator of the machine connected to the grid. This makes the machine less sensible to grid disturbances, suppressing a number of design challenges regarding the need to improve the control methods to reduce the stress over the generator and the mechanical system of the wind turbine in case of need to operate during grid faults.

Finally, another interesting feature of the PMSG topology is that the

Chapter 1 Introduction

higher rating of the converter and the complete decoupling between the generator and the grid connection make it possible to implement with ease new strategies and special behaviours to operate under different grid conditions.

Vector control of PMSG has been proved to provide good performance characteristics. The principles behind this method originate in [13] and its use to control the PMSG is extensively documented in the literature [14, 15]. Here, the basic vector control scheme will be described and a ride-through strategy which enables independent control of the AC grid side connection of the converter and the machine rectifier will be analyzed.

Part I

Modelling of wind turbines

Chapter 2

Wind turbine mechanical system modelling

2.1 Introduction

This chapter analyzes the modelling of the dynamics of the mechanical system of a variable speed wind turbine. First, in Section 2.2, a simple aerodynamic model based on [16] is described. This model relates the power extracted from the wind passing through the surface swept by the turbine to the wind speed and the rotating speed of the turbine. A linearized version of this model is also obtained here to later simplify the analysis of the performance requirements of the wind turbine generator torque control. In Section 2.3, a model of the wind speed originating from [17] is presented. Section 2.4 analyzes the modelling of the wind turbine drivetrain dynamics. A so called two-mass model is presented and briefly compared to a more simple one-mass model. Finally, a basic wind turbine speed control called constant tip speed ratio control is presented and discussed in Section 2.5. The stability and the dynamic behaviour of the system are analyzed and the basic performance requirements of the torque control of the generator are obtained.

2.2 Modeling of the wind turbine aerodynamics

According to [18], wind turbine generation is based on the extraction of power from the kinetic energy of the wind. Hence, the power extracted by the turbine P_t can be expressed as the kinetic power available in the stream of air across the area swept by its blades P_w multiplied by an dimensionless coefficient C_P called power coefficient. The C_P can be thought as a measure of the aerodynamic efficiency of the turbine and depends on the relation between the average speed of the air across the area covered by the wind wheel and its angular speed and the geometry of the turbine (which also

Chapter 2 Wind turbine mechanical system modelling

depends on the pitch angle of the blades). The power extracted by the wind turbine has the following expression:

$$P_t = c_P P_w = c_P \frac{1}{2} \rho A v_w^3 \quad (2.1)$$

where ρ is the air density assumed to be constant,
 A is the surface covered by the wind wheel,
 v_w is the average wind speed.

There have been different approaches to model the power coefficient ranging from considering it to be constant for steady state and small signal response simulations to using look-up tables with measured data. A common approach is to use an analytic expression suggested in [16] of the form:

$$c_P(\Lambda, \beta) = c_1 \left(c_2 \frac{1}{\Lambda} - c_3 \beta - c_4 \beta^{c_5} - c_6 \right) e^{-c_7 \frac{1}{\Lambda}} \quad (2.2)$$

where $[c_1 \dots c_9]$ are characteristic parameters of the wind turbine which can be obtained by statistical analysis of measured data from a real turbine and finite element method simulations, β is the blade pitch angle and Λ is defined as:

$$\frac{1}{\Lambda} \triangleq \frac{1}{\lambda + c_8 \beta} - \frac{c_9}{1 + \beta^3} \quad (2.3)$$

where λ is the so called tip speed ratio and it is defined as:

$$\lambda \triangleq \frac{\omega_t R}{v_w} \quad (2.4)$$

where ω_t is the turbine speed and R is the turbine radius.

To simulate the response of the turbine, the power extracted by the turbine for a given wind speed, angular speed of the turbine and the blade pitch angle, can be easily computed by using (2.1). Dividing the extracted power by the angular speed, the turbine torque, which is needed for the simulation of the mechanical dynamics, is obtained as:

$$\Gamma_t = C_P \frac{1}{2} \rho A v_w^3 \frac{1}{\omega_t} \quad (2.5)$$

The characteristic parameters for a turbine case that will be used along this document can be found in Table 2.1. Figure 2.1 shows a plot of the power coefficient as a function of the tip speed ratio for a constant pitch angle for this turbine. According to [18], this is the usual shape of the C_P

2.2 Modeling of the wind turbine aerodynamics

curve for a three blade wind turbine and it usually has a maximum that can be obtained by for $\lambda \approx 8$. In this case, the maximum corresponds to the 48% of the available power. The theoretical limit for the aerodynamic efficiency for any possible wind turbine corresponds to approximately 59%[16].

Parameter	Value	Units	Description
R	33	m	Turbine radius
v_w^N	9	m/s	Nominal wind speedt
ρ	1,225	Kg/m ³	Air density
c_1	1	1	C_P function parameters
c_2	39,52	1	
c_3	0	1	
c_4	0	1	
c_5	0	1	
c_6	2,04	1	
c_7	14,47	1	
c_8	0	1	
c_9	0	1	
λ_{opt}	8,28	1	Optimal tip speed ratio
C_P^{opt}	0,476	1	Optimal power coefficient
ω_t^N	21,57	min ⁻¹	Wind turbine nominal speed
Γ_t^N	0,322e6	Nm	Wind turbine nominal torque
P_t^N	727,3	kW	Wind turbine nominal power

Table 2.1: Wind turbine characteristic parameters

The maximum efficiency for a given turbine, can be calculated by differentiating (2.2) as a function of λ and solving for the roots of this equation. For the sake of simplicity here the pitch angle is taken as zero as an increase on the pitch angle always leads to a reduction on the force that the wind applies on the blades. The maximum efficiency C_P^{opt} becomes:

$$C_P^{opt} = \frac{c_1 c_2}{c_7} e^{-\frac{c_2 + c_6 c_7}{c_2}} \quad (2.6)$$

also, the so called optimal tip speed ratio to obtain this efficiency is:

$$\lambda^{opt} = \frac{1}{c_9 + \frac{c_6}{c_2} + \frac{1}{c_7}} \quad (2.7)$$

Thus, considering the wind speed to be known, the power extracted by the turbine can be maximized by simply driving the turbine to match the

Chapter 2 Wind turbine mechanical system modelling

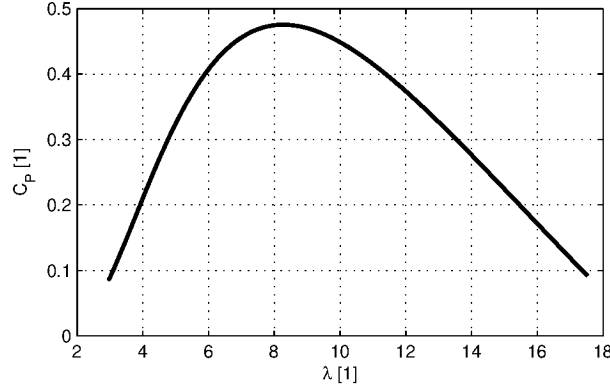


Figure 2.1: Power coefficient as a function of the tip speed ratio for $\beta = 0$.

corresponding speed for the optimal tip speed ratio. As the wind is hard to measure, usually a different open loop strategy without wind speed sensors is used, this will be explained in more detail later.

On the other hand, to analyze the dynamics of the mechanical system, it is also useful to do a small signal linearization of the torque equation (2.5) around the nominal operation. The following relation is obtained:

$$\Gamma_t \approx \Gamma_t^N + \frac{3\Gamma_t^N}{v_w^N} \delta v_w - \frac{\Gamma_t^N}{\omega_t^N} \delta \omega_t \quad (2.8)$$

where the nominal values for the wind speed, the turbine torque, the turbine speed are v_w^N , Γ_t^N and ω_t^N and the small signal variables are defined as:

$$\delta v_w \triangleq v_w - v_w^N \quad (2.9)$$

$$\delta \Gamma_t \triangleq \Gamma_t - \Gamma_t^N \quad (2.10)$$

$$\delta \omega_t \triangleq \omega_t - \omega_t^N \quad (2.11)$$

2.3 Wind speed modelling

Wind speed varies from one location to another and also fluctuates over the time in a stochastic way. As it has been previously shown, it maintains a direct relation to the force that the turbine blades receive from the wind. Therefore, it has a direct effect on the extracted power and its evolution must be taken into account to properly simulate the WTGS dynamics.

2.3 Wind speed modelling

One possible approach to generate the wind speed signal on simulations may be to use logs of real measurements of the speed on the real location of the WTGS. This approach has some evident limitations because it requires a measurement to be done on each place to be simulated. Another choice, proposed by [17] is to use a mathematical model which takes some landscape parameters to generate a wind speed sequence for any location. This wind speed expression has the form:

$$v_w(t) = v_{wa}(t) + v_{wr}(t) + v_{wg}(t) + v_{wt}(t) \quad (2.12)$$

where $v_{wa}(t)$ is a constant component,
 $v_{wr}(t)$ is a common ramp component,
 v_{wg} is a gust component,
 v_{wt} is a turbulence component.

The $v_{wa}(t)$ component is a constant value used to set a constant wind speed. The v_{wr} component is a limited ramp function used to simulate a increase in the wind speed and it can be written as a function of time as:

$$v_{wr}(t) = \begin{cases} 0, & \text{per } t < T_{sr} \\ \hat{A}_r \frac{(t-T_{sr})}{(T_{er}-T_{sr})}, & \text{per } T_{sr} \leq t \leq T_{er} \\ \hat{A}_r, & \text{per } T_{er} < t \end{cases} \quad (2.13)$$

where \hat{A}_r is the amplitude of the ramp and T_{sr} and T_{er} are the start and the end time of the ramp.

The gust component may be useful to simulate an abnormal temporary increase of the speed of the wind and its expression is:

$$v_{wg}(t) = \begin{cases} 0, & \text{for } t < T_{sg} \\ \hat{A}_g \left(1 - \cos \left[2\pi \left(\frac{t-T_{sg}}{T_{eg}-T_{sg}} \right) \right] \right), & \text{for } T_{sg} \leq t \leq T_{eg} \\ 0, & \text{for } T_{eg} < t \end{cases} \quad (2.14)$$

where \hat{A}_g is the amplitude of the gust and T_{sg} and T_{eg} are the start and the end time of the gust.

Finally, as discussed in [19], the turbulence component v_{wt} is a signal which has a power spectral density of the form:

$$P_{Dt}(f) = \frac{l\hat{v}_w \left[\ln \left(\frac{h}{z_0} \right) \right]^{-2}}{\left[1 + 1.5 \frac{fl}{\hat{v}_w} \right]^{5/3}} \quad (2.15)$$

Chapter 2 Wind turbine mechanical system modelling

where \hat{v}_w is the average wind speed, h is the height of interest (the wind wheel height), l is the turbulence scale which is twenty times h and has a maximum of 300 m and z_0 is a roughness length parameter which depends on the landscape type as shown in Table 2.2.

Landscape type	Range of z_0 (m)
Open sea or sand	0,0001-0,001
Snow surface	0,001-0,005
Mown grass or steppe	0,001-0,01
Long grass or rocky ground	0,04-0,1
Forests, cities and hilly areas	1-5

Table 2.2: Values of the z_0 for different types of landscapes. *Sources:* Panofsky and Dutton, 1984; Simiu and Scanlan, 1986

The parameters of the power spectral density function of the wind speed turbulence can be computed from the height of the wind turbine, the average wind speed and the kind of landscape where the WTGS is located. The next step to simulate the evolution of the wind speed is to generate a signal which has the desired power spectral density. There are many ways of doing this, as for example by summing a large number of sines with random phases and amplitudes according to the P_{Dt} function as suggested in [20] or by designing a shaping filter and applying it to a flat spectrum noise signal.

Finally, note that although it is important to be able to perform long simulations with a realistic model for the whole WTGS, as most simulations for power quality studies are very short in time, sometimes a very simplified model including only the step component or even a constant wind speed will be used. The reason for this is that sometimes it is wanted to be able to easily isolate the changes in the system variables induced by grid disturbances from the distortions produced by the random nature of the wind.

2.4 Drivetrain modelling

The drivetrain of a WTGS comprises the wind turbine, the turbine shaft, the gearbox and the generator’s rotor shaft. The ν multiplication ratio of the gearbox is usually comprised between 50 and 150 and the wind turbine inertia is usually about the 90% of the inertia of the whole system according to [1].

The turbine blades are usually made of composite materials which are light enough to make it feasible to build very large turbines. Due to the

2.4 Drivetrain modelling

heavy forces applied by the wind on the blades, they tend to deform thus introducing some dynamic effects on the transmission of the power between the wind kinetic energy and the mechanical power transmitted to the electrical generator. A common way to model this phenomenon is by the use of partial differential equations which can be solved by the finite element method [21]. As solving this equations is computational intensive task, usually lumped parameter system approximations are used for the simulation of these systems if only a rough approximation of the behaviour of the mechanical system is needed. A common approximation is to treat the mechanical system as a series of masses connected through elastic couplings with linear stiffness, a damping ratio and a multiplication ratio between them [1]. Here a model of two masses, graphically presented in Figure 2.2 is used. The model consists of one inertia J_t corresponding to the turbine inertia connected to another inertia J_m corresponding to the motor and the gearbox through an elastic shaft with a k angular stiffness coefficient and a c angular damping coefficient. By applying the Newton's laws to such system, the dynamical equations for it are obtained as:

$$\begin{bmatrix} \dot{\omega}_m \\ \dot{\omega}_t \\ \omega_m \\ \omega_t \end{bmatrix} = \begin{bmatrix} \frac{-c}{\nu^2 J_m} & \frac{c}{\nu J_m} & -\frac{k}{\nu^2 J_m} & \frac{k}{\nu J_m} \\ \frac{c}{\nu J_t} & -\frac{c}{J_t} & \frac{k}{\nu J_t} & -\frac{k}{J_t} \\ 1 & 0 & 0 & 0 \\ 0 & 1 & 0 & 0 \end{bmatrix} \begin{bmatrix} \omega_m \\ \omega_t \\ \theta_m \\ \theta_t \end{bmatrix} + \begin{bmatrix} \frac{1}{J_m} & 0 \\ 0 & \frac{1}{J_t} \\ 0 & 0 \\ 0 & 0 \end{bmatrix} \begin{bmatrix} \Gamma_m \\ \Gamma_t \end{bmatrix} \quad (2.16)$$

where θ_t is the turbine angle,
 θ_m is the generator shaft angle,
 ω_t is the turbine speed,
 ω_m is the generator speed,
 τ_t is the torque applied to the turbine by the wind,
 τ_m is the generator torque.

This equations can be thought as the state space representation of a system which has the turbine and generator torque as inputs which need to be calculated from the wind turbine aerodynamic model and the generator model to simulate the evolution of the system.

To study the dynamical characteristics of the drivetrain, it is useful to apply the Laplace transform to its equations. Here the Laplace transform of the turbine speed $\omega_t(s)$ as a function of the generator and the turbine torque is obtained as:

Chapter 2 Wind turbine mechanical system modelling

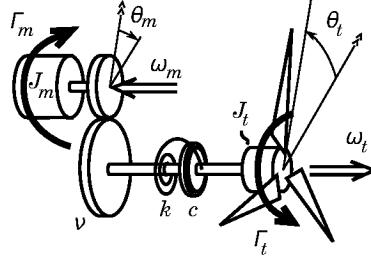


Figure 2.2: Two mass drivetrain model

$$\omega_t(s) = \frac{c\nu s + k\nu}{J_m J_t \nu^2 s^3 + (J_m c \nu^2 + J_t c) s^2 + (J_m k \nu^2 + J_t k) s} \Gamma_m(s) + \frac{J_m \nu^2 s^2 + cs + k}{J_m J_t \nu^2 s^3 + (J_m c \nu^2 + J_t c) s^2 + (J_m k \nu^2 + J_t k) s} \Gamma_t(s) \quad (2.17)$$

From this equation it can be seen that for either $c \rightarrow \infty$ or $k \rightarrow \infty$, that is if the mechanical system is considered to be rigid, the equation becomes equivalent to a one mass model where the inertia of the whole system can be aggregated:

$$\omega_t(s) = \frac{\nu}{(J_m \nu^2 + J_t) s} \Gamma_m(s) + \frac{1}{(J_m \nu^2 + J_t) s} \Gamma_t(s) = \frac{\nu}{J_g s} \Gamma_m(s) + \frac{1}{J_g s} \Gamma_t(s) \quad (2.18)$$

where J_g is the aggregated inertia of the whole mechanical system.

The characteristic parameters for an example case can be found in Table 2.3. The bode plots of the transfer function between the generator torque and the turbine speed and the turbine torque and the turbine speed for both models is shown in Figure 2.3 and Figure 2.4. Note that both models are identical at low frequency, thus proper modelling of the turbine elastic nature may not be necessary to have a proper representation of the system behavior for slow transient phenomena.

2.5 Wind turbine speed control

As it was previously shown in Section 2.2, the power available to be extracted by a wind turbine depends on the average speed of the wind that crosses

2.5 Wind turbine speed control

Parameter	Value	Units	Description
ν	90	1	Gearbox transform ratio
I_t^1	4e6	Kg m ²	One-mass wind turbine aggregated inertia
I_t^2	3,6e6	Kg m ²	Two-mass wind turbine aggregated inertia
I_m	49,38	Kg m ²	Two-mass generator aggregated inertia
c	10 ⁶	Nm rad ⁻¹	Two-mass damping ratio
k	6e7	Nm s rad ⁻¹	Two-mass stiffness coefficient
ω_m^N	1,941	min ⁻¹	Generator nominal speed
Γ_m^N	3,58e3	Nm	Generator nominal torque

Table 2.3: Drivetrain characteristic parameters

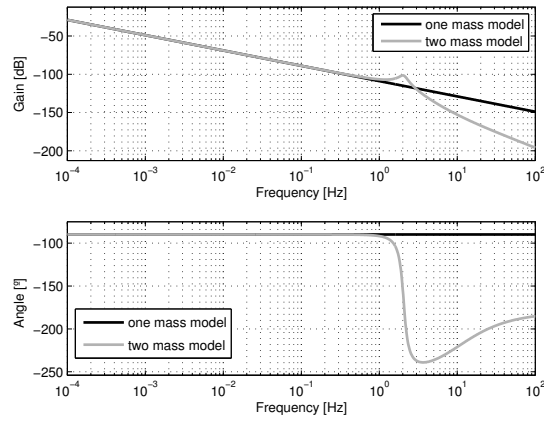


Figure 2.3: Bode plot of the transfer function between the generator torque and the turbine speed

Chapter 2 Wind turbine mechanical system modelling

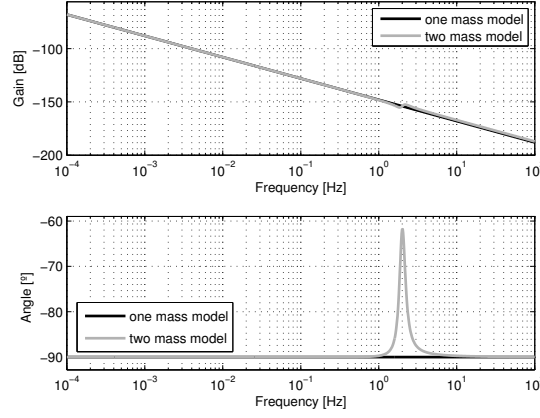


Figure 2.4: Bode plot of the transfer function between the turbine torque and the turbine speed

the surface swept by its blades. Also, to have the maximum possible power extraction from the wind, it was shown that the speed of the turbine must match a certain value that depends on the speed of the wind.

The precise measurement of the wind speed is a hard task due to the local variations of the speed and the distortions introduced by the operation of the wind turbine. For this reason, a number of different control strategies to maximize the energy extraction by doing the so called maximum power point tracking (MPPT) without the need of a wind speed measurement have been suggested in the past. The most basic and well known of these techniques is the so called constant tip speed ratio control, which has been extensively documented in the literature [22, 3, 23] and is usually used for the modelling of the speed control behavior for power quality simulations of wind turbines. Here only a some details on this technique which are useful to know for the proper design of the generator current control will be presented.

The control action for the constant tip speed ratio control can be calculated as:

$$\Gamma_m^* = \frac{1}{\nu} K_{CP} \omega_t^2 \quad (2.19)$$

where Γ_m^* is the generator torque reference value and

$$K_{CP} = \frac{1}{2} \rho A R^3 \frac{c_1 (c_2 + c_6 c_7)^3 e^{-\frac{c_2 + c_6 c_7}{c_2}}}{c_2^2 c_7^4} \quad (2.20)$$

2.5 Wind turbine speed control

In order to study the resulting dynamics, as the speed control law and the turbine aerodynamic curve are nonlinear, a small signal linearization of the equations around the nominal operating point can be performed. Considering the generator control to be perfect so that $\Gamma_m = \Gamma_m^*$, the following relation is obtained by linearization:

$$\Gamma_m \approx \Gamma_m^N + \frac{2\Gamma_m^N}{\omega_t^N} \delta\omega_t = -\frac{\Gamma_t^N}{\nu} - \underbrace{\frac{2\Gamma_t^N}{\nu\omega_t^N} \delta\omega_t}_{\delta\Gamma_m} \quad (2.21)$$

where Γ_m^N and ω_t^N are the nominal values for the generator torque and the turbine speed and the small signal variable $\delta\Gamma_m$ is defined as:

$$\delta\Gamma_m \triangleq \Gamma_m - \Gamma_m^N \quad (2.22)$$

By combining the Laplace transform of the turbine speed as a function of the turbine and generator torque (2.17) or (2.18), the linealized turbine torque equation (2.8) and the linealized generator torque (2.21) the transfer function between the wind speed and the turbine speed can be obtained. For the sake of simplicity, here only the equation for the one mass model is presented:

$$\frac{\delta\omega_t}{\delta v_w}(s) = \frac{\frac{3\Gamma_t^N}{J_g v_w^N}}{s + \frac{3\Gamma_t^N}{J_g \omega_t^N}} \quad (2.23)$$

From this equation, several conclusions can be drawn. The first to note is that the system will be stable as the term $\frac{3\Gamma_t^N}{J_g \omega_t^N}$ is always positive. On the other hand, the system response will be that of a first order system with a time constant of $\tau = \frac{3\Gamma_t^N}{J_g \omega_t^N}$ which depends on the system characteristics and can not be adjusted.

In order to properly design the generator current control, it is also useful to obtain the transfer function that relates the generator torque, which is the reference input to this control loop, to the wind speed variations. By introducing (2.23) into (2.21) the following is obtained:

$$\frac{\delta\Gamma_m}{\delta v_w}(s) = \frac{\frac{-6(\Gamma_t^N)^2}{\nu J_g v_w^N \omega_t^N}}{s + \frac{3\Gamma_t^N}{J_g \omega_t^N}} \quad (2.24)$$

Next the response of the system to a step increase of the wind speed is simulated and its evolution is compared between the linearized model and

Chapter 2 Wind turbine mechanical system modelling

the nonlinear model. The evolution of the turbine speed and the generator torque is presented in Figure 2.5, the evolution of the power coefficient is presented on Figure 2.6.

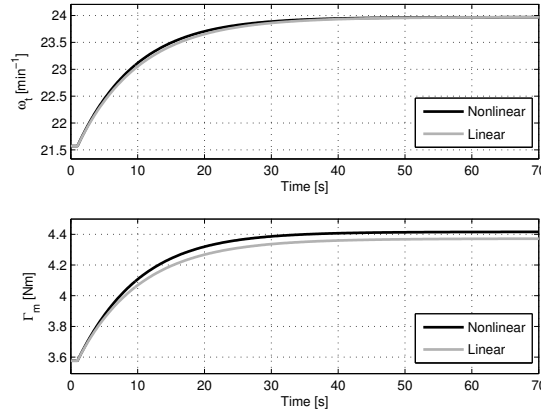


Figure 2.5: Simulated evolution of the turbine speed and the torque applied by the generator during a step increase of the wind speed when controlling the generator using the constant tip speed ratio control technique.

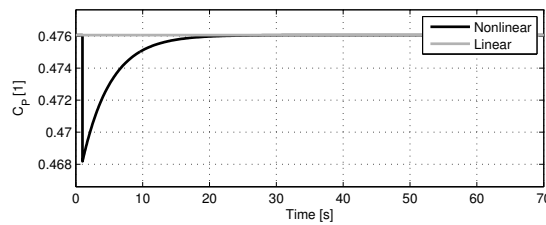


Figure 2.6: Simulated evolution of the power coefficient of the turbine during the transient produced by a step increase of the wind speed when controlling the generator using the constant tip speed ratio control technique.

It can be seen that there are only slight differences between the predicted evolution on both models thus confirming the usefulness of the linearization. It can also be seen that the transient response is very slow with a time constant of approximately 11 seconds, and that during this transient the power extraction is not optimal.

2.5 Wind turbine speed control

Figure 2.7 shows the bode plot of (2.24). This graph provides useful information about the use that the speed control does of the torque control action, this way it is possible to decide the performance needed from the generator current controller.

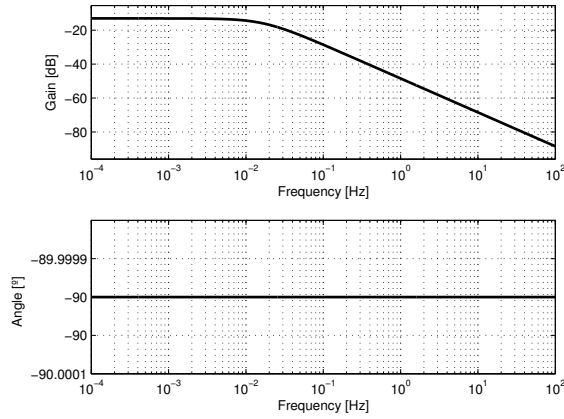


Figure 2.7: Bode plot of the transfer function that relates the generator torque to the wind speed variations. Note the graph is normalized to the nominal generator torque.

Note that for a step increase of the wind speed by 1m/s, the system needs to increase the applied torque by approximately 22% (-13 dB) of the nominal torque in steady state while for frequencies above 20 Hz, the gain becomes lower than 1% of this value (-53 dB). This frequency can be thought as a lower bound for the bandwidth of the generator current controller and it is very low because of the very slow dynamics of the mechanical system.

Chapter 3

Induction machine modelling

3.1 Introduction

This chapter discusses the modelling of an induction machine. The induction machine is nowadays the most common type of electrical machine used for wind generation.

The chapter is organized as follows: first, a dynamic model of the induction machine based on [24] is presented in Section 3.2. The equations of the machine are first presented in their abc variable form and later the variables are transformed to the so called Park variables by introducing the Park variable transformation matrix which will be useful for the study of the machine and the design of the controllers in later chapters. The steady state operation equations of the machine, which make it easy to calculate the relations between the current flowing through the machine windings and the voltage applied to the machine, are obtained from the dynamic equations. First the equations for a balanced case are presented in Section 3.3 and later a more general unbalanced case is analyzed in Section 3.4.

The methods to calculate the current reference values needed to obtain the desired torque and reactive power output of the machine are also analyzed. First, the calculation method used in the conventional vector control which considers the grid voltages to be balanced is analyzed and later a generalized calculation method for unbalanced operation, which allows to suppress the machine torque oscillations in case of an asymmetric voltage sag, is analyzed.

3.2 Induction machine dynamic equations

Figure 3.1 shows the connection schematics for the DFIG machine.

We define the machine stator and rotor voltage vectors v_s^{abc} and v_r^{abc} as the vectors of voltages applied to each of their windings. Thus, they can be written as a function of the transformer secondary windings voltages and the machine side inverter voltages as:

Chapter 3 Induction machine modelling

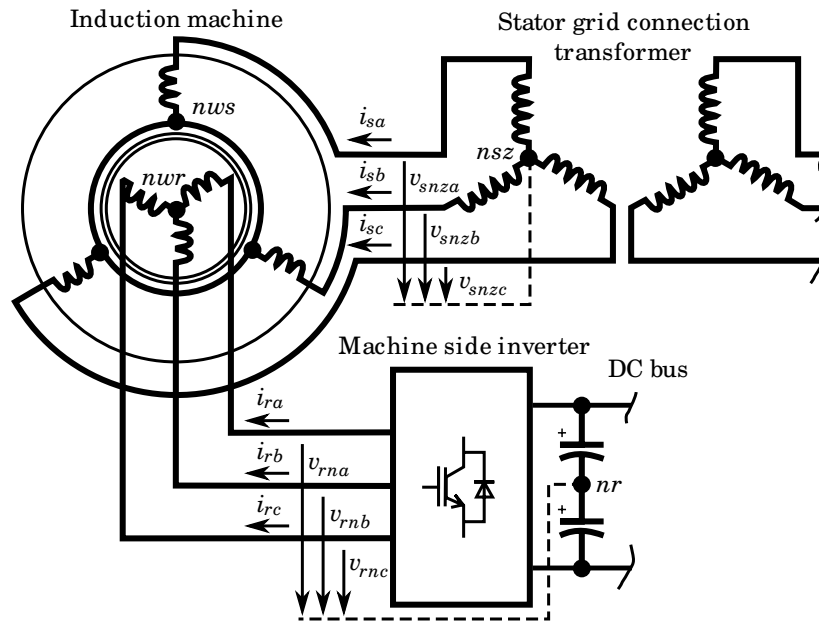


Figure 3.1: Detail of the DFIG connection for a Y-Y configuration without neutral conductor.

3.2 Induction machine dynamic equations

$$v_s^{abc} = v_{snz}^{abc} + (v_{nsz} - v_{nws}) \begin{bmatrix} 1 \\ 1 \\ 1 \end{bmatrix} \quad (3.1)$$

and

$$v_r^{abc} = v_{rn}^{abc} + (v_{nr} - v_{nwr}) \begin{bmatrix} 1 \\ 1 \\ 1 \end{bmatrix} \quad (3.2)$$

Also as no neutral conductor is present it can be stated that:

$$\begin{cases} i_{sa} + i_{sb} + i_{sc} = 0 \\ i_{ra} + i_{rb} + i_{rc} = 0 \end{cases} \quad (3.3)$$

According to [24] the relation between the current and the applied voltage on the windings of a symmetrical induction can be written as:

$$v_s^{abc} = r_s i_s^{abc} + \frac{d}{dt} \lambda_s^{abc} \quad (3.4)$$

$$v_r^{abc} = r_r i_r^{abc} + \frac{d}{dt} \lambda_r^{abc} \quad (3.5)$$

where v_s^{abc} and v_r^{abc} are the stator and rotor voltage vectors,
 i_s^{abc} and i_r^{abc} are the stator and rotor current vectors,
 λ_s^{abc} and λ_r^{abc} are the stator and rotor flux linkage vectors,
 r_s is the resistance of a single phase of the stator,
 r_r is the resistance of a single phase of the rotor.

Considering an ideal linear magnetic behaviour, the flux linkage vectors can be written as a function of the current vectors as:

$$\begin{bmatrix} \lambda_s^{abc} \\ \lambda_r^{abc} \end{bmatrix} = \begin{bmatrix} L_{ss}^{abc} & L_{sr}^{abc} \\ L_{rs}^{abc} & L_{rr}^{abc} \end{bmatrix} \begin{bmatrix} i_s^{abc} \\ i_r^{abc} \end{bmatrix} \quad (3.6)$$

where L_{ss}^{abc} , L_{sr}^{abc} , L_{rs}^{abc} and L_{rr}^{abc} are the coupling matrices which can be written as:

$$L_{ss}^{abc} = \begin{bmatrix} L_{ls} + L_{ms} & -\frac{1}{2}L_{ms} & -\frac{1}{2}L_{ms} \\ -\frac{1}{2}L_{ms} & L_{ls} + L_{ms} & -\frac{1}{2}L_{ms} \\ -\frac{1}{2}L_{ms} & -\frac{1}{2}L_{ms} & L_{ls} + L_{ms} \end{bmatrix}, \quad (3.7)$$

Chapter 3 Induction machine modelling

$$L_{rr}^{abc} = \begin{bmatrix} L_{lr} + L_{mr} & -\frac{1}{2}L_{mr} & -\frac{1}{2}L_{mr} \\ -\frac{1}{2}L_{mr} & -L_{lr} + L_{mr} & -\frac{1}{2}L_{mr} \\ -\frac{1}{2}L_{mr} & -\frac{1}{2}L_{mr} & L_{lr} + L_{mr} \end{bmatrix}, \quad (3.8)$$

$$L_{sr}^{abc} = \left\{ L_{rs}^{abc} \right\}^t = L_{sr} \begin{bmatrix} \cos(\theta_r) & \cos(\theta_r + \frac{2\pi}{3}) & \cos(\theta_r - \frac{2\pi}{3}) \\ \cos(\theta_r - \frac{2\pi}{3}) & \cos(\theta_r) & \cos(\theta_r + \frac{2\pi}{3}) \\ \cos(\theta_r + \frac{2\pi}{3}) & \cos(\theta_r - \frac{2\pi}{3}) & \cos(\theta_r) \end{bmatrix} \quad (3.9)$$

where L_{ls} and L_{lr} are the stator and rotor leakage self-inductances,
 L_{ms} and L_{mr} are the stator and rotor core self-inductances,
 L_{sr} is the maximum value of the coupling inductance between the rotor and the stator,
 θ_r is the rotor angle multiplied by the number of pair poles of the machine.

On the other hand, the equation for the torque of the machine can be obtained by evaluating the power balance on the machine by identifying the terms that correspond to the mechanical power output. The obtained expression is:

$$\Gamma_m = \frac{P}{2} \begin{bmatrix} i_s^{abc} \\ i_r^{abc} \end{bmatrix}^t \begin{bmatrix} 0 & N_{sr}^{abc} \\ N_{rs}^{abc} & 0 \end{bmatrix} \begin{bmatrix} i_s^{abc} \\ i_r^{abc} \end{bmatrix} \quad (3.10)$$

where P is the number of pair poles of the machine, and

$$N_{sr}^{abc} = \left\{ N_{rs}^{abc} \right\}^t = -L_{sr} \begin{bmatrix} \sin(\theta_r) & \sin(\theta_r + \frac{2\pi}{3}) & \sin(\theta_r - \frac{2\pi}{3}) \\ \sin(\theta_r - \frac{2\pi}{3}) & \sin(\theta_r) & \sin(\theta_r + \frac{2\pi}{3}) \\ \sin(\theta_r + \frac{2\pi}{3}) & \sin(\theta_r - \frac{2\pi}{3}) & \sin(\theta_r) \end{bmatrix} \quad (3.11)$$

The former equations contain a number of time-varying sinusoidal terms that make them nonlinear and hard to operate. To make the study of the machine dynamics easier, the so called Park variable transformation matrix is usually applied to them to eliminate the dependence on the rotor position and also, as it will be shown, to eliminate one of the equations for every winding group in absence of neutral conductor.

The Park variable transformation matrix for a Park reference frame (also referred as $qd0$ frame) is defined as:

$$T(\theta) = \frac{2}{3} \begin{bmatrix} \cos(\theta) & \cos(\theta - \frac{2\pi}{3}) & \cos(\theta + \frac{2\pi}{3}) \\ \sin(\theta) & \sin(\theta - \frac{2\pi}{3}) & \sin(\theta + \frac{2\pi}{3}) \\ \frac{1}{2} & \frac{1}{2} & \frac{1}{2} \end{bmatrix} \quad (3.12)$$

3.2 Induction machine dynamic equations

and its inverse is

$$T^{-1}(\theta) = \begin{bmatrix} \cos(\theta) & \sin(\theta) & 1 \\ \cos(\theta - \frac{2\pi}{3}) & \sin(\theta - \frac{2\pi}{3}) & 1 \\ \cos(\theta + \frac{2\pi}{3}) & \sin(\theta + \frac{2\pi}{3}) & 1 \end{bmatrix} \quad (3.13)$$

The transformation of the x^{abc} vector to a $qd0$ frame with angle θ is then defined as:

$$x^{qd0} \triangleq T(\theta)x^{abc} \quad (3.14)$$

Next we define the Park-transformed variables for the DFIG as:

$$\begin{cases} v_s^{qd0} \triangleq T(\theta)v_s^{abc} \\ i_s^{qd0} \triangleq T(\theta)i_s^{abc} \\ v_r^{qd0} \triangleq T(\theta - \theta_r)v_r^{abc} \\ i_r^{qd0} \triangleq T(\theta - \theta_r)i_r^{abc} \end{cases} \quad (3.15)$$

By introducing the transformed variables to the machine equations, the following equations in the $qd0$ frame are obtained:

Chapter 3 Induction machine modelling

$$\begin{aligned}
 \begin{bmatrix} v_s^{qd} \\ v_r^{qd} \end{bmatrix} &= \begin{bmatrix} \frac{3}{2}L_{ms} + L_{ls} & 0 & \frac{3}{2}L_{sr} & 0 \\ 0 & \frac{3}{2}L_{ms} + L_{ls} & 0 & \frac{3}{2}L_{sr} \\ \frac{3}{2}L_{sr} & 0 & \frac{3}{2}L_{mr} + L_{lr} & 0 \\ 0 & \frac{3}{2}L_{sr} & 0 & \frac{3}{2}L_{mr} + L_{lr} \end{bmatrix} \frac{d}{dt} \begin{bmatrix} i_s^{qd} \\ i_r^{qd} \end{bmatrix} \\
 &+ \begin{bmatrix} r_s & (\frac{3}{2}L_{ms} + L_{ls})\dot{\theta} & 0 & \frac{3}{2}L_{sr}\dot{\theta} \\ -(\frac{3}{2}L_{ms} + L_{ls})\dot{\theta} & r_s & -\frac{3}{2}L_{sr}\dot{\theta} & 0 \\ 0 & \frac{3}{2}L_{sr}(\dot{\theta} - \omega_r) & r_r & 0 \\ -\frac{3}{2}L_{sr}(\dot{\theta} - \omega_r) & 0 & -(\frac{3}{2}L_{ms} + L_{ls})(\dot{\theta} - \omega_r) & r_r \end{bmatrix} \begin{bmatrix} i_s^{qd} \\ i_r^{qd} \end{bmatrix}
 \end{aligned} \tag{3.16}$$

3.2 Induction machine dynamic equations

and

$$v_{s0} = L_{ls} \frac{di_{s0}}{dt} + r_s i_{s0} \quad (3.17)$$

$$v_{r0} = L_{lr} \frac{di_{r0}}{dt} + r_r i_{r0} \quad (3.18)$$

On the other hand, the torque can be written as a function of the current in the $qd0$ frame as:

$$\Gamma_m = \frac{9}{4} P L_{sr} (i_{sq} i_{rd} - i_{sd} i_{rq}) \quad (3.19)$$

To further simplify these equations, we define the following machine parameters:

$$\begin{cases} L_s \triangleq \frac{3}{2} L_{ms} + L_{ls} \\ L_r \triangleq \frac{3}{2} L_{mr} + L_{lr} \\ M \triangleq \frac{3}{2} L_{sr} \end{cases} \quad (3.20)$$

thus we obtain:

$$\begin{aligned} \begin{bmatrix} v_s^{qd} \\ v_r^{qd} \end{bmatrix} &= \begin{bmatrix} L_s & 0 & M & 0 \\ 0 & L_s & 0 & M \\ M & 0 & L_r & 0 \\ 0 & M & 0 & L_r \end{bmatrix} \frac{d}{dt} \begin{bmatrix} i_s^{qd} \\ i_r^{qd} \end{bmatrix} \\ &+ \begin{bmatrix} r_s & L_s \dot{\theta} & 0 & M \dot{\theta} \\ -L_s \dot{\theta} & r_s & -M \dot{\theta} & 0 \\ 0 & M(\dot{\theta} - \omega_r) & r_r & L_r(\dot{\theta} - \omega_r) \\ -M(\dot{\theta} - \omega_r) & 0 & -L_r(\dot{\theta} - \omega_r) & r_r \end{bmatrix} \begin{bmatrix} i_s^{qd} \\ i_r^{qd} \end{bmatrix}, \end{aligned} \quad (3.21)$$

$$\begin{cases} v_{s0} = L_{ls} \frac{di_{s0}}{dt} + r_s i_{s0} \\ v_{r0} = L_{lr} \frac{di_{r0}}{dt} + r_r i_{r0} \end{cases}, \quad (3.22)$$

$$\Gamma_m = \frac{3}{2} P M (i_{sq} i_{rd} - i_{sd} i_{rq}) \quad (3.23)$$

It is also interesting to obtain the expression for the stator, rotor and mechanical power exchange. According to [25], they can be written as:

Chapter 3 Induction machine modelling

$$P_m = \Gamma_m \omega_m \quad (3.24)$$

$$P_s = \frac{3}{2} (v_{sq} i_{sq} + v_{sd} i_{sd}) \quad (3.25)$$

$$P_r = \frac{3}{2} (v_{rq} i_{rq} + v_{rd} i_{rd}) \quad (3.26)$$

$$Q_s = \frac{3}{2} (v_{sq} i_{sd} - v_{sd} i_{sq}) \quad (3.27)$$

$$Q_r = \frac{3}{2} (v_{rq} i_{rd} - v_{rd} i_{rq}) \quad (3.28)$$

where P_m is the mechanical power,
 P_s is the stator active power,
 P_r is the rotor active power,
 Q_s is the stator reactive power,
 Q_r is the rotor reactive power.

The first important result, from (3.22), is that the presence of 0 component on the voltage would imply a 0 sequence current, and the sum of the current of the three phases would not be zero. Thus:

$$\begin{cases} v_{snza} + v_{snzb} + v_{snzc} + 3(v_{nsz} - v_{nws}) = 0 \\ v_{rna} + v_{rnb} + v_{rnc} + 3(v_{nr} - v_{nwr}) = 0 \end{cases} \quad (3.29)$$

and the following relations are obtained:

$$v_s^{abc} = \frac{2}{3} \begin{bmatrix} 1 & -\frac{1}{2} & -\frac{1}{2} \\ -\frac{1}{2} & 1 & -\frac{1}{2} \\ -\frac{1}{2} & -\frac{1}{2} & 1 \end{bmatrix} v_{snz}^{abc} \quad (3.30)$$

$$v_r^{abc} = \frac{2}{3} \begin{bmatrix} 1 & -\frac{1}{2} & -\frac{1}{2} \\ -\frac{1}{2} & 1 & -\frac{1}{2} \\ -\frac{1}{2} & -\frac{1}{2} & 1 \end{bmatrix} v_{rn}^{abc} \quad (3.31)$$

3.3 Steady state analysis for balanced operation

Next the equations for the steady state will be derived from the system equations considering first the case where the voltages applied to the machine have no negative nor zero sequence components.

A three phase sinusoidal signal $x^{abc}(t)$ is said to be balanced and contain only positive sequence when it is of the form [26]:

3.3 Steady state analysis for balanced operation

$$x^{abc}(t) = \sqrt{2}X \begin{bmatrix} \cos(\omega_e t + \varphi_x) \\ \cos(\omega_e t + \varphi_x - \frac{2\pi}{3}) \\ \cos(\omega_e t + \varphi_x + \frac{2\pi}{3}) \end{bmatrix} \quad (3.32)$$

where X is the root mean square (rms) of any of the phases,
 ω_e is the grid frequency,
 φ_x is the a phase angle for $t = 0$.

If the Park transformation matrix $T(\theta)$ is applied to this vector by choosing the reference angle to match the angle of the a phase as $\theta = \omega_e t + \varphi$, the obtained voltage vector is constant of the form:

$$x^{qd}(t) = T(\omega_e t + \varphi)x^{abc} = \sqrt{2}X \begin{bmatrix} \cos(\varphi_x - \varphi) \\ -\sin(\varphi_x - \varphi) \end{bmatrix} \triangleq \begin{bmatrix} x_q^{ss} \\ x_d^{ss} \end{bmatrix} \quad (3.33)$$

where x_q^{ss} and x_d^{ss} are the steady state values for the q and d components of $x^{qd}(t)$.

Particularizing the machine equations (3.21) for $\theta = \omega_e t + \varphi$ and considering the machine rotational speed ω_r to be constant and v_s^{qd} and v_r^{qd} to be balanced, it can be seen that the obtained system dynamics are linear. If the system is stable, then in steady state the current will be constant as the input voltages are constant. Thus in steady state the derivative of the current will be zero and the following relations are obtained:

$$\begin{cases} v_{sq}^{ss} = r_s i_{sq}^{ss} + \omega_e L_s i_{sd}^{ss} + \omega_e M i_{rd}^{ss} \\ 0 = r_s i_{sd}^{ss} - \omega_e L_s i_{sq}^{ss} - \omega_e M i_{rq}^{ss} \\ v_{rq}^{ss} = r_r i_{rq}^{ss} + s\omega_e L_r i_{rd}^{ss} + s\omega_e M i_{sd}^{ss} \\ v_{rd}^{ss} = r_r i_{rd}^{ss} - s\omega_e L_r i_{rq}^{ss} - s\omega_e M i_{sq}^{ss} \end{cases} \quad (3.34)$$

where $s = \frac{\omega_e - \omega_r}{\omega_e}$ is the so known slip of the machine.

Note that φ was chosen to match the angle of the stator voltage at the time $t = 0$ so that v_{sd}^{ss} became 0.

These relations are usually rewritten in a more compact form called phasor form. We define the phasor form \underline{X} of the vector $x^{qd}(t)$ in steady state as:

$$\underline{X} = \frac{1}{\sqrt{2}} (x_q^{ss} - jx_d^{ss}) \quad (3.35)$$

Thus, to obtain the phasor form of the steady state equations (3.34), the equations for each d component are multiplied by the j and subtracted from the corresponding q component and both are divided by $\sqrt{2}$ to put

Chapter 3 Induction machine modelling

everything as a function of the rms values of the corresponding sinusoidal variables:

$$V_s = (r_s + j\omega_e L_s) \underline{I}_s + j\omega_e M \underline{I}_r \quad (3.36)$$

$$\underline{V}_r = (r_r + js\omega_e L_r) \underline{I}_r + js\omega_e M \underline{I}_s \quad (3.37)$$

Also as having a different number of turns on the stator and the rotor will give a transformation ratio between both windings, usually the rotor variables may be referred to the stator side as it is usually done with transformers and squirrel cage induction machines. To the reduce the rotor variables to the rotor side, they are be divided by the ratio between the stator turns N_s and the rotor turns N_r . The following new reduced variables and parameters are defined:

$$\underline{V}'_r \triangleq \frac{N_s}{N_r} \underline{V}_r \quad (3.38)$$

$$\underline{I}'_r \triangleq \frac{N_r}{N_s} \underline{I}_r \quad (3.39)$$

$$r'_r \triangleq \left(\frac{N_s}{N_r} \right)^2 r_r \quad (3.40)$$

$$L'_r \triangleq \left(\frac{N_s}{N_r} \right)^2 L_r \quad (3.41)$$

$$\hat{M} \triangleq \frac{N_s}{N_r} M \quad (3.42)$$

Then, the steady state phasor equations can be rewritten as:

$$V_s = (r_s + j\omega_e L_s) \underline{I}_s + j\omega_e \hat{M} \underline{I}'_r \quad (3.43)$$

$$\underline{V}'_r = (r'_r + js\omega_e L'_r) \underline{I}'_r + js\omega_e \hat{M} \underline{I}_s \quad (3.44)$$

Finally as the slip of the machine also changes the rotor impedance, it is also usual to divide the rotor equation by the slip to obtain the former equation in the following form:

$$V_s = \left(r_s + j\omega_e (L_s - \hat{M}) \right) \underline{I}_s + j\omega_e \hat{M} (\underline{I}_s + \underline{I}'_r) \quad (3.45)$$

$$\frac{\underline{V}'_r}{s} = \left(\frac{r'_r}{s} + j\omega_e (L'_r - \hat{M}) \right) \underline{I}'_r + j\omega_e \hat{M} (\underline{I}_s + \underline{I}'_r) \quad (3.46)$$

3.3 Steady state analysis for balanced operation

From this point it is easy to obtain the equivalent circuit of the machine which is depicted on Figure 3.2. The parameters for the machine used in this work can be found on Table 3.1.

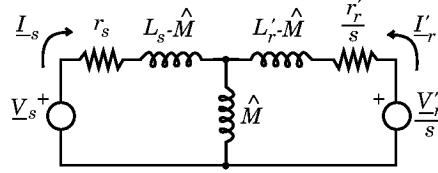


Figure 3.2: DFIG machine equivalent circuit.

From the equivalent circuit, considering that the magnetizing inductance \hat{M} will usually have a large value in comparison to the resistance of both winding sets r_s and r_r and also to the terms $L_s - \hat{M}$ and $L_r' - \hat{M}$ which are related to the leakage flux, we see that usually the it will be usually true that:

$$\underline{I}_r' \approx -\underline{I}_s, \quad (3.47)$$

$$\underline{V}_r' \approx s\underline{V}_s \quad (3.48)$$

From this relations we can also obtain an approximate relation between the stator and the rotor active power:

$$P_r \approx -sP_s \quad (3.49)$$

Thus, for operation speeds close to the synchronous speed, that is for small values of the slip s , the power through the rotor P_r is only a small fraction of the total power extracted from the wind, and thus the machine can be controlled using a power electronic converter with a small rating connected on the rotor of the machine, which is one of the important advantages of the DFIG topology in comparison to other generator types.

3.3.1 Steady state current reference calculation

Usually the output variables of the generator control will be either generator torque and the reactive power through the stator of the machine. Unfortunately, this variables may either not be measured or be nonlinearly related to other relevant system variables. Thus usually, as both currents and voltages

Chapter 3 Induction machine modelling

Parameter	Value	Units	Comments
V_s^N	690	V	Phase to phase rms
$\frac{N_s}{N_r}$	2,5	1	
P	2	1	Number of pole pairs
r_s	3e-3	Ω	
r_r'	3e-3	Ω	
$\omega_e \left(L_s - \hat{M} \right)$	20e-3	Ω	For 50 Hz
$\omega_e \left(L_r' - \hat{M} \right)$	40e-3	Ω	For 50 Hz
$\omega_e \hat{M}$	1	Ω	Calculated for 50 Hz
r_r	4,8e-4	Ω	
$\omega_e L_s$	1,02	Ω	Calculated for 50 Hz
$\omega_e L_r$	0,166	Ω	Calculated for 50 Hz
$\omega_e M$	0,4	Ω	Calculated for 50 Hz
s^N	-0.2942	1	Nominal slip.
P_s^N	562	kW (gen.)	Nominal stator active power
P_r^N	165	kW (gen.)	Nominal rotor active power
P_e^N	727	kW (gen.)	Nominal total power

Table 3.1: Induction generator parameters from [1]

3.4 Steady state analysis for unbalanced operation

are easy to measure and have approximately linear dynamics, the generator is controlled through a feedback current control loop and the reference values for the machine torque or the output power are used to calculate the current reference values using a machine model.

The steady state equations presented in the previous section can be used to calculate the reference values for the current from the desired machine torque Γ_m^* and the stator reactive power Q_s^* . To obtain the current references i_{sq}^* and i_{sd}^* , the following system of equations must be solved:

$$\begin{cases} v_{sq}^{ss} &= r_s i_{sq}^* + \omega_e L_s i_{sd}^* + \omega_e M i_{rd}^* \\ 0 &= r_s i_{sd}^* - \omega_e L_s i_{sq}^* - \omega_e M i_{rq}^* \\ \Gamma_m^* &= \frac{3}{2} P M (i_{sq}^* i_{rd}^* - i_{sd}^* i_{rq}^*) \\ Q_s^* &= \frac{3}{2} v_{sq}^{ss} i_{sd}^* \end{cases} \quad (3.50)$$

This system of equations is nonlinear and leads to multiple solutions which are hard to compute. A usual approach is to neglect the machine windings' resistance, which is usually very small in comparison to the other impedances of the machine. Doing this assumption, the equations to solve become:

$$\begin{cases} v_{sq}^{ss} &= \omega_e L_s i_{sd}^* + \omega_e M i_{rd}^* \\ 0 &= -\omega_e L_s i_{sq}^* - \omega_e M i_{rq}^* \\ \Gamma_m^* &= \frac{3}{2} P M (i_{sq}^* i_{rd}^* - i_{sd}^* i_{rq}^*) \\ Q_s^* &= \frac{3}{2} v_{sq}^{ss} i_{sd}^* \end{cases} \quad (3.51)$$

This equations are linear and the following solution for the current reference values is obtained:

$$\begin{cases} i_{rq}^* &= -\frac{2L_s}{3PMv_{sq}^{ss}} \Gamma_m^* \\ i_{rd}^* &= -\frac{2L_s}{3Mv_{sq}^{ss}} Q_s^* + \frac{v_{sq}^{ss}}{\omega_e M} \end{cases} \quad (3.52)$$

Notice that this reference calculation depends on the knowledge of the machine parameters and also needs the grid voltage to be measured.

3.4 Steady state analysis for unbalanced operation

Next it will be considered a more general operation condition where the grid voltage is no longer balanced and the voltages seen by the stator of the machine have both positive and negative sequence voltages. According to [26], a three phase sinusoidal signal is said to contain both positive and negative sequence when it is of the form:

Chapter 3 Induction machine modelling

$$\begin{aligned}
 x^{abc}(t) = x_+^{abc}(t) + x_-^{abc}(t) = \sqrt{2}X^+ \begin{bmatrix} \cos(\omega_e t + \varphi_x^+) \\ \cos(\omega_e t + \varphi_x^+ - \frac{2\pi}{3}) \\ \cos(\omega_e t + \varphi_x^+ + \frac{2\pi}{3}) \end{bmatrix} \\
 + \sqrt{2}X^- \begin{bmatrix} \cos(\omega_e t + \varphi_x^-) \\ \cos(\omega_e t + \varphi_x^- + \frac{2\pi}{3}) \\ \cos(\omega_e t + \varphi_x^- - \frac{2\pi}{3}) \end{bmatrix} \quad (3.53)
 \end{aligned}$$

where $x_+^{abc}(t)$ and $x_-^{abc}(t)$ are the positive and negative sequence vectors,
 X^+ and X^- are the root mean square (rms) of any of the
 phases for the positive and negative sequences,
 φ_x^+ and φ_x^- are the a phase angles for $t = 0$ for the positive
 and negative sequences.

Unlike in the balanced case, here it is no longer possible to find a Park reference frame where the transformed signals become constant. Fortunately, as it was shown before, considering a constant rotational speed ω_r and a constant reference frame angle, the dynamic equations of the machine (3.21) become linear. Thus the properties of the linear systems apply to the machine and in particular if the inputs to the machine (that is the voltages) can be decomposed as the sum of two terms, the resulting outputs (that is the currents) will be equal to the outputs that would be obtained for each of the input terms alone. Thus the study of the unbalanced case for the machine can be dealt as two separate balanced problems.

By applying the Park transformation to the positive sequence $x_+^{abc}(t)$ with $\theta = \omega_e t + \varphi^+$ the positive sequence in the positive reference frame $x_+^{qd}(t)$ is obtained as:

$$x_+^{qd}(t) = T(\omega_e t + \varphi^+)x_+^{abc}(t) = \sqrt{2}X^+ \begin{bmatrix} \cos(\varphi_x^+ - \varphi^+) \\ -\sin(\varphi_x^+ - \varphi^+) \end{bmatrix} \quad (3.54)$$

Doing the same for the negative sequence component $x_-^{abc}(t)$ and taking $\theta = -\omega_e t - \varphi^-$ for the negative sequence reference frame, we obtain:

$$x_-^{qd}(t) = T(-\omega_e t - \varphi^-)x_-^{abc}(t) = \sqrt{2}X^- \begin{bmatrix} \cos(\varphi_x^- - \varphi^-) \\ \sin(\varphi_x^- - \varphi^-) \end{bmatrix} \quad (3.55)$$

Separating the machine equations for the positive and the negative sequence and applying the corresponding transformation in each of them considering as in the balanced case that for a constant input the output of the

3.4 Steady state analysis for unbalanced operation

system will be constant, the equations for the positive sequence are obtained as:

$$\begin{cases} v_{sq}^+ &= r_s i_{sq}^+ + \omega_e L_s i_{sd}^+ + \omega_e M i_{rd}^+ \\ 0 &= r_s i_{sd}^+ - \omega_e L_s i_{sq}^+ - \omega_e M i_{rq}^+ \\ v_{rq}^+ &= r_r i_{rq}^+ + s \omega_e L_r i_{rd}^+ + s \omega_e M i_{sd}^+ \\ v_{rd}^+ &= r_r i_{rd}^+ - s \omega_e L_r i_{rq}^+ - s \omega_e M i_{sq}^+ \end{cases} \quad (3.56)$$

while for the negative sequence:

$$\begin{cases} v_{sq}^- &= r_s i_{sq}^- - \omega_e L_s i_{sd}^- - \omega_e M i_{rd}^- \\ 0 &= r_s i_{sd}^- + \omega_e L_s i_{sq}^- + \omega_e M i_{rq}^- \\ v_{rq}^- &= r_r i_{rq}^- - (s-2) \omega_e L_r i_{rd}^- - (s-2) \omega_e M i_{sd}^- \\ v_{rd}^- &= r_r i_{rd}^- + (s-2) \omega_e L_r i_{rq}^- + (s-2) \omega_e M i_{sq}^- \end{cases} \quad (3.57)$$

Note that again, φ^+ and φ^- were chosen to match the stator voltage angles for both sequences so that v_{sd}^+ and v_{sd}^- became 0.

As in the balanced case, these equations are usually rewritten in the more compact phasor form. A phasor for a positive sequence three phase magnitude is defined as:

$$\underline{X}_+ \triangleq \frac{1}{\sqrt{2}} (x_q^+ - j x_d^+) = X_+ (\cos(\varphi_x^+) + j \sin(\varphi_x^+)) \quad (3.58)$$

while for a negative sequence signal, the corresponding phasor is defined as:

$$\underline{X}_- \triangleq \frac{1}{\sqrt{2}} (x_q^- + j x_d^-) = X_- (\cos(\varphi_x^-) + j \sin(\varphi_x^-)) \quad (3.59)$$

Substituting in the previous steady state equations and reducing the rotor variables to the stator side using the machine transforming ratio as in the balanced case, the following phasor relations are obtained for the positive sequence:

$$V_{s+} = \left(r_s + j \omega_e (L_s - \hat{M}) \right) \underline{I}_{s+} + j \omega_e \hat{M} (\underline{I}_{s+} + \underline{I}'_{r+}) \quad (3.60)$$

$$\frac{V'_{r+}}{s} = \left(\frac{r'_r}{s} + j \omega_e (L'_r - \hat{M}) \right) \underline{I}'_{r+} + j \omega_e \hat{M} (\underline{I}_{s+} + \underline{I}'_{r+}) \quad (3.61)$$

while for the negative sequence:

Chapter 3 Induction machine modelling

$$V_{s-} = \left(r_s + j\omega_e (L_s - \hat{M}) \right) \underline{I}_{s-} + j\omega_e \hat{M} (\underline{I}_{s-} + \underline{I}'_{r-}) \quad (3.62)$$

$$\frac{V_{r-}}{s-2} = \left(\frac{r'_r}{s-2} + j\omega_e (L'_r - \hat{M}) \right) \underline{I}'_{r-} + j\omega_e \hat{M} (\underline{I}_{s-} + \underline{I}'_{r-}) \quad (3.63)$$

Again, as in the balanced case, this equations make it easy to obtain the equivalent circuit for the machine as depicted on Figure 3.3.

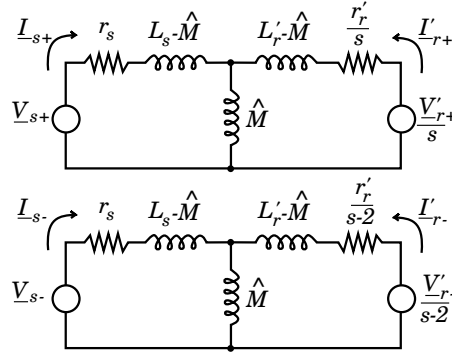


Figure 3.3: DFIG machine equivalent circuit for the unbalanced case.

Also from the equivalent circuit we see that as resistance of the windings and the leakage inductance can be considered to be small, and the magnetizing inductance to be very large, there are the following relations between the currents and the voltages:

$$\begin{cases} \underline{I}'_{r+} \approx -\underline{I}_{s+} \\ \underline{I}'_{r-} \approx -\underline{I}_{s-} \end{cases} \quad (3.64)$$

and

$$\begin{cases} \underline{V}'_{r+} \approx s \underline{V}_{s+} \\ \underline{V}'_{r-} \approx (s-2) \underline{V}_{s-} \end{cases} \quad (3.65)$$

Note that unlike in the balanced case, where having a small slip s made the voltages to apply on the rotor of the machine to be small, in the unbalanced case this is no longer true as the negative sequence voltage to be applied to compensate the negative sequence voltage of the grid will be multiplied by $s-2$ instead of s .

3.4 Steady state analysis for unbalanced operation

3.4.1 Steady state current reference calculation

As mentioned before, it will be desired for the current control reference calculation to obtain the relation between the output variables and the current and voltage on the machine. To obtain these relations, both positive and negative variables which were defined on the positive and negative reference frames, must be transformed to a common reference frame.

It can be easily proven that the Park transformation matrix $T(\theta)$ can be decomposed as the product between a conventional rotation matrix and the Park transformation matrix for a different reference angle θ_0 as:

$$T(\theta) \equiv R(\theta - \theta_0)T(\theta_0) \quad (3.66)$$

where

$$R(\theta) = \begin{bmatrix} \cos(\theta) & -\sin(\theta) & 0 \\ \sin(\theta) & \cos(\theta) & 0 \\ 0 & 0 & 1 \end{bmatrix} \quad (3.67)$$

The natural choice as a common reference frame is the stationary reference frame, which is obtained by using the Clarke transformation matrix. Thus the angle for $R(\theta)$ to transform the positive sequence variables will be $\theta = -\omega_e t - \varphi^+$ while for the negative sequence it will be $\theta = \omega_e t + \varphi^-$. By introducing these equivalences to the torque equation (3.23) and the stator reactive power equation (3.28), the following equivalences are obtained:

$$\begin{aligned} \Gamma_m = \frac{3}{2} PM \{i_s^{\alpha\beta}\}^T \begin{bmatrix} 0 & 1 \\ -1 & 0 \end{bmatrix} i_r^{\alpha\beta} &= \frac{3}{2} PM \{R(-\omega_e t - \varphi^+) i_{s+}^{qd} + R(\omega_e t + \varphi^-) i_{s-}^{qd}\}^T \\ &\cdot \begin{bmatrix} 0 & 1 \\ -1 & 0 \end{bmatrix} \left(R(-\omega_e t - \varphi^+) i_{r+}^{qd} + R(\omega_e t + \varphi^-) i_{r-}^{qd} \right) \end{aligned} \quad (3.68)$$

and

$$\begin{aligned} Q_s = \frac{3}{2} \{v_s^{\alpha\beta}\}^T \begin{bmatrix} 0 & 1 \\ -1 & 0 \end{bmatrix} i_s^{\alpha\beta} &= \frac{3}{2} \{R(-\omega_e t - \varphi^+) v_{s+}^{qd} + R(\omega_e t + \varphi^-) v_{s-}^{qd}\}^T \\ &\cdot \begin{bmatrix} 0 & 1 \\ -1 & 0 \end{bmatrix} \left(R(-\omega_e t - \varphi^+) i_{s+}^{qd} + R(\omega_e t + \varphi^-) i_{s-}^{qd} \right) \end{aligned} \quad (3.69)$$

Substituting the rotation matrix on the previous expressions, the following relations are obtained:

Chapter 3 Induction machine modelling

$$\Gamma_m = \Gamma_0 + \Gamma_{\cos} + \Gamma_{\sin} \quad (3.70)$$

$$Q_s = Q_{s0} + Q_{s\cos} + Q_{s\sin} \quad (3.71)$$

where

$$\Gamma_0 = \frac{3}{2}PM (i_{sq}^+ i_{rd}^+ - i_{sd}^+ i_{rq}^+ + i_{sq}^- i_{rd}^- - i_{sd}^- i_{rq}^-) \quad (3.72)$$

$$\Gamma_{\cos} = \frac{3}{2}PM (i_{sq}^+ i_{rd}^- - i_{sd}^+ i_{rq}^- + i_{sq}^- i_{rd}^+ - i_{sd}^- i_{rq}^+) \cos(2\omega_e t + \varphi_{V_s^+} + \varphi_{V_s^-}) \quad (3.73)$$

$$\Gamma_{\sin} = \frac{3}{2}PM (i_{sq}^+ i_{rq}^- + i_{sd}^+ i_{rd}^- - i_{sq}^- i_{rq}^+ - i_{sd}^- i_{rd}^+) \sin(2\omega_e t + \varphi_{V_s^+} + \varphi_{V_s^-}) \quad (3.74)$$

and

$$Q_{s0} = v_{sq}^+ i_{sd}^+ + v_{sq}^- i_{sd}^- \quad (3.75)$$

$$Q_{s\cos} = (v_{sq}^+ i_{sd}^- + v_{sq}^- i_{sd}^+) \cos(2\omega_e t + \varphi_{V_s^+} + \varphi_{V_s^-}) \quad (3.76)$$

$$Q_{s\sin} = (v_{sq}^+ i_{sq}^- - v_{sq}^- i_{sq}^+) \sin(2\omega_e t + \varphi_{V_s^+} + \varphi_{V_s^-}) \quad (3.77)$$

Thus unlike in the balanced three phase case, both the torque of the machine and the stator reactive power can contain sinusoidal time varying terms in steady state. Also, it can be seen that there are four control variables $\{i_{sq}^+, i_{sd}^+, i_{sq}^-, i_{sd}^-\}$ while there are six independent outputs terms $\{\Gamma_0, \Gamma_{\cos}, \Gamma_{\sin}, Q_{s0}, Q_{s\cos}, Q_{s\sin}\}$. Thus it is not possible in general to force the value for each of the six output terms but only four of them.

Usually the control of the torque will be prioritized in front to the reactive power, as it is critical for the physical integrity of the wind turbine. Thus it will be chosen to force the value of $\{\Gamma_0, \Gamma_{\cos}, \Gamma_{\sin}, Q_{s0}\}$ while the output variables $\{Q_{s\cos}, Q_{s\sin}\}$ will depend on the choice of the previous ones. As the choice of the generator torque will depend on the speed control of the turbine, and it is expected to be much slower than the dynamics of the electrical system, the sinusoidal terms Γ_{\sin} and Γ_{\cos} will be chosen to be zero.

To obtain the current needed to obtain the desired outputs, the following system of equations must be solved:

3.4 Steady state analysis for unbalanced operation

$$\begin{cases} v_{sq}^+ &= r_s i_{sq}^+ + \omega_e L_s i_{sd}^+ + \omega_e M i_{rd}^+ \\ 0 &= r_s i_{sd}^+ - \omega_e L_s i_{sq}^+ - \omega_e M i_{rq}^+ \\ v_{sq}^- &= r_s i_{sq}^- - \omega_e L_s i_{sd}^- - \omega_e M i_{rd}^- \\ 0 &= r_s i_{sd}^- + \omega_e L_s i_{sq}^- + \omega_e M i_{rq}^- \\ \Gamma_m^* &= \frac{3}{2} PM (i_{sq}^+ i_{rd}^+ - i_{sd}^+ i_{rq}^+ + i_{sq}^- i_{rd}^- - i_{sd}^- i_{rq}^-) \\ 0 &= \frac{3}{2} PM (i_{sq}^+ i_{rd}^- - i_{sd}^+ i_{rq}^- + i_{sq}^- i_{rd}^+ - i_{sd}^- i_{rq}^+) \\ 0 &= \frac{3}{2} PM (i_{sq}^+ i_{rq}^- + i_{sd}^+ i_{rd}^- - i_{sq}^- i_{rq}^+ - i_{sd}^- i_{rd}^+) \\ Q_s^* &= v_{sq}^+ i_{sd}^+ + v_{sq}^- i_{sd}^- \end{cases} \quad (3.78)$$

As in the balanced case, this system of equations is bilinear. To obtain an approximate solution, a common approach is to neglect the resistance of the generator windings. Doing this assumption, the system to solve becomes:

$$\begin{cases} v_{sq}^+ &= \omega_e L_s i_{sd}^+ + \omega_e M i_{rd}^+ \\ 0 &= -\omega_e L_s i_{sq}^+ - \omega_e M i_{rq}^+ \\ v_{sq}^- &= -\omega_e L_s i_{sd}^- - \omega_e M i_{rd}^- \\ 0 &= \omega_e L_s i_{sq}^- + \omega_e M i_{rq}^- \\ \Gamma_m^* &= \frac{3}{2} PM (i_{sq}^+ i_{rd}^+ - i_{sd}^+ i_{rq}^+ + i_{sq}^- i_{rd}^- - i_{sd}^- i_{rq}^-) \\ 0 &= \frac{3}{2} PM (i_{sq}^+ i_{rd}^- - i_{sd}^+ i_{rq}^- + i_{sq}^- i_{rd}^+ - i_{sd}^- i_{rq}^+) \\ 0 &= \frac{3}{2} PM (i_{sq}^+ i_{rq}^- + i_{sd}^+ i_{rd}^- - i_{sq}^- i_{rq}^+ - i_{sd}^- i_{rd}^+) \\ Q_s^* &= v_{sq}^+ i_{sd}^+ + v_{sq}^- i_{sd}^- \end{cases} \quad (3.79)$$

This system of equations is linear and leads to the following solution:

$$i_{rq}^+ = -\frac{2L_s}{3PM} \frac{\omega_e v_{sq}^+}{(v_{sq}^+)^2 - (v_{sq}^-)^2} \Gamma_m^* \quad (3.80)$$

$$i_{rd}^+ = -\frac{2L_s}{3M} \frac{v_{sq}^+}{(v_{sq}^+)^2 - (v_{sq}^-)^2} Q_s^* + \frac{(v_{sq}^+)^3 - (v_{sq}^-)^2 v_{sq}^+}{\omega_e M ((v_{sq}^+)^2 - (v_{sq}^-)^2)} \quad (3.81)$$

$$i_{rq}^- = \frac{2L_s}{3PM} \frac{\omega_e v_{sq}^-}{(v_{sq}^+)^2 - (v_{sq}^-)^2} \Gamma_m^* \quad (3.82)$$

$$i_{rd}^- = \frac{2L_s}{3M} \frac{v_{sq}^-}{(v_{sq}^+)^2 - (v_{sq}^-)^2} Q_s^* + \frac{(v_{sq}^-)^3 - (v_{sq}^+)^2 v_{sq}^-}{\omega_e M ((v_{sq}^+)^2 - (v_{sq}^-)^2)} \quad (3.83)$$

Thus it is possible to obtain a constant torque and the desired mean value for the reactive except in the case that the amplitude of the positive sequence is close to the amplitude of the negative sequence, which would require a current with infinite modulus. Next this condition will be further analyzed.

Chapter 3 Induction machine modelling

According to (3.53) the stator voltage signal is of the form:

$$v_s^{abc}(t) = \sqrt{2}V_{s+} \begin{bmatrix} \cos(\omega_e t + \varphi_x^+) \\ \cos(\omega_e t + \varphi_x^+ - \frac{2\pi}{3}) \\ \cos(\omega_e t + \varphi_x^+ + \frac{2\pi}{3}) \end{bmatrix} + \sqrt{2}V_{s-} \begin{bmatrix} \cos(\omega_e t + \varphi_x^-) \\ \cos(\omega_e t + \varphi_x^- + \frac{2\pi}{3}) \\ \cos(\omega_e t + \varphi_x^- - \frac{2\pi}{3}) \end{bmatrix} \quad (3.84)$$

By introducing the condition to have the same amplitude for the positive and negative sequence, that is $V_{s+} = V_{s-} = V$, into the stator voltage function, the time signal for this particular condition is obtained:

$$v_s^{abc}(t) = 2\sqrt{2}V \begin{bmatrix} \cos(\frac{\varphi^+ - \varphi^-}{2}) \cos(\omega_e t + \frac{\varphi^+ + \varphi^-}{2}) \\ \cos(\frac{\varphi^+ - \varphi^-}{2} - \frac{2\pi}{3}) \cos(\omega_e t + \frac{\varphi^+ + \varphi^-}{2}) \\ \cos(\frac{\varphi^+ - \varphi^-}{2} + \frac{2\pi}{3}) \cos(\omega_e t + \frac{\varphi^+ + \varphi^-}{2}) \end{bmatrix} \quad (3.85)$$

Note that the expression of the voltage for each phase is composed by the product of the cosine of a constant by a cosine which depends on the time which is the same for each phase. Thus, the voltage of the three phases becomes zero at the same time two times each cycle and it is impossible to have a constant power output.

Chapter 4

Permanent magnet synchronous machine modelling

4.1 Introduction

This chapter presents a model of a permanent magnet synchronous generator (PMSG) based on the work by [24] and [27]. The PMSG is a type of synchronous generator that uses permanent magnets in the rotor instead of excitation coils to create the excitation field of the machine. This type of machine is very common for small sized machines due to its compact size, high efficiency and ease to control by a VSC. However, the high price of the magnets and the mechanical difficulty of handling large magnets, make these machines less common than ones with rotor excitation coils for high power applications. Recently, the need to improve the reliability of the wind turbines to reduce the high costs of maintenance of the offshore wind farms have risen the interest in using this topology of machine and it is expected to replace the common DFIG topology in the following years. The main advantage of the PMSG is that it allows to build machines with a large number of pair poles, thus making the machine capable to work at very low speeds such as the operating speeds of the wind turbines. This way, the gearbox, which is known to be one of the most common sources of failures of the wind turbines, can be suppressed. Also, unlike the DFIG, this machine doesn't have slipping rings in the rotor, thus reducing the need of maintenance of the system. On the other hand, one important drawback to note from this machine is that unlike the DFIG it requires a full power-rated converter, thus for the same wind turbine rating the power converter of a PMSG-based WTGS will always be more expensive than that of a DFIG.

The equations of the PMSG are described and analyzed in Section 4.2. These equations are first presented in its *abc* variable form and then the Park transformation is introduced to transform the variables into the *qd0* frame which simplifies the understanding of the machine dynamics and becomes

Chapter 4 Permanent magnet synchronous machine modelling

useful to design the current controllers of the machine. Later in Section 4.3, the steady state equations of the machine are obtained from the dynamic ones.

4.2 Permanent magnet synchronous machine dynamic equations

Figure 4.1 shows the connection schematics for the PMSG machine.

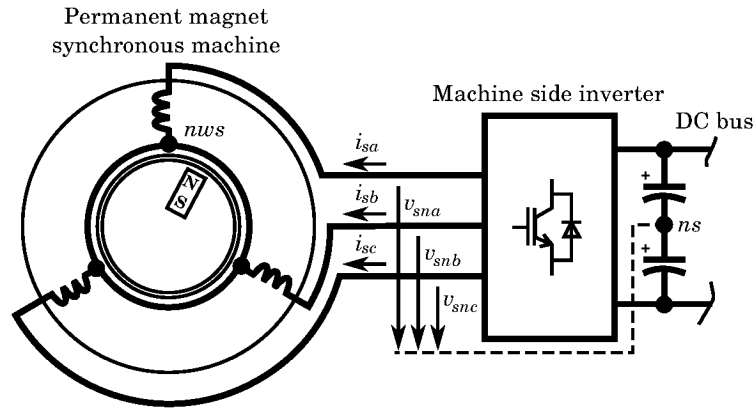


Figure 4.1: Detail of the PMSG connection for a Y configuration without neutral conductor.

We define the stator voltage vector v_s^{abc} as the vector of voltages applied to each of the machine stator windings. This vector can be written as a function of the machine side inverter voltage as:

$$v_s^{abc} = v_{sn}^{abc} + (v_{ns} - v_{nws}) \begin{bmatrix} 1 \\ 1 \\ 1 \end{bmatrix} \quad (4.1)$$

Also, as no neutral conductor is considered for the machine connection, it can be stated that the sum of the current of the three phases will be zero:

$$i_{sa} + i_{sb} + i_{sc} = 0 \quad (4.2)$$

According to [24], the relation between the voltage and the current in the machine for the PMSG can be written as:

4.2 Permanent magnet synchronous machine dynamic equations

$$v_s^{abc} = r_s i_s^{abc} + \frac{d}{dt} \lambda_s^{abc} \quad (4.3)$$

where v_s^{abc} is the stator voltage vector,
 i_s^{abc} is the stator current vector,
 λ_s^{abc} is the stator flux linkage vector,
 r_s is the resistance of a single phase of the stator windings.

Here the saturation nonlinearities will be neglected for the modelling of the magnetic circuit. On the other hand, although the inductances can also be considered not to depend on the rotor position for machines with surface mounted magnets, a more general case must be considered to properly model the behavior of a machine with buried magnets. In such model, the inductances are considered as a function of the projection of the rotor angle as:

$$\lambda_s^{abc} = ([L_1] + [L_2(\theta_r)]) i_s^{abc} + \lambda_m \begin{bmatrix} \sin(\theta_r) \\ \sin(\theta_r - \frac{2\pi}{3}) \\ \sin(\theta_r + \frac{2\pi}{3}) \end{bmatrix} \quad (4.4)$$

with

$$[L_1] = \begin{bmatrix} L_{ls} + L_A & -\frac{1}{2}L_A & -\frac{1}{2}L_A \\ -\frac{1}{2}L_A & L_{ls} + L_A & -\frac{1}{2}L_A \\ -\frac{1}{2}L_A & -\frac{1}{2}L_A & L_{ls} + L_A \end{bmatrix} \quad (4.5)$$

and

$$[L_2(\theta_r)] = -L_B \begin{bmatrix} \cos 2(\theta_r) & \cos 2(\theta_r - \frac{\pi}{3}) & \cos 2(\theta_r + \frac{\pi}{3}) \\ \cos 2(\theta_r - \frac{\pi}{3}) & \cos 2(\theta_r + \frac{\pi}{3}) & \cos 2(\theta_r) \\ \cos 2(\theta_r + \frac{\pi}{3}) & \cos 2(\theta_r) & \cos 2(\theta_r - \frac{\pi}{3}) \end{bmatrix} \quad (4.6)$$

where λ_m is the flux linkage per rotating speed unit due to the rotor magnets, L_A is a inductance term which does not depend on the rotor position and L_B is the maximum inductance value for a term that depends on the rotor position. Note that for surface mounted magnets, $L_B \approx 0$.

Differentiating the flux by the time, the following is obtained:

$$\frac{d}{dt} \lambda_s^{abc} = ([L_1] + [L_2(\theta_r)]) \frac{d}{dt} i_s^{abc} + \omega_r \frac{d}{d\theta_r} [L_2(\theta_r)] i_s^{abc} + \lambda_m \omega_r \begin{bmatrix} \cos(\theta_r) \\ \cos(\theta_r - \frac{2\pi}{3}) \\ \cos(\theta_r + \frac{2\pi}{3}) \end{bmatrix} \quad (4.7)$$

Chapter 4 Permanent magnet synchronous machine modelling

By substituting this in equation (4.3), the relation between the machine voltages and currents is obtained:

$$v_s^{abc} = \left(r_s [I_3] + \omega_r \frac{d}{d\theta_r} [L_2(\theta_r)] \right) i_s^{abc} + ([L_1] + [L_2(\theta_r)]) \frac{d}{dt} i_s^{abc} + \lambda_m \omega_r \begin{bmatrix} \cos(\theta_r) \\ \cos(\theta_r - \frac{2\pi}{3}) \\ \cos(\theta_r + \frac{2\pi}{3}) \end{bmatrix} \quad (4.8)$$

This equation is hard to analyze as it contains a series of elements which vary with time. In order to solve this problem, usually the Park variable transformation matrix (3.12) is applied to this equation [24]. The new transformed variables are defined as:

$$\begin{cases} v_s^{qd0} & \triangleq T(\theta) v_s^{abc} \\ i_s^{qd0} & \triangleq T(\theta) i_s^{abc} \end{cases} \quad (4.9)$$

By multiplying (4.8) by $T(\theta)$ the following is obtained:

$$\begin{aligned} v_s^{qd0} = [T_{qd0}(\theta)] & \left(r_s [I_3] + \omega_r \frac{d}{d\theta_r} [L_2(\theta_r)] \right) [T_{qd0}^{-1}(\theta)] i_s^{qd0} \\ & + [T_{qd0}(\theta)] ([L_1] + [L_2(\theta_r)]) [T_{qd0}^{-1}(\theta)] \frac{d}{dt} i_s^{qd0} \\ & + \omega [T_{qd0}(\theta)] ([L_1] + [L_2(\theta_r)]) \left[\frac{d}{d\theta} T_{qd0}^{-1}(\theta) \right] i_s^{qd0} \\ & + \lambda_m \omega_r [T_{qd0}(\theta)] \begin{bmatrix} \cos(\theta_r) \\ \cos(\theta_r - \frac{2\pi}{3}) \\ \cos(\theta_r + \frac{2\pi}{3}) \end{bmatrix} \end{aligned} \quad (4.10)$$

By manipulating this expression the following is obtained:

4.2 Permanent magnet synchronous machine dynamic equations

$$\begin{aligned}
 v_s^{qd0} = & \begin{bmatrix} r_s + \frac{1}{2}L_B(6\omega_r - 3\omega) \cos 2(\theta_r - \theta - \frac{\pi}{4}) & \omega(L_{ls} + \frac{3}{2}L_A) + \frac{1}{2}L_B(6\omega_r - 3\omega) \cos 2(\theta_r - \theta) & 0 \\ -\omega(L_{ls} + \frac{3}{2}L_A) + \frac{1}{2}L_B(6\omega_r - 3\omega) \cos 2(\theta_r - \theta) & r_s - \frac{1}{2}L_B(6\omega_r - 3\omega) \cos 2(\theta_r - \theta - \frac{\pi}{4}) & 0 \end{bmatrix} i_s^{qd0} \\
 & + \begin{bmatrix} L_{ls} + \frac{3}{2}L_A - \frac{3}{2}L_B \cos 2(\theta_r - \theta) & \frac{3}{2}L_B \cos 2(\theta_r - \theta - \frac{\pi}{4}) & 0 \\ \frac{3}{2}L_B \cos 2(\theta_r - \theta - \frac{\pi}{4}) & L_{ls} + \frac{3}{2}L_A + \frac{3}{2}L_B \cos 2(\theta_r - \theta) & 0 \end{bmatrix} \frac{d}{dt} i_s^{qd0} + \lambda_m \omega_r \begin{bmatrix} \cos(\theta_r - \theta) \\ -\sin(\theta_r - \theta) \\ 0 \end{bmatrix} r_s
 \end{aligned} \tag{4.11}$$

Chapter 4 Permanent magnet synchronous machine modelling

On the other hand, a much simpler equation can be obtained by using the rotor position as the transformation angle, that is $\theta \triangleq \theta_r$:

$$v_s^{qd0} = \begin{bmatrix} r_s & \omega_r (L_{ls} + \frac{3}{2} (L_A + L_B)) & 0 \\ -\omega_r (L_{ls} + \frac{3}{2} (L_A - L_B)) & r_s & 0 \\ 0 & 0 & r_s \end{bmatrix} i_s^{qd0} + \begin{bmatrix} L_{ls} + \frac{3}{2} (L_A - L_B) & 0 & 0 \\ 0 & L_{ls} + \frac{3}{2} (L_A + L_B) & 0 \\ 0 & 0 & L_{ls} \end{bmatrix} \frac{d}{dt} i_s^{qd0} + \lambda_m \omega_r \begin{bmatrix} 1 \\ 0 \\ 0 \end{bmatrix} \quad (4.12)$$

Note that the zero sequence component 0 is decoupled from the qd components, thus this equation can be split as:

$$v_s^{qd} = \begin{bmatrix} r_s & \omega_r (L_{ls} + \frac{3}{2} (L_A + L_B)) \\ -\omega_r (L_{ls} + \frac{3}{2} (L_A - L_B)) & r_s \end{bmatrix} i_s^{qd} + \begin{bmatrix} L_{ls} + \frac{3}{2} (L_A - L_B) & 0 \\ 0 & L_{ls} + \frac{3}{2} (L_A + L_B) \end{bmatrix} \frac{d}{dt} i_s^{qd} + \lambda_m \omega_r \begin{bmatrix} 1 \\ 0 \end{bmatrix} \quad (4.13)$$

and

$$v_s^0 = r_s i_s^0 + L_{ls} \frac{d}{dt} i_s^0 \quad (4.14)$$

This equations can also be manipulated to obtain an explicit equation for the current derivatives:

$$\frac{d}{dt} i_s^{qd} = \begin{bmatrix} \frac{-r_s}{L_{ls} + \frac{3}{2} (L_A - L_B)} & \frac{-\omega_r (L_{ls} + \frac{3}{2} (L_A + L_B))}{L_{ls} + \frac{3}{2} (L_A - L_B)} \\ \frac{\omega_r (L_{ls} + \frac{3}{2} (L_A - L_B))}{L_{ls} + \frac{3}{2} (L_A + L_B)} & \frac{-r_s}{L_{ls} + \frac{3}{2} (L_A + L_B)} \end{bmatrix} i_s^{qd} - \lambda_m \omega_r \begin{bmatrix} \frac{1}{L_{ls} + \frac{3}{2} (L_A - L_B)} \\ 0 \end{bmatrix} + \begin{bmatrix} \frac{1}{L_{ls} + \frac{3}{2} (L_A - L_B)} & 0 \\ 0 & \frac{1}{L_{ls} + \frac{3}{2} (L_A + L_B)} \end{bmatrix} v_s^{qd} \quad (4.15)$$

and

$$\frac{d}{dt} i_s^0 = -\frac{r_s}{L_s} i_s^0 + \frac{1}{L_{ls}} v_s^0 \quad (4.16)$$

4.2 Permanent magnet synchronous machine dynamic equations

Here no neutral conductor will be considered, in this case the sum of the abc currents will be zero thus there will be no zero sequence current and only the qd subsystem equations will need to be taken into account.

On the other hand, the equation for the torque of the generator can be obtained by calculating the mechanical power of the generator, P_M and dividing it by the mechanical speed. To obtain the mechanical power, the stator voltage (4.8) is multiplied by the rotor voltage and the terms which do not correspond to the losses due to the joule effect and the power stored in the inductances are identified as:

$$P_M = \omega_r \left\{ i_s^{abc} \right\}^T \frac{d}{d\theta_r} [L_2(\theta_r)] i_s^{abc} + \lambda_m \omega_r \left\{ i_s^{abc} \right\}^T \begin{bmatrix} \cos(\theta_r) \\ \cos(\theta_r - \frac{2\pi}{3}) \\ \cos(\theta_r + \frac{2\pi}{3}) \end{bmatrix} \quad (4.17)$$

By applying the Park transformation to this equation, it can be put as a function of the $qd0$ variables as:

$$\begin{aligned} P_M &= \omega_r \left\{ i_s^{qd0} \right\}^T \left[T_{qd0}^{-1}(\theta) \right]^T \frac{d}{d\theta_r} [L_2(\theta_r)] \left[T_{qd0}^{-1}(\theta) \right] i_s^{qd0} \\ &\quad + \lambda_m \omega_r \left\{ i_s^{qd0} \right\}^T \left[T_{qd0}^{-1}(\theta) \right]^T \begin{bmatrix} \cos(\theta_r) \\ \cos(\theta_r - \frac{2\pi}{3}) \\ \cos(\theta_r + \frac{2\pi}{3}) \end{bmatrix} \\ &= \omega_r \left\{ i_s^{qd0} \right\}^T \begin{bmatrix} \frac{3}{2} 3L_B \cos 2(\theta_r - \theta - \frac{\pi}{2}) & \frac{3}{2} 3L_B \cos 2(\theta_r - \theta) & 0 \\ \frac{3}{2} 3L_B \cos 2(\theta_r - \theta) & -\frac{3}{2} 3L_B \cos 2(\theta_r - \theta - \frac{\pi}{2}) & 0 \\ 0 & 0 & 0 \end{bmatrix} i_s^{qd0} \\ &\quad + \frac{3}{2} \lambda_m \omega_r \left\{ i_s^{qd0} \right\}^T \begin{bmatrix} \cos(\theta_r - \theta) \\ -\sin(\theta_r - \theta) \\ 0 \end{bmatrix} \end{aligned} \quad (4.18)$$

This can be further simplified by identifying the stator flux as:

$$P_M = \frac{3}{2} \omega_r (\lambda_{sd} i_{sq} - \lambda_{sq} i_{sd}) \quad (4.19)$$

where

Chapter 4 Permanent magnet synchronous machine modelling

$$\lambda_s^{qd0} = \begin{bmatrix} L_{ls} + \frac{3}{2}L_A - \frac{3}{2}L_B \cos 2(\theta_r - \theta) & \frac{3}{2}L_B \cos 2(\theta_r - \theta - \frac{\pi}{4}) & 0 \\ \frac{3}{2}L_B \cos 2(\theta_r - \theta - \frac{\pi}{4}) & L_{ls} + \frac{3}{2}L_A + \frac{3}{2}L_B \cos 2(\theta_r - \theta) & 0 \\ 0 & 0 & L_{ls} \end{bmatrix} i_s^{qd0} + \lambda_m \begin{bmatrix} \sin(\theta_r - \theta) \\ \cos(\theta_r - \theta) \\ 0 \end{bmatrix} \quad (4.20)$$

By dividing this equation by the mechanical speed, the torque equation is obtained as:

$$\Gamma_m = \frac{3}{2}P (\lambda_{sd}i_{sq} - \lambda_{sq}i_{sd}) \quad (4.21)$$

Also, by using the rotor position as the Park reference angle, a further simplified equation is obtained:

$$\Gamma_m = \frac{3}{2}P \left(\left\{ i_s^{qd0} \right\}^T \begin{bmatrix} 0 & 3L_B & 0 \\ 3L_B & 0 & 0 \\ 0 & 0 & 0 \end{bmatrix} i_s^{qd0} + \lambda_m \left\{ i_s^{qd0} \right\}^T \begin{bmatrix} 1 \\ 0 \\ 0 \end{bmatrix} \right) = \frac{3}{2}P (\lambda_m i_{sq} + 3L_B i_{sq} i_{sd}) \quad (4.22)$$

Note that for a machine with surface mounted magnets, where $L_B \approx 0$, the torque of the machine only depends on the q component of the stator current, while for a machine with buried magnets, the torque also depends on the product of the q and d components. Thus for a surface mounted machine, there is only one possible value of the q current to obtain the desired torque on the machine while the d component can be adjusted for other purposes while for a machine with buried magnets, it becomes harder to decide the proper value for the current for a desired torque.

Finally, to write the equations in a more compact form in the qd base, usually the following new parameters are defined:

$$L_q \triangleq L_{ls} + \frac{3}{2}(L_A - L_B) \quad (4.23)$$

$$L_d \triangleq L_{ls} + \frac{3}{2}(L_A + L_B) \quad (4.24)$$

Then, the equations of the machine become:

4.3 Steady state analysis

$$v_s^{qd} = \begin{bmatrix} r_s & \omega_r L_d \\ -\omega_r L_q & r_s \end{bmatrix} i_s^{qd} + \begin{bmatrix} L_q & 0 \\ 0 & L_d \end{bmatrix} \frac{d}{dt} i_s^{qd} + \lambda_m \omega_r \begin{bmatrix} 1 \\ 0 \end{bmatrix} \quad (4.25)$$

and

$$\Gamma_m = \frac{3}{2} P (\lambda_m i_{sq} + (L_d - L_q) i_{sq} i_{sd}) \quad (4.26)$$

Also the current derivatives in explicit form become:

$$\frac{d}{dt} i_s^{qd} = \begin{bmatrix} \frac{-r_s}{L_q} & \frac{-\omega_r L_d}{L_q} \\ \frac{\omega_r L_q}{L_d} & \frac{-r_s}{L_d} \end{bmatrix} i_s^{qd} - \lambda_m \omega_r \begin{bmatrix} \frac{1}{L_q} \\ 0 \end{bmatrix} + \begin{bmatrix} \frac{1}{L_q} & 0 \\ 0 & \frac{1}{L_d} \end{bmatrix} v_s^{qd} \quad (4.27)$$

4.3 Steady state analysis

In this section the characteristics for the steady state operation of the PMSG will be obtained from the machine equations.

Note from (4.26) that in order to obtain a constant torque from the machine, the stator current must be constant in the qd reference frame. Under such condition, the current derivatives are zero and thus the following relation between the voltages and the currents is obtained:

$$\begin{cases} v_{sq}^{ss} = r_s i_{sq}^{ss} + \omega_r L_q i_{sd}^{ss} + \lambda_m \omega_r \\ v_{sd}^{ss} = -\omega_r L_d i_{sq}^{ss} + r_s i_{sd}^{ss} \end{cases} \quad (4.28)$$

In the case of a machine with surface mounted magnets, where $L_B \approx 0$ and thus $L \triangleq L_q \approx L_d$, this system of equations can be put in a more compact form by combining both equations into a single complex equation using phasors as:

$$\underline{V}_s = (r_s + j\omega_r L) \underline{I}_s + \frac{1}{\sqrt{2}} \lambda_m \omega_r \quad (4.29)$$

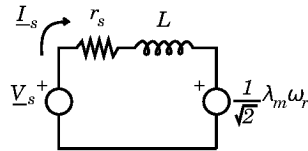


Figure 4.2: PMSG machine equivalent circuit.

Chapter 5

Power converter and grid-side system modelling

5.1 Introduction

This chapter analyzes the modelling of the voltage source converter and the dynamics of the AC grid connection of the converter. The voltage source back-to-back converter is an “AC to DC to AC” converter with two three-phase inverters with IGBT switching devices connected through a DC bus with large capacitors in parallel, hence the name of voltage source in contrast to the so called current source converters with large inductors in series.

The high frequency switching capabilities of the IGBTs make it possible to use high frequency pulse-width modulation (PWM) techniques which allow high performance control of the current while minimizing the low frequency current harmonics without the need of large passive filters. The high frequency modulation also makes it possible to use a low frequency model of the converter and to approximate the behaviour of the inverters as ideal controllable voltage sources. This is possible thanks to the low pass nature of the physical systems connected to the inverters, which have the ability to filter the high frequency content of the voltage applied by the inverters. This allows to apply the well known linear system analysis tools to study the system and design its controllers.

When studying the dynamics and the design of the control of the converter, a common approach is to divide the design problem into a series of small problems. Namely, as the capacity of the DC bus is large, its dynamics are usually slower than the dynamics of the current of the generator and the current on the AC grid side. Thus, usually the design of the generator current controllers, the AC grid side current and the DC bus voltage is dealt separately.

This chapter is organized as follows: first in Section 5.2, the equations of the dynamics of the DC bus, which later will be used to design the regulator

Chapter 5 Power converter and grid-side system modelling

of the DC bus voltage, are presented. Later, in Section 5.3, the dynamic equations of the AC grid side connection of the converter are discussed. As in the Chapter 3, the steady state analysis is first presented for the balanced case, as used in the conventional vector control, and later it is generalized for the unbalanced case. Unlike in Chapter 3, the calculation of the current reference values is not dealt here but in Chapter 9, where several issues arising from the traditional approaches will be discussed. Finally, the equations for a dynamic model of a transformer are presented in Section 5.6.

5.2 DC bus dynamic equations

The schematic diagram of the DC bus is shown in Figure 5.1. Notice the diagram is represented for the DFIG configuration, in the case of the converter of the PMSG, the diagram is equivalent by replacing the rotor variables by the stator equivalents. Using the Kirchoff laws to analyze the circuit, the following set of equations is obtained:

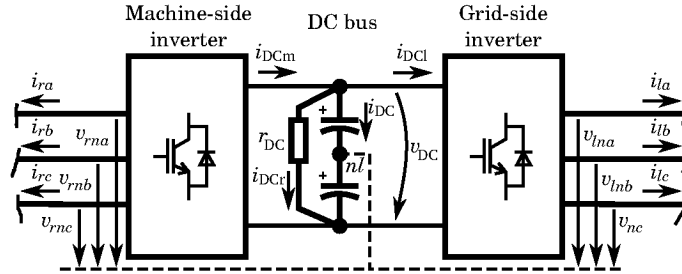


Figure 5.1: Back-to-back converter DC bus

$$\begin{cases} \frac{d}{dt}V_{DC} = \frac{1}{C}i_{DC} \\ V_{DC} = r_{DC}i_{DCr} \\ i_{DCm} = i_{DC} + i_{DCt} + i_{DCr} \end{cases} \quad (5.1)$$

5.3 Grid side system dynamic equations

where V_{DC} is the DC bus voltage,
 C is the DC bus capacity,
 r_{DC} is the so called DC bus discharge resistor,
 i_{DC} is the current flowing through the DC bus capacitors,
 i_{DCr} is the current flowing through the DC bus discharge resistor,
 i_{DCl} is the current flowing through the DC side of the grid side inverter,
 i_{DCm} is the current coming from the the DC side of the machine side inverter.

Solving the previous equations, the derivative of the DC bus voltage can be put as a function of the DC bus voltage and the current from both inverters as:

$$\frac{d}{dt}V_{DC} = \frac{1}{C} \left(-\frac{1}{r_{DC}}V_{DC} + i_{DCm} - i_{DCl} \right) \quad (5.2)$$

Here the inverters are considered to have an ideal behavior with no losses. Thus, the current on the DC side of each inverter is related to the power flowing through the AC side of the inverter. For the grid side of the converter the following relation is obtained:

$$\left\{ v_l^{abc} \right\}^T i_l^{abc} = V_{DC} i_{DCl} \quad (5.3)$$

On the other hand, the machine side equations depending on which winding set is connected to the converter. In the case of a DFIG the following relation is obtained:

$$\left\{ v_r^{abc} \right\}^T i_r^{abc} = -V_{DC} i_{DCm} \quad (5.4)$$

while for a PMSG:

$$\left\{ v_s^{abc} \right\}^T i_s^{abc} = -V_{DC} i_{DCm} \quad (5.5)$$

5.3 Grid side system dynamic equations

Figure 5.2 depicts the connection of a three phase voltage source converter to the grid.

Chapter 5 Power converter and grid-side system modelling

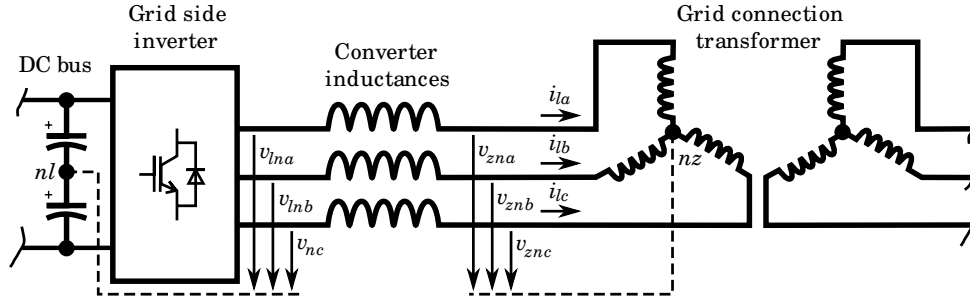


Figure 5.2: Grid side converter connection

Here the grid at the point of connection of the wind turbine will be considered to have an infinite short-circuit power. Thus, the voltage at the point of connection of the converter inductances v_z^{abc} will be assumed to not depend on the current injected to the grid i_l^{abc} . This hypothesis can arguably be made when designing the current control loops and the current reference calculation procedure as the controller will measure v_z^{abc} and will be able to adapt to the changes in v_z^{abc} due to the injected current. Also, the hypothesis can be relaxed when simulating the system behaviour by modelling the grid connection transformer. A model of transformer with two secondary windings will be presented later. This type of transformer is common in DFIG wind turbines where the stator and the converter of the rotor are connected to different secondary windings of the grid connection transformer.

By applying the Kirchoff laws to the grid side circuit, we obtain the following relations:

$$v_{ln}^{abc} + (v_{nl} - v_{nz}) \begin{bmatrix} 1 \\ 1 \\ 1 \end{bmatrix} = r_l i_l^{abc} + L_l \frac{d}{dt} i_l^{abc} + v_{zn}^{abc} \quad (5.6)$$

where v_{ln}^{abc} is the voltage between the inverter terminals and the DC bus neutral,
 v_{zn}^{abc} is the voltage between the transformer terminals and its neutral,
 v_{nz} is the voltage of the neutral point of the secondary windings of the grid connection transformer,
 v_{nl} is the voltage of the neutral point of the DC bus,
 r_l is the resistance of the grid connection impedance,
 L_l is the inductance of the grid connection impedance.

5.3 Grid side system dynamic equations

Also if no neutral conductor is considered, it can be stated that:

$$i_{la} + i_{lb} + i_{lc} = 0 \quad (5.7)$$

By summing the a , b and c equations in (5.6) and introducing (5.7), the following relation between the voltages is obtained:

$$v_{nl} - v_{nz} = \frac{1}{3} \left(\underbrace{v_{zna} + v_{znb} + v_{znc}}_{3v_{z0}} - \underbrace{v_{lna} - v_{lnb} - v_{lnc}}_{3v_{l0}} \right) = v_{z0} - v_{l0} \quad (5.8)$$

where v_{l0} is the so called homopolar sequence of v_{ln}^{abc} ,
 v_{z0} is the homopolar sequence of v_{zn}^{abc} .

We define:

$$v_l^{abc} \equiv \begin{bmatrix} v_{la} \\ v_{lb} \\ v_{lc} \end{bmatrix} \triangleq \begin{bmatrix} v_{lna} - \frac{1}{3}v_{l0} \\ v_{lnb} - \frac{1}{3}v_{l0} \\ v_{lnc} - \frac{1}{3}v_{l0} \end{bmatrix} \quad (5.9)$$

and

$$v_z^{abc} \equiv \begin{bmatrix} v_{za} \\ v_{zb} \\ v_{zc} \end{bmatrix} \triangleq \begin{bmatrix} v_{zna} - \frac{1}{3}v_{z0} \\ v_{znb} - \frac{1}{3}v_{z0} \\ v_{znc} - \frac{1}{3}v_{z0} \end{bmatrix} \quad (5.10)$$

thus obtaining:

$$v_l^{abc} = r_l i_l^{abc} + L_l \frac{d}{dt} i_l^{abc} + v_z^{abc} \quad (5.11)$$

Next, in order to simplify as much as possible the study of these equations, usually the Park transformation matrix is applied to the variables, allowing to suppress one of the equations when there is no neutral conductor and also transforming the time varying sinusoidal signals in steady state in constants if the right parameters of the transformation are chosen.

The Park variable transformation matrix can be defined as:

$$T(\theta) = \frac{2}{3} \begin{bmatrix} \cos(\theta) & \cos(\theta - \frac{2\pi}{3}) & \cos(\theta + \frac{2\pi}{3}) \\ \sin(\theta) & \sin(\theta - \frac{2\pi}{3}) & \sin(\theta + \frac{2\pi}{3}) \\ \frac{1}{2} & \frac{1}{2} & \frac{1}{2} \end{bmatrix} \quad (5.12)$$

which has an inverse of the form:

Chapter 5 Power converter and grid-side system modelling

$$T^{-1}(\theta) = \begin{bmatrix} \cos(\theta) & \sin(\theta) & 1 \\ \cos(\theta - \frac{2\pi}{3}) & \sin(\theta - \frac{2\pi}{3}) & 1 \\ \cos(\theta + \frac{2\pi}{3}) & \sin(\theta + \frac{2\pi}{3}) & 1 \end{bmatrix} \quad (5.13)$$

we define the Park transformed variable x^{qd0} of a three phase abc signal x^{abc} as:

$$x^{qd0} \triangleq T(\theta)x^{abc} \quad (5.14)$$

We introduce the Park transformation matrix to the circuit equations by multiplying equation (5.11) by $T(\theta)$, obtaining:

$$T(\theta)v_l^{abc} = r_l T(\theta)i_l^{abc} + L_l T(\theta) \frac{d}{dt} i_l^{abc} + T(\theta)v_z^{abc} \quad (5.15)$$

By operating with this expression and introducing (5.14) we obtain:

$$v_l^{qd0} = \begin{bmatrix} r_l & L_l \dot{\theta} & 0 \\ -L_l \dot{\theta} & r_l & 0 \\ 0 & 0 & r_l \end{bmatrix} i_l^{qd0} + L_l \frac{d}{dt} i_l^{qd0} + v_z^{qd0} \quad (5.16)$$

From (5.9) and (5.10), we know that both v_l^{abc} and v_z^{abc} don't have 0 component. Thus from (5.16) we know that i_{l0} will be 0 and the equation for the 0 component can be suppressed:

$$v_l^{qd} = \begin{bmatrix} r_l & L_l \dot{\theta} \\ -L_l \dot{\theta} & r_l \end{bmatrix} i_l^{qd} + L_l \frac{d}{dt} i_l^{qd} + v_z^{qd} \quad (5.17)$$

this equation can be put in the conventional linear system state space representation as:

$$\frac{d}{dt} i_l^{qd} = \begin{bmatrix} -\frac{r_l}{L_l} & -\dot{\theta} \\ \dot{\theta} & -\frac{r_l}{L_l} \end{bmatrix} i_l^{qd} + \frac{1}{L_l} v_l^{qd} - \frac{1}{L_l} v_z^{qd} \quad (5.18)$$

one particular interesting choice for θ is $\theta \equiv 0$, the so know stationary reference frame, in this reference frame usually qd is replaced by $\alpha\beta$ and the following equation is obtained:

$$v_l^{\alpha\beta} = r_l i_l^{\alpha\beta} + L_l \frac{d}{dt} i_l^{\alpha\beta} + v_z^{\alpha\beta} \quad (5.19)$$

5.4 Steady state analysis for balanced operation

A $x^{abc}(t)$ sinusoidal three phase positive sequence signal can be defined as [26]:

$$x^{abc}(t) = \sqrt{2}X \begin{bmatrix} \cos(\omega_e t + \varphi_x) \\ \cos(\omega_e t + \varphi_x - \frac{2\pi}{3}) \\ \cos(\omega_e t + \varphi_x + \frac{2\pi}{3}) \end{bmatrix} \quad (5.20)$$

From equation (5.18) we see that the dynamics of the grid-side system are linear. If we assume that they are also stable, we know that for a sinusoidal input, in steady state the system output will be also sinusoidal of the same frequency. Also, from (5.18) we see that the a , b and c components are decoupled from each other, thus for a positive sequence grid voltage v_z^{abc} and a positive sequence converter voltage v_l^{abc} , the current will also become a positive sequence signal in steady state.

By applying the Park transformation matrix $T(\theta)$ to a generic positive sequence signal $x^{abc}(t)$ with $\theta \triangleq \omega_e t + \varphi$ we obtain:

$$x^{qd0}(t) = T(\omega_e t + \varphi)x^{abc} = \sqrt{2}X \begin{bmatrix} \cos(\varphi_x - \varphi) \\ -\sin(\varphi_x - \varphi) \\ 0 \end{bmatrix} \quad (5.21)$$

Thus if all the voltage inputs are positive sequence signals, by using this reference frame all steady state signals become constants and in steady state the following simplified relations are obtained:

$$\begin{cases} v_{lq}^{ss} - v_{zq}^{ss} = r_l i_{lq}^{ss} + L_l \omega_e i_{ld}^{ss} \\ v_{ld}^{ss} - v_{zd}^{ss} = r_l i_{ld}^{ss} - L_l \omega_e i_{lq}^{ss} \end{cases} \quad (5.22)$$

As this equation is linear and invertible it becomes easy to solve the steady state voltage for a given steady state current and vice versa.

These equations are also often written in the more conventional phasor form. We define the phasor \underline{X} as:

$$\underline{X} \triangleq \frac{1}{\sqrt{2}} (x_q^{ss} - jx_d^{ss}) \quad (5.23)$$

by combining both expressions in (5.22) we obtain:

$$\underline{V}_l - \underline{V}_z = (r_l + j\omega_e L_l) \underline{I}_l \quad (5.24)$$

Usually it is interesting to solve for the steady state variables for a given power output instead of a given current. To do that, two power equations

Chapter 5 Power converter and grid-side system modelling

must be added to the system to be solved. These equations usually will come from the power balance on the converter or the power balance at the grid connection point of the converter inductances.

According to the instantaneous power theory [25], the instantaneous active and reactive power can be written as a function of the instantaneous voltage and current as:

$$P = \frac{3}{2} (v_q i_q + v_d i_d) \quad (5.25)$$

$$Q = \frac{3}{2} (v_q i_d - v_d i_q) \quad (5.26)$$

Considering the power balance on the AC side of the converter we have:

$$\begin{cases} P_l = \frac{3}{2} (v_{lq}^{ss} i_{lq}^{ss} + v_{ld}^{ss} i_{ld}^{ss}) \equiv 3\Re\{\underline{V}_l \underline{I}_l^*\} \\ Q_l = \frac{3}{2} (v_{lq}^{ss} i_{ld}^{ss} - v_{ld}^{ss} i_{lq}^{ss}) \equiv 3\Im\{\underline{V}_l \underline{I}_l^*\} \end{cases} \quad (5.27)$$

whilst for the grid connection point of the converter inductances we have:

$$\begin{cases} P_z = \frac{3}{2} (v_{zq}^{ss} i_{lq}^{ss} + v_{zd}^{ss} i_{ld}^{ss}) \equiv 3\Re\{\underline{V}_z \underline{I}_l^*\} \\ Q_z = \frac{3}{2} (v_{zq}^{ss} i_{ld}^{ss} - v_{zd}^{ss} i_{lq}^{ss}) \equiv 3\Im\{\underline{V}_z \underline{I}_l^*\} \end{cases} \quad (5.28)$$

5.5 Steady state analysis for unbalanced operation

A $x^{abc}(t)$ sinusoidal three phase signal with positive and negative sequence components can be defined as sum of a positive sequence signal plus a negative sequence signal, which in turn is equivalent to a positive sequence signal with two of the three phases permuted [26]:

$$x^{abc}(t) = \sqrt{2}X^+ \begin{bmatrix} \cos(\omega_e t + \varphi_x^+) \\ \cos(\omega_e t + \varphi_x^+ - \frac{2\pi}{3}) \\ \cos(\omega_e t + \varphi_x^+ + \frac{2\pi}{3}) \end{bmatrix} + \sqrt{2}X^- \begin{bmatrix} \cos(\omega_e t + \varphi_x^-) \\ \cos(\omega_e t + \varphi_x^- + \frac{2\pi}{3}) \\ \cos(\omega_e t + \varphi_x^- - \frac{2\pi}{3}) \end{bmatrix} \quad (5.29)$$

Unlike in the positive sequence case, here it is no longer possible to apply the Park transformation to obtain a steady state constant value for the system variables.

To overcome this problem, the additivity property of the linear systems can be taken into account as the obtained current output for a combination of positive and negative voltage inputs is equal to the sum of the current

5.5 Steady state analysis for unbalanced operation

output that would be obtained for both the positive and negative sequence alone. Thus solving the steady state problem for the relation between the voltage and the current can be dealt by solving two independent balanced problems.

If we apply the Park transformation matrix with $\theta \triangleq \omega_e t + \varphi^+$ to the positive sequence we obtain:

$$x_+^{qd}(t) = T(\omega_e t + \varphi^+) x_+^{abc}(t) = \sqrt{2} X^+ \begin{bmatrix} \cos(\varphi_x^+ - \varphi^+) \\ -\sin(\varphi_x^+ - \varphi^+) \end{bmatrix} \quad (5.30)$$

Whilst if we apply the Park transformation matrix with $\theta \triangleq -\omega_e t - \varphi^-$ to the negative sequence we obtain:

$$x_-^{qd}(t) = T(-\omega_e t - \varphi^-) x_-^{abc}(t) = \sqrt{2} X^- \begin{bmatrix} \cos(\varphi_x^- - \varphi^-) \\ \sin(\varphi_x^- - \varphi^-) \end{bmatrix} \quad (5.31)$$

As in the balanced case, the simplified steady state equations can be obtained for both positive and negative sequences:

$$\begin{cases} v_{lq}^+ - v_{zq}^+ = r_l i_{lq}^+ + L_l \omega_e i_{ld}^+ \\ v_{ld}^+ - v_{zd}^+ = r_l i_{ld}^+ - L_l \omega_e i_{lq}^+ \end{cases} \quad (5.32)$$

and

$$\begin{cases} v_{lq}^- - v_{zq}^- = r_l i_{lq}^- - L_l \omega_e i_{ld}^- \\ v_{ld}^- - v_{zd}^- = r_l i_{ld}^- + L_l \omega_e i_{lq}^- \end{cases} \quad (5.33)$$

These expressions, can also be rewritten in a more compact notation by using phasors. Here we define a phasor for the positive sequence as:

$$\underline{X}_+ \triangleq \frac{1}{\sqrt{2}} (x_q^+ - j x_d^+) \quad (5.34)$$

whilst for the negative sequence we define:

$$\underline{X}_- \triangleq \frac{1}{\sqrt{2}} (x_q^- + j x_d^-) \quad (5.35)$$

Thus the steady state equations can be rewritten as:

$$\begin{cases} \underline{V}_{l+} - \underline{V}_{z+} = (r + j\omega_e) \underline{I}_{l+} \\ \underline{V}_{l-} - \underline{V}_{z-} = (r + j\omega_e) \underline{I}_{l-} \end{cases} \quad (5.36)$$

As in the positive sequence case, usually it will be desired to solve for the current values as a function of the desired power balance. To compute

Chapter 5 Power converter and grid-side system modelling

the power, both positive and negative sequence must be put on the same reference frame as:

$$P = \frac{3}{2} \{v^{\alpha\beta}\}^T \begin{bmatrix} 1 & 0 \\ 0 & 1 \end{bmatrix} i^{\alpha\beta} = \frac{3}{2} \{R(-\omega_e t - \varphi^+) v_+^{qd} + R(\omega_e t + \varphi^-) v_-^{qd}\}^T \cdot \begin{bmatrix} 1 & 0 \\ 0 & 1 \end{bmatrix} \left(R(-\omega_e t - \varphi^+) i_+^{qd} + R(\omega_e t + \varphi^-) i_-^{qd} \right) \quad (5.37)$$

$$Q = \frac{3}{2} \{v^{\alpha\beta}\}^T \begin{bmatrix} 0 & 1 \\ -1 & 0 \end{bmatrix} i^{\alpha\beta} = \frac{3}{2} \{R(-\omega_e t - \varphi^+) v_+^{qd} + R(\omega_e t + \varphi^-) v_-^{qd}\}^T \cdot \begin{bmatrix} 0 & 1 \\ -1 & 0 \end{bmatrix} \left(R(-\omega_e t - \varphi^+) i_+^{qd} + R(\omega_e t + \varphi^-) i_-^{qd} \right) \quad (5.38)$$

where $R(\theta)$ is a rotation matrix defined as:

$$R(\theta) = \begin{bmatrix} \cos(\theta) & -\sin(\theta) \\ \sin(\theta) & \cos(\theta) \end{bmatrix} \quad (5.39)$$

it can be easily proven that:

$$T(\theta) \equiv \begin{bmatrix} R(\theta) & 0 \\ 0 & 1 \end{bmatrix} T(0) \quad (5.40)$$

In the three phase positive sequence case, the sum of the power of the three phases is constant in steady state as a result of the symmetrical angle difference between the variables of each phase. In the unbalanced case, with both positive and negative sequence components, this is no longer true and both active and reactive power may contain time-varying sinusoidal components.

If the active power is put as a function of the steady state voltage and current, the following expression is obtained:

$$P = P_0 + P_{\cos} + P_{\sin} \quad (5.41)$$

where

$$P_0 = \frac{3}{2} (v_q^+ i_q^+ + v_d^+ i_d^+ + v_q^- i_q^- + v_d^- i_d^-) \quad (5.42)$$

$$P_{\cos} = \frac{3}{2} (v_q^+ i_q^- + v_d^+ i_d^- + v_q^- i_q^+ + v_d^- i_d^+) \cos(2\omega_e t + \varphi^+ + \varphi^-) \quad (5.43)$$

$$P_{\sin} = \frac{3}{2} (-v_q^+ i_d^- + v_d^+ i_q^- + v_q^- i_d^+ - v_d^- i_q^+) \sin(2\omega_e t + \varphi^+ + \varphi^-) \quad (5.44)$$

5.6 Three phase transformer with two sets of secondary windings

whilst for the reactive power:

$$Q = Q_0 + Q_{\cos} + Q_{\sin} \quad (5.45)$$

where

$$Q_0 = \frac{3}{2} (v_q^+ i_d^+ - v_d^+ i_q^+ + v_q^- i_d^- - v_d^- i_q^-) \quad (5.46)$$

$$Q_{\cos} = \frac{3}{2} (v_q^+ i_d^- - v_d^+ i_q^- + v_q^- i_d^+ - v_d^- i_q^+) \cos(2\omega_e t + \varphi^+ + \varphi^-) \quad (5.47)$$

$$Q_{\sin} = \frac{3}{2} (v_q^+ i_q^- + v_d^+ i_d^- - v_q^- i_q^+ - v_d^- i_d^+) \sin(2\omega_e t + \varphi^+ + \varphi^-) \quad (5.48)$$

The use of this equations to obtain the current reference value for a given desired active and reactive power will be discussed in Chapter 9.

5.6 Three phase transformer with two sets of secondary windings

The basic scheme of a three phase transformer with two secondary winding sets can be seen in Figure 5.3, where the subindex 1,2' and 2'' represents the primary and the first and the second secondary.

The equivalent electric circuit of the transformer can be seen in Figure 5.4. By applying the Kirchoff laws to this circuit, the following equations can be obtained:

$$u_{1k} = r_1 i_{1k} + L_{l1} \frac{di_{1k}}{dt} + e_{1k} \quad \text{for } k = a, b, c \quad (5.49)$$

$$u_{2'k} = r_{2'} i_{2'k} + L_{l2'} \frac{di_{2'k}}{dt} + e_{2'k} \quad \text{for } k = a, b, c \quad (5.50)$$

$$u_{2''k} = r_{2''} i_{2''k} + L_{l2''} \frac{di_{2''k}}{dt} + e_{2''k} \quad \text{for } k = a, b, c \quad (5.51)$$

$$i_{1ek} = i_{1k} - \frac{1}{r_{Fe}} e_{1k} \quad \text{for } k = a, b, c \quad (5.52)$$

and

Chapter 5 Power converter and grid-side system modelling

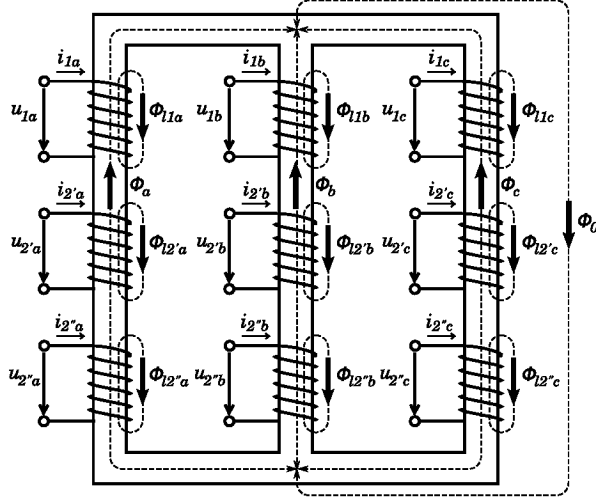


Figure 5.3: Three phase transformer with three-leg core and two secondary winding sets.

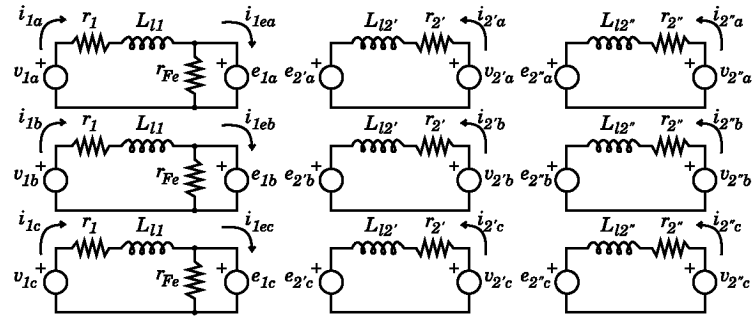


Figure 5.4: Equivalent electric circuit of the three phase transformer with two secondary winding sets.

5.6 Three phase transformer with two sets of secondary windings

$$e_{1k} = \frac{d\lambda_{1k}}{dt} = N_1 \frac{d\phi_k}{dt} \quad \text{for } k = a, b, c \quad (5.53)$$

$$e_{2'k} = \frac{d\lambda_{2'k}}{dt} = N_{2'} \frac{d\phi_k}{dt} \quad \text{for } k = a, b, c \quad (5.54)$$

$$e_{2''k} = \frac{d\lambda_{2''k}}{dt} = N_{2''} \frac{d\phi_k}{dt} \quad \text{for } k = a, b, c \quad (5.55)$$

where u_{jk} is the voltage of the k -th phase of the j -th winding set,
 i_{jk} is the current of the k -th phase of the j -th winding set,
 Φ_{jk} is the flux flowing through the k -th phase of the j -th winding set,
 λ_{jk} is the flux linkage of the k -th phase of the j -th winding set,
 e_{jk} is the electromotive force of the k -th phase of the j -th winding set,
 r_j is the resistance of the j -th winding set,
 L_{lj} is the flux leakage inductance of the j -th winding set,
 r_{Fe} is the resistance that models the core losses of the transformer.

The equivalent magnetic circuit of the transformer can be found in Figure 5.5. Notice that even though the transformer depicted in Figure 5.3 corresponds to a three-legged transformer, a homopolar flux Φ_0 is considered. Thus, depending on the value given to the reluctance of the homopolar path, the model can properly describe the dynamics of a four legged transformer as well. The following equations can be obtained from this circuit:

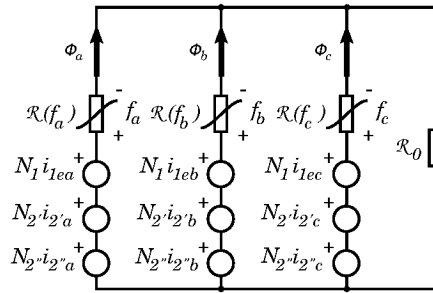


Figure 5.5: Equivalent magnetic circuit of the three phase transformer with two secondary winding sets.

Chapter 5 Power converter and grid-side system modelling

$$f_k = \Re(f_k)\phi_k \quad \text{per } k = a, b, c \quad (5.56)$$

and

$$f_k = N_1 i_{1ek} + N_2 i_{2'k} + N_2 i_{2''k} - \Re_0 \sum_{i=a,b,c} \phi_i \quad \text{for } k = a, b, c \quad (5.57)$$

where f_k is the magnetomotive force of the k -th leg,
 N_j is the number of coil turns around the core of the j -th winding set,
 $\Re(f_k)$ is the reluctance of the flux path through the k -th leg,
 \Re_0 is the reluctance corresponding the homopolar path.

In order to take into account the non-linear magnetic properties of the core, the following equation is used to describe the relation between the reluctance and the magnetomotive force [28]:

$$\Re(f)^{-1} = \frac{K_1}{\left(1 + \left(\frac{|f|}{f_{sat}}\right)^p\right)^{\frac{1}{p}}} + K_2 \quad (5.58)$$

Notice that for $f \approx 0$, this function becomes:

$$\lim_{f \rightarrow 0} \Re(f)^{-1} = K_1 + K_2 \quad (5.59)$$

whereas for $f \rightarrow \infty$, it becomes:

$$\lim_{f \rightarrow \infty} \Re(f)^{-1} = K_2 \quad (5.60)$$

Thus, K_1 and K_2 are two characteristic parameters that can be used to adjust the limit values of the inverse of the reluctance, while f_{sat} and p can be used to adjust the transition between both values. Insights on how to adjust this parameters for an existing transformer can be found in [28].

Part II

Control of wind turbines

Chapter 6

Conventional DFIG vector control

6.1 Introduction

This chapter analyzes a conventional vector control approach for the control of the current of the DFIG and the AC grid side connection of the converter.

The basic idea behind the conventional vector control approach is that by applying the Park transformation matrix to the system variables and choosing the derivative of the Park reference angle to match the angle of the time-varying sinusoidal magnitudes of the system, most system variables become constant in steady state. Thus, it is possible to use the proportional-integrator (PI) and other well known low pass controllers, meant to track step-wise reference signals and reject step-wise disturbances, to control the current.

The chapter is organized as follows: first, the design of the current control for the DFIG is analyzed in Section 6.2 using the DFIG model obtained in Chapter 3.

Next, Section 6.3 is divided in two parts: first, in the Section 6.3.1 the design of the DC bus voltage regulator using the equations obtained in Section 5.2 is described. This regulator will also be used in Chapter 7 and 8 where the vector current controllers for the generator and the AC grid side will be replaced by designs meant for unbalanced operation.

Later, Section 6.3.2 analyses the design of the current controllers for the AC grid side of the converter using the model obtained in Section 5.3.

Finally, Section 6.4 presents a validation study of a simulation model for a DFIG-based WTGS controlled using conventional vector control using existing experimental measurements from a voltage sag test performed on a real large scale wind turbine.

Chapter 6 Conventional DFIG vector control

6.2 Machine side control

It was shown in Chapter 3 that assuming a balanced state, by using a Park reference with the same angular speed as the grid frequency, all the Park-transformed magnitudes of the DFIG become constant in steady state. This way, it is possible to design the current controllers using the well known controller design tools meant for regulation problems instead of having to design more complex controllers to track general time-varying reference signals.

By choosing $\dot{\theta}$ to match the grid frequency ω_e , the DFIG machine equations (3.21) become:

$$\begin{bmatrix} v_{sq} \\ v_{sd} \\ v_{rq} \\ v_{rd} \end{bmatrix} = \begin{bmatrix} L_s & 0 & M & 0 \\ 0 & L_s & 0 & M \\ M & 0 & L_r & 0 \\ 0 & M & 0 & L_r \end{bmatrix} \frac{d}{dt} \begin{bmatrix} i_{sq} \\ i_{sd} \\ i_{rq} \\ i_{rd} \end{bmatrix} + \begin{bmatrix} r_s & L_s \omega_e & 0 & M \omega_e \\ -L_s \omega_e & r_s & -M \omega_e & 0 \\ 0 & M(\omega_e - \omega_r) & r_r & L_r(\omega_e - \omega_r) \\ -M(\omega_e - \omega_r) & 0 & -L_r(\omega_e - \omega_r) & r_r \end{bmatrix} \begin{bmatrix} i_{sq} \\ i_{sd} \\ i_{rq} \\ i_{rd} \end{bmatrix} \quad (6.1)$$

and also

$$\begin{cases} \Gamma_m = \frac{3}{2} PM (i_{sq} i_{rd} - i_{sd} i_{rq}) \\ Q_s = \frac{3}{2} (v_{sq} i_{sd} - v_{sd} i_{sq}) \end{cases} \quad (6.2)$$

It was shown in Section 3.3.1 that it is possible to calculate the rotor current that allows to obtain the desired machine torque and stator reactive power for a given grid voltage. As the torque is rarely measured due to the complexity and the cost of this type of sensor, usually a current reference will be calculated from the torque and reactive power reference signals as:

$$\begin{cases} i_{rq}^* = -\frac{2L_s}{3PMv_{sq}^{ss}} \Gamma_m^* \\ i_{rd}^* = -\frac{2L_s}{3Mv_{sq}^{ss}} Q_s^* + \frac{v_{sq}^{ss}}{\omega_e M} \end{cases} \quad (6.3)$$

where v_{sq}^{ss} is the measured grid voltage.

This reference will then be fed to a feedback current controller which will compare the desired current with the measured one and will calculate the voltage to be applied to the machine through PWM modulation of the DC bus voltage.

6.2 Machine side control

According to the machine equations in (6.1), there exist an important coupling between the stator and rotor magnitudes and also between q and d , thus this coupling may interfere the performance of the control loops if decoupled controllers are to be used. To cope with this problem, it has been suggested to use the following decoupling feedback loop [3]:

$$\begin{bmatrix} v_{rq} \\ v_{rd} \end{bmatrix} = \begin{bmatrix} \hat{v}_{rq} + (\omega_e - \omega_r) M i_{sd} + (\omega_e - \omega_r) L_r i_{rd} \\ \hat{v}_{rd} - (\omega_e - \omega_r) M i_{sq} - (\omega_e - \omega_r) L_r i_{rq} \end{bmatrix} = \begin{bmatrix} \hat{v}_{rq} + (\omega_e - \omega_r) \lambda_{rd} \\ \hat{v}_{rd} - (\omega_e - \omega_r) \lambda_{rq} \end{bmatrix} \quad (6.4)$$

where \hat{v}_{rq} and \hat{v}_{rd} are the outputs of two single input single output (SISO) controllers fed with the error for the q and the d current errors.

To test the effectiveness of this decoupling loop, a simulation of the current response under different conditions is performed. A voltage step on \hat{v}_{rd} is applied while maintaining \hat{v}_{rq} equal to zero (see Figure 6.1) for 1.000 and 1.900 min^{-1} machine speeds. The simulations are performed in two different models, one that uses an averaged converter model and another which simulates the PWM for a switching frequency of 3 kHz. In both simulations the controllers are implemented in discrete time with a sampling frequency matching the switching frequency of the converter.

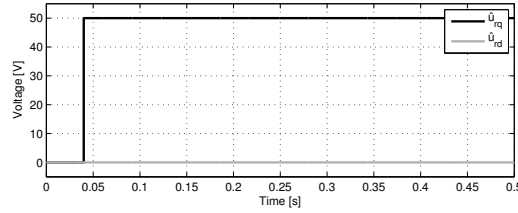


Figure 6.1: Simulated voltage step to test the decoupling feedback loop used by the conventional vector controller of the DFIG

The resulting simulated rotor voltages, which contain \hat{v}_r^{qd} plus the decoupling terms can be seen in Figure 6.2, the rotor current is shown in Figure 6.3. Note that for all the cases, $v_{rq} \approx \hat{v}_{rq}$, thus the decoupling loop does not change significantly the q component of the current as i_{rd} remains small compared to i_{rq} , which is a good result. On the other hand, notice that the decoupling voltage v_{rd} needed to keep i_{rd} small is very large even compared to v_{rq} .

Thus, even though the decoupling loop works, it becomes apparent that care must be taken when designing the current feedback controllers as for

Chapter 6 Conventional DFIG vector control

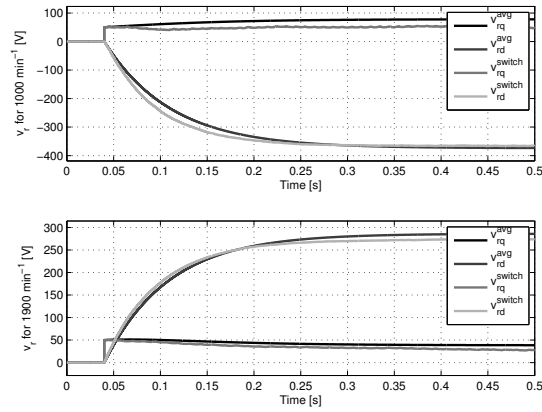


Figure 6.2: Rotor voltage applied to test the decoupling feedback loop used by the conventional vector controller of the DFIG

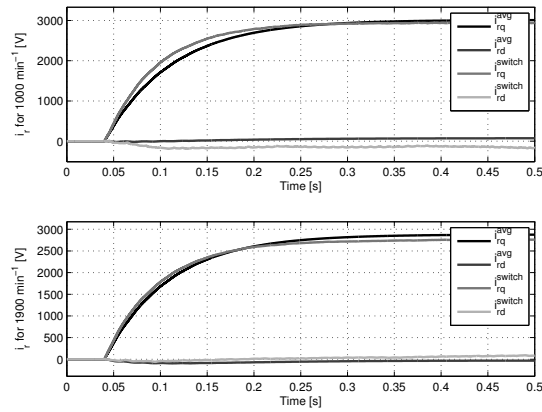


Figure 6.3: Evolution of the rotor current for the test of the decoupling feedback loop used by the conventional vector controller of the DFIG

6.2 Machine side control

instance, the decoupling loop may easily interfere with the proper operation of them and significantly reduce their performance.

Assuming the decoupling feedback loop to completely decouple the magnitudes, the rotor current dynamics become:

$$\begin{bmatrix} \hat{v}_{rq} \\ \hat{v}_{rd} \end{bmatrix} = \begin{bmatrix} L_r & 0 \\ 0 & L_r \end{bmatrix} \frac{d}{dt} \begin{bmatrix} i_{rq} \\ i_{rd} \end{bmatrix} + \begin{bmatrix} r_r & 0 \\ 0 & r_r \end{bmatrix} \begin{bmatrix} i_{rq} \\ i_{rd} \end{bmatrix} \quad (6.5)$$

By applying the Laplace transformation to this equation, the following transfer function between the voltage and the current is obtained. As both q and d have the same transfer function, here for the sake of simplicity only the q component equations will be displayed:

$$G(s) = \frac{i_{rq}(s)}{\hat{v}_{rq}(s)} = \frac{1}{L_r s + r_r} \quad (6.6)$$

Then a PI controller can be used to control this system. One common way to adjust the parameters of this controller is based in the so called Internal Model Control (IMC) [29]. This method consists in designing the current controller transfer function $K(s)$ by multiplying the open loop transfer function that allows to obtain the desired closed loop transfer function by the inverse of the system transfer function (when possible). Here, the desired closed loop transfer function $T(s)^*$ is taken as:

$$T(s)^* = \frac{i_{rq}(s)}{i_{rq}^*(s)} = \frac{1}{\tau s + 1} \quad (6.7)$$

where $i_{rq}^*(s)$ is the rotor current reference signal and τ is the desired closed loop time constant of the system.

Then, the open loop transfer function that allows to obtain this is:

$$L(s)^* = \frac{\hat{v}_{rq}(s)}{e_{rq}(s)} = \frac{1}{\tau s} \quad (6.8)$$

where $e_{rq}(s)$ is the rotor current error signal.

Thus, the controller can be obtained as:

$$K(s) = G^{-1}(s)L(s)^* = \frac{L_r s + r_r}{1} \frac{1}{\tau s} = \frac{\frac{L_r}{\tau} s + \frac{r_r}{\tau}}{s} \quad (6.9)$$

Note that this corresponds to the transfer function of a proportional-integrator (PI) controller:

$$K(s) = \frac{K_P s + K_I}{s} \quad (6.10)$$

Chapter 6 Conventional DFIG vector control

where K_P and K_I are the so called proportional and integral gains:

$$\begin{cases} K_P = \frac{L_r}{\tau} \\ K_I = \frac{r_r}{\tau} \end{cases} \quad (6.11)$$

A simulation is performed on the system to test the performance obtained using the designed controllers. Time constant for the design of the PI controllers is chosen so that the steady state is reached in 6 ms. A step change of the i_{rq}^* reference is simulated from 0 to the value needed to have the nominal torque. The operating point before the reference change corresponds to the machine spinning at the 1.900 min^{-1} and the nominal grid voltage applied to the stator. The current response is shown in Figure 6.4 for the averaged and the switching simulation models. Notice the rise time of the current response corresponds to the design parameter. On the other hand, note also that the 0 steady state error is not reached in that time as there exists a small error which vanishes at a slow rate because of the dynamics introduced by the decoupling loop.

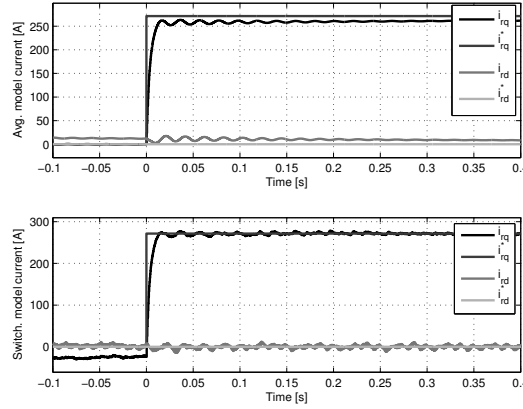


Figure 6.4: Evolution of the rotor current of the DFIG to a step reference change when using conventional vector control

A diagram representation for this control scheme can be found in Figure 6.5. Note that for the sake of completeness the PLL used to synchronize the reference frame to the grid magnitudes has been included in the lower-right side.

6.3 Grid-side control

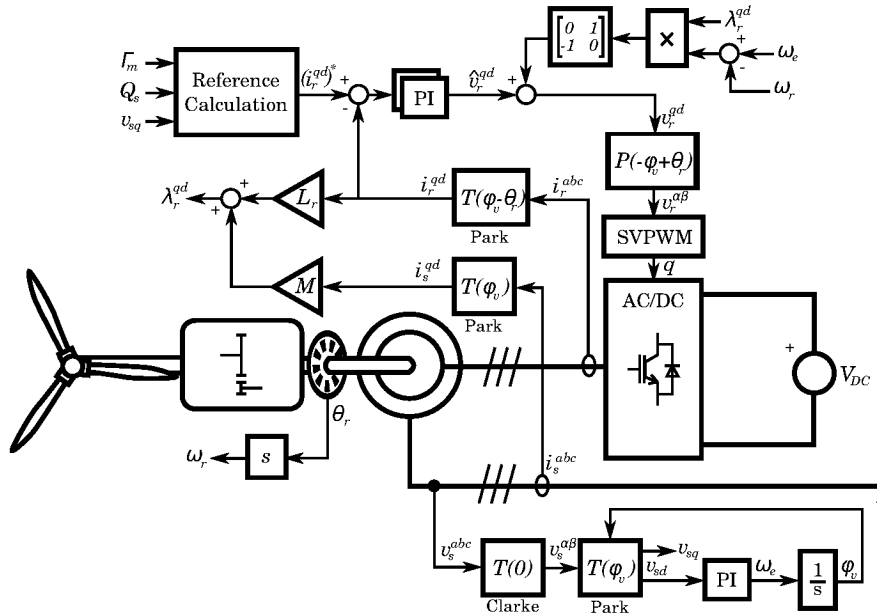


Figure 6.5: DFIG conventional vector control

6.3 Grid-side control

6.3.1 DC bus voltage regulation

The dynamics of the DC bus are described by the equation (5.2). Applying the Laplace transformation to this equation, the following relation is obtained:

$$V_{DC}(s) = \underbrace{\frac{r_{DC}}{r_{DC}Cs + 1}}_{G_d(s)} i_{DCm} - \underbrace{\frac{r_{DC}}{r_{DC}Cs + 1}}_{G(s)} i_{DCI} \quad (6.12)$$

where $G(s)$ and $G_d(s)$ are the transfer functions between the grid side current and the machine side current and the DC bus voltage respectively.

Here, a one degree of freedom controller will be used to control the DC bus voltage through the grid-side current. To do so, the output of the DC bus voltage controller, i_{DCI}^* will be transformed into a power reference value which will be fed to the current control loops of the AC side of the inverter as:

$$P_l^* = V_{DC} i_{DCl}^*$$

Chapter 6 Conventional DFIG vector control

In order to simplify the design of the voltage controller, a model reduction will be applied by considering the current control loops will to have an ideal instantaneous response ($i_{DCI} = i_{DCI}^*$). Thus, the current control loops will be designed to have a faster response than the voltage control loop.

Considering a generic controller DC bus voltage controller $K(s)$, the closed loop transfer function between the DC bus reference signal and its actual value, $T(s)$, and the closed transfer function between the machine side current and the DC bus voltage are:

$$T(s) = \frac{V_{DC}(s)}{V_{DC}^*(s)} = \frac{-K(s)}{Cs - K(s) + \frac{1}{r_{DC}}} \quad (6.13)$$

and

$$S(s) = \frac{V_{DC}(s)}{i_{DCm}(s)} = \frac{1}{Cs - K(s) + \frac{1}{r_{DC}}} \quad (6.14)$$

From the equation of $T(s)$ it can be seen that if $r_{DC} \approx \infty$, a simple proportional $K(s)$ will make the transfer function be approximately equal to one at zero frequency (for $s = j\omega|_{\omega=0}$) and thus the system will have a nearly zero steady state error for constant reference values. On the other hand, from $S(s)$ it can be seen that with such controller, $i_{DCm} \neq 0$ will lead to a DC bus voltage error as $S(0) \neq 0$. To avoid this drawback, a controller with an integrator, such as a PI controller, can be used:

$$K(s) = \frac{K_p s + K_i}{s} \quad (6.15)$$

this leads to:

$$\begin{cases} T(s) = \frac{-\frac{K_p}{C}s - \frac{K_i}{C}}{D(s)} \\ S(s) = \frac{\frac{1}{C}s}{D(s)} \end{cases} \quad (6.16)$$

where

$$D(s) = s^2 + \frac{1}{C} \left(\frac{1}{r_{DC}} - K_p \right) s - \frac{K_i}{C} \quad (6.17)$$

Then, the parameters of the PI controller can be adjusted to tune the system response. Both $T(s)$ and $S(s)$ two poles which are the same, the damping ζ and the natural frequency ω_n of such poles can be related to the PI controller gains as:

6.3 Grid-side control

$$\begin{cases} K_p = -2C\zeta\omega_n + \frac{1}{r_{DC}} \\ K_i = -C\omega_n^2 \end{cases} \quad (6.18)$$

where

$$\begin{aligned} D(s) &= s^2 + 2\zeta\omega_n s + \omega_n^2 \\ &= \left(s + \omega_n \left(\zeta - \sqrt{\zeta^2 - 1}\right)\right) \left(s + \omega_n \left(\zeta + \sqrt{\zeta^2 - 1}\right)\right) \end{aligned} \quad (6.19)$$

To test the performance of this controller, a simulation of the response is performed using a simplified model of the DC bus fed by two ideal current sources corresponding to the machine and the grid side inverters. The DC bus voltage reference value is changed stepwise from 900 V to the nominal value of 1.338 V at $t = 0,04$ s and the power injected by the machine side inverter to the DC bus is also changed from 0 to 300 kW at $t = 0,5$ s. The simulated evolution of the DC bus magnitudes is shown in Figure 6.6. The voltage regulator PI controller parameters are adjusted to have $\zeta = 1$ and $\omega_n = 32$ rad/s. Using this parameters, the poles of the system have a settling time of approximately 0,1 s. Notice, though, that the obtained settling time for both simulated changes is slightly slower due to the zeros of the closed loop transfer function.

6.3.2 AC side current control

It was shown in Chapter 5 that assuming a balanced state, the AC side magnitudes of the grid side inverter become constants in steady state by matching the Park reference angle to the grid frequency. Under such condition, the equations of the grid side of the inverter (5.17) become:

$$v_l^{qd} = \begin{bmatrix} r_l & Ll\omega_e \\ -Ll\omega_e & r_l \end{bmatrix} i_l^{qd} + L_l \frac{d}{dt} i_l^{qd} + v_z^{qd} \quad (6.20)$$

Also, in Section 5.4 it was shown that if the grid side voltages are considered to be independent from the inverter output current, it is possible to calculate a reference current that leads to the desired active and reactive power output using (9.7). This way a current reference is calculated from the power reference and the current is controlled by a feedback loop which compares the reference with the actual current and decides the voltage to be applied by the inverter using PWM modulation of the DC bus voltage. The current reference values are calculated as:

Chapter 6 Conventional DFIG vector control

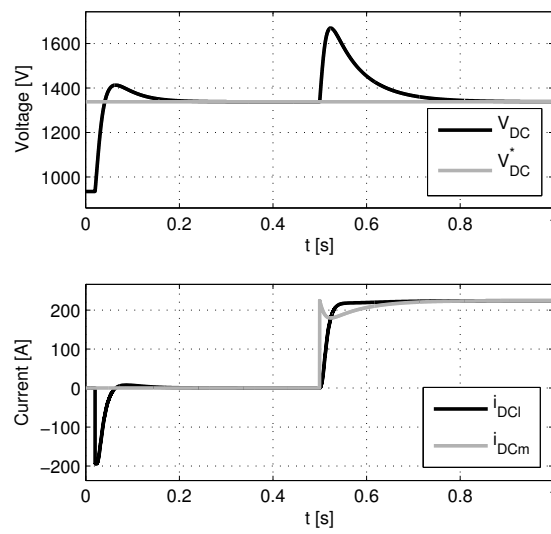


Figure 6.6: Evolution DC bus voltage and the current on the DC side of the machine and the grid side inverter for a change in the DC bus voltage reference value and a change in the power injected to the DC bus by the machine inverter.

6.3 Grid-side control

$$\begin{cases} i_{lq}^* = \frac{2}{3} \frac{P_z^*}{v_{zq}^{ss}} \\ i_{le}^* = \frac{2}{3} \frac{Q_z^*}{v_{zq}^{ss}} \end{cases} \quad (6.21)$$

From (6.20) we see that there is a coupling between the q and d variables which may have an adverse effect on the performance of the current control loops if two SISO controllers are used and the coupling is neglected. To avoid this adverse effect, a feedback decoupling loop have been suggested to be used [3]. This can also be combined with a feed-forward to compensate for the grid voltage as:

$$\begin{bmatrix} v_{lq} \\ v_{ld} \end{bmatrix} = \begin{bmatrix} \hat{v}_{lq} + \omega_e L_l \dot{i}_{ld} + v_{zq} \\ \hat{v}_{ld} - \omega_e L_l \dot{i}_{lq} \end{bmatrix} \quad (6.22)$$

where \hat{v}_l^{qd} is the output of a pair of SISO controllers fed with the error between the reference current and its actual value.

To test the proper operation of the decoupling feedback loop, the evolution of the current to a step voltage input applied in \hat{v}_{lq} is simulated using an averaged model of the converter and a discrete time implementation of the controller with a sampling frequency of 3 kHz. The voltage step can be seen in Figure 6.7 and the evolution of the current is shown in Figure 6.8. The evolution of the current shows that the decoupling is not perfect during the transient, however the maximum value reached by i_{ld} is approximately 500 times lower than the DC gain of i_{lq} , thus it is arguable to assume q and d to be successfully decoupled using the decoupling feedback and use SISO current controllers for each component of i_l^{qd} . On the other hand, notice from Figure 6.7 that although the voltage step is applied on \hat{v}_{lq} , the actual applied voltage v_{lq} is much smaller than v_{ld} , which means that the choice to control i_{lq} through v_{lq} might not be the best possible choice.

Assuming the decoupling and the feed-forward to completely compensate for the grid voltage and the coupling between q and d , the dynamics of the system become:

$$\hat{v}_l^{qd} = r_l i_l^{qd} + L_l \frac{d}{dt} i_l^{qd} \quad (6.23)$$

Then, two independent SISO controllers can be designed to control the q and d components of the current through the corresponding components of the voltage. By transforming the previous equation through Laplace, the following transfer function between the grid side current and the inverter voltage is obtained:

Chapter 6 Conventional DFIG vector control

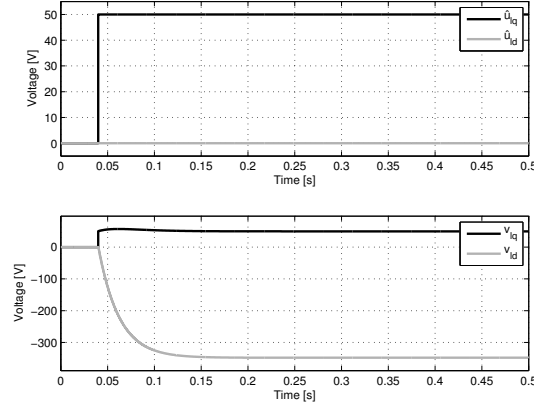


Figure 6.7: Simulated voltage step to test the decoupling feedback loop used by the conventional vector controller of the AC side current control. *Upper graph:* evolution of \hat{v}_l^{qd} . *Lower graph:* evolution of v_l^{qd} including the voltage applied by the decoupling feedback loop.

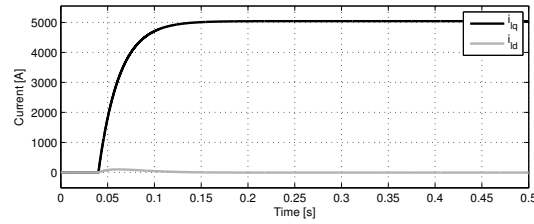


Figure 6.8: Evolution of the AC side current for the test of the decoupling feedback loop used by the conventional vector controller of the AC side current control.

6.4 Validation of the simulation model using experimental results

$$G(s) = \frac{i_{lq}(s)}{v_{lq}(s)} = \frac{1}{L_l s + r_r} \quad (6.24)$$

As in the case of the DFIG current controllers described in the previous section, the IMC technique can be used to tune the parameters of two PI controllers for the current [29]. The transfer function for such controllers is:

$$K(s) = \frac{K_P s + K_I}{s} \quad (6.25)$$

with:

$$\begin{cases} K_P = \frac{L_r}{\tau} \\ K_I = \frac{r_r}{\tau} \end{cases} \quad (6.26)$$

where τ is the time constant of the expected closed loop transfer function of the system, that is:

$$T(s) = \frac{i_{lq}(s)}{i_{lq}^*(s)} = \frac{1}{\tau s + 1} \quad (6.27)$$

To test the performance of the current loops, a simulation of the response of the system to a step change in the reference value of i_{lq} . The current loops are adjusted to have a settling time of 6 ms, that is $\tau = 2$ ms and the amplitude of the reference step is 350 A, which approximately corresponds to the current needed to have the nominal output power from the converter. The evolution of i_l^{qd} can be seen in Figure 6.9 and i_l^{abc} is also shown in Figure 6.10. Notice that the performance specification is met as the resulting time constant of the response is approximately 6 ms. The evolution of the applied voltage compared to the grid voltage is also shown in Figure 6.11. Notice that the v_{ld} is very small in comparison to v_{lq} due to the need to compensate the grid voltage.

The complete scheme for the grid side controller can be seen in Figure 6.12.

6.4 Validation of the simulation model using experimental results

In order to test the matching between the model of the WTGS with conventional vector control and the behaviour of a real wind turbine, the response of the system to a symmetrical voltage sag is simulated and the results are compared to experimental measurements from a test performed on a real

Chapter 6 Conventional DFIG vector control

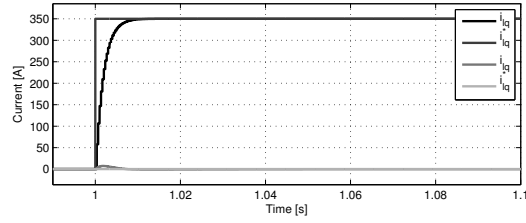


Figure 6.9: Evolution of the AC side current of the grid side inverter in the qd reference frame to a step reference change when using conventional vector control

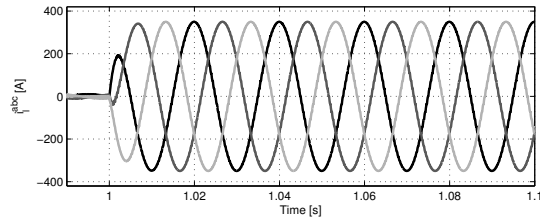


Figure 6.10: Evolution of the AC side current of the grid side inverter in the abc reference frame to a step reference change when using conventional vector control

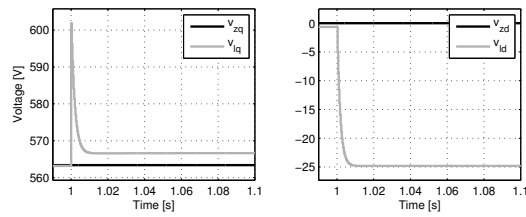


Figure 6.11: Evolution of the voltage applied on the AC side of the grid side inverter due to a step change in the current reference when using conventional vector control

6.4 Validation of the simulation model using experimental results

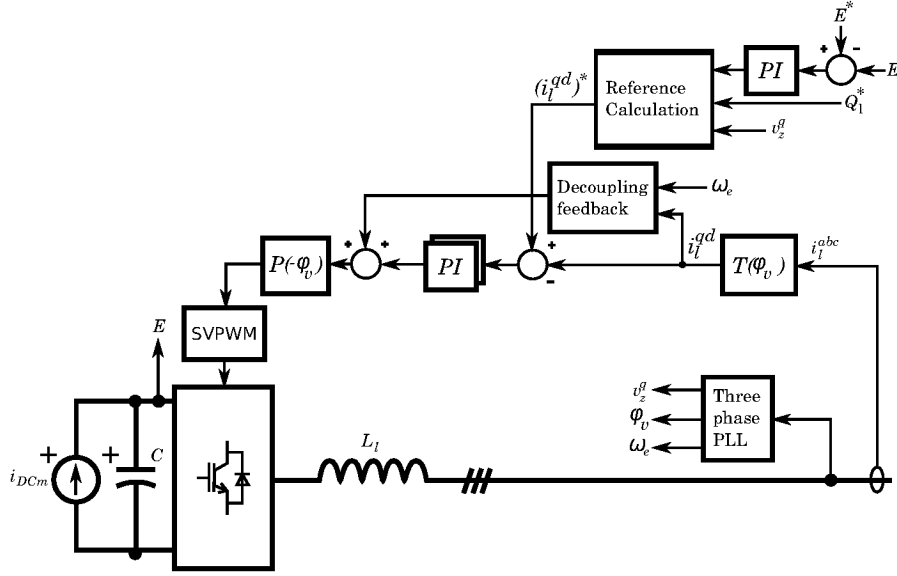


Figure 6.12: Grid-side conventional vector control

wind turbine. The experimental test was done on a ECO74 Wind turbine from Alstom (see Figure 6.13) while operating at partial load. Measurements of the electrical magnitudes on the medium voltage (MV) side of the farm connection transformer of the wind turbine were available to compare with simulation results (see Figure 6.14). Table 6.1 shows the parameters of the operating point before the voltage dip and the nominal values used to compute the per-unit (pu) quantities.

Parameter	Value	Units
Nominal power (stator plus rotor)	1,76	MVA
Nominal MV voltage	17,32	kV (phase to phase rms)
Nominal MV current	33,81	A (rms)
Rotor-side converter rated power	750	kVA
Grid-side converter rated power	480	kVA
Active Power before the voltage dip	0,1532	pu
Reactive Power before the voltage dip	0,0033	pu

Table 6.1: Characteristic parameters of the WTGS used for the voltage sag test.

The simulated voltage sag was a symmetrical drop of the voltage applied

Chapter 6 Conventional DFIG vector control



Figure 6.13: Picture of a real ECO74 WTGS. More detail is available on <http://www.power.alstom.com>.

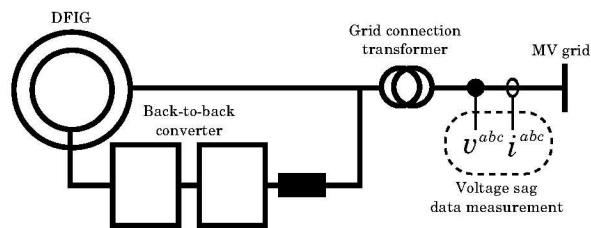


Figure 6.14: Voltage sag test measurements.

6.4 Validation of the simulation model using experimental results

to the medium voltage side of the wind turbine transformer. Table 6.2 shows the parameters of the sag and Figure 6.15 shows the root mean square (rms) graph of the measured MV side voltages from the experimental test which are used as the input to the simulation model.

Parameter	Value	Units
Duration	540	ms
Voltage amplitude during the dip	0,215	pu
Drop start ramp length	15	ms
Drop end ramp length	30	ms

Table 6.2: Voltage dip parameters

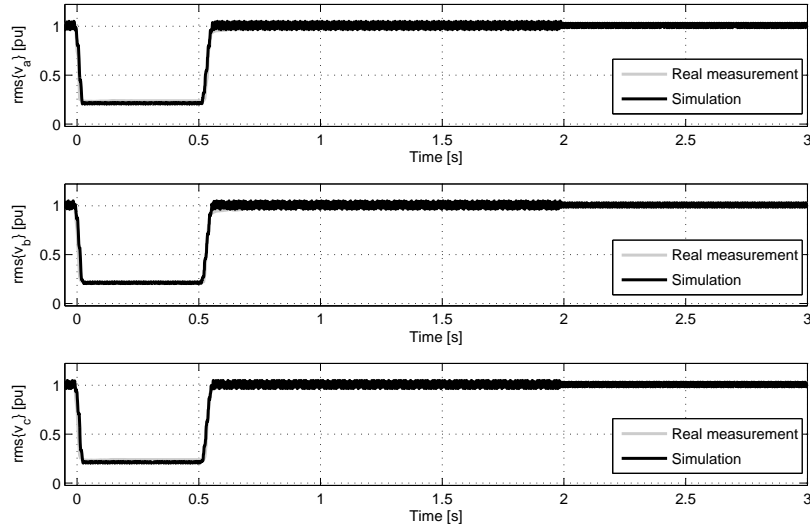


Figure 6.15: Rms value of the *abc* voltages on the MV side of the wind turbine transformer during the voltage sag test.

During a voltage sag, the current needed to inject to the grid to keep the same active power output rises due to the drop in the grid voltage. If the WTGS is working on a operation point close to the limits of the converter, the converter may be unable to output the desired amount of power to the grid, thus producing a power imbalance in the DC bus of the converter which will make the DC bus voltage to rise. Different strategies exist to

Chapter 6 Conventional DFIG vector control

deal with voltage sags doing the so called ride-through and avoiding to have to stop and disconnect the WTGS from the grid. Here, the same strategy implemented on the real WTGS is used in the simulation to ensure the correlation between the simulation and the real test.

The strategy used here is split in two different procedures: the first one is the replacement of the torque and the stator reactive power control current reference signals computed from (6.3) during the sag by two constant values from tabulated data as soon as the voltage sag is detected. The second procedure is the use of the so called crowbar protection which is a resistor that is connected to the machine rotor terminals to absorb part of the current flowing through the machine rotor windings during transients when the DC bus voltages reaches a threshold value of 1.140 V.

According to the quasi-decoupled active and reactive power control, giving a 0 as the i_{rd} reference value during the sag, suppresses the generator’s torque and the active power flowing through the rotor windings thus minimizing the power through the rotor-side converter and the rise of the DC bus voltage. Also, giving a non-zero value as the i_{rq} reference signal allows providing reactive power to the grid which may be a requirement during voltage sags. As the grid voltage reaches its nominal value, the constant current reference signals are replaced again by the ones computed from (6.3). The torque reference is kept constant for a few seconds and then switched back to the output of the speed control torque reference signal.

6.4.1 Controller response

In this section a series of graphs of the evolution of some relevant internal variables of the model are presented which show the proper behavior of the different WTGS control loops. Note that this variables were not measured on the real test thus no comparison with the actual system evolution is shown, proper comparison between simulation and experimental measurements will be presented for the MV variables later.

Figure 6.16 shows the evolution of the rotor current and its reference value. i_{rd} current reference value is kept constant for one second after the rise of the voltage. The rotor voltage applied by the converter can be seen in Figure 6.17. It be seen that the d component does not remain constant despite the constant value of the torque reference due to the linearization state feedback which depends on the mechanical speed. Figure 6.18 shows the stator reactive power and the generator torque and its reference values. Notice that according to the ride-through strategy, the torque reference from the speed control is ignored during the voltage dip. The evolution of the

6.4 Validation of the simulation model using experimental results

angular speed of the generator can be seen in Figure 6.19, it can be seen that the speed of the machine increases during the voltage sag due to the reduction of the generator torque.

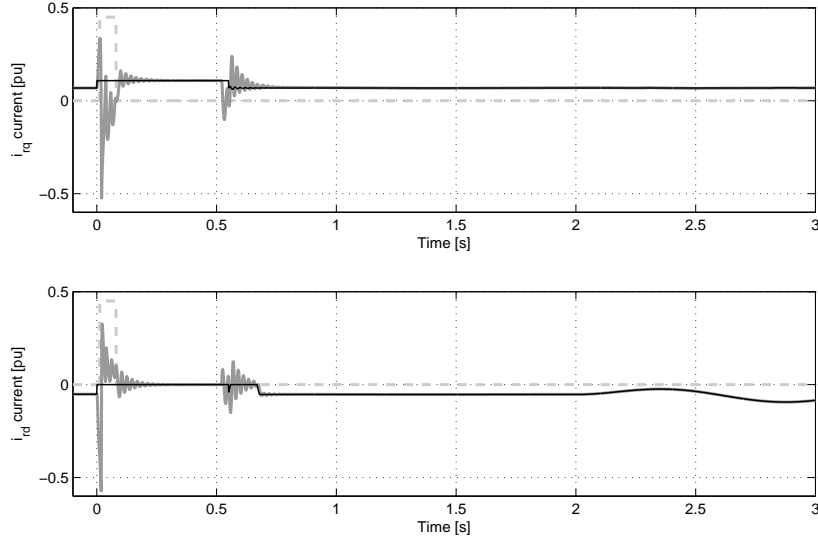


Figure 6.16: DFIG rotor current. The continuous black line corresponds to the reference value, the continuous grey line corresponds to the actual value and the grey dashed line corresponds to the crowbar connection state.

The grid-side converter control DC-bus voltage and reactive power reference inputs are kept constant despite the voltage dip. The currents through the converter and its reference values can be seen in Figure 6.20. The voltages applied by the converter on the AC side can be seen in Figure 6.21. The evolution of the DC bus voltage can be seen in Figure 6.22.

6.4.2 Comparison with experimental results

In this section a comparison between the simulation results and the measurements available from the real test is presented.

Figure 6.23 shows the evolution of the active and reactive power output of the MV transformer on the MV side. The comparison of the evolution of the RMS values of the currents on the MV side of the transformer can also be seen on Figure 6.24.

Chapter 6 Conventional DFIG vector control

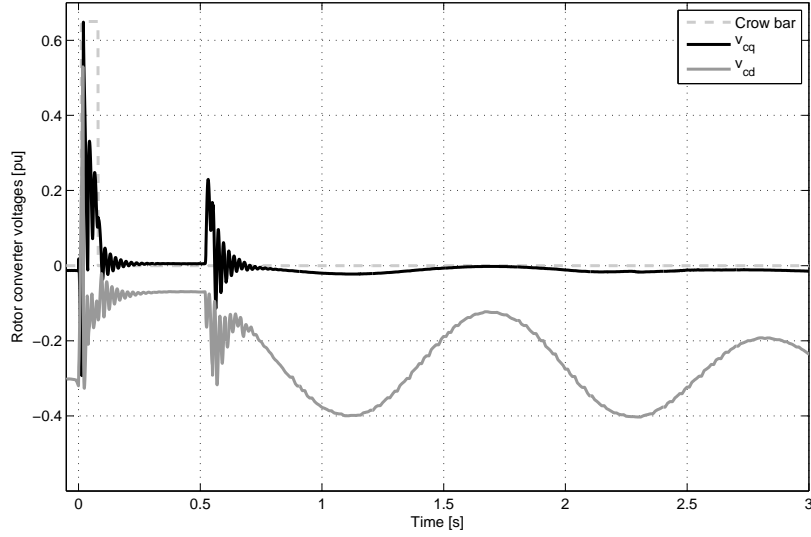


Figure 6.17: Machine-side inverter voltages voltage during the voltage sag.

The comparison shows that the evolution obtained from the simulated model and the measured data are very close despite the reactive power in the real system shows a slightly slower evolution at the end of the sag. As the measurements were made on the MV side of the transformer, the close resemblance of the active power evolution suggests that the neglect of the transformer magnetizing transients may be the cause of these differences. Dynamic models of transformers can be found in the literature which can be adapted from experimental data from transformer tests [30] and could be added to the model to improve its accuracy. Unfortunately, to adapt the model and confirm these hypothesis, measurements from both sides of the transformer which are not available would be necessary.

6.4 Validation of the simulation model using experimental results

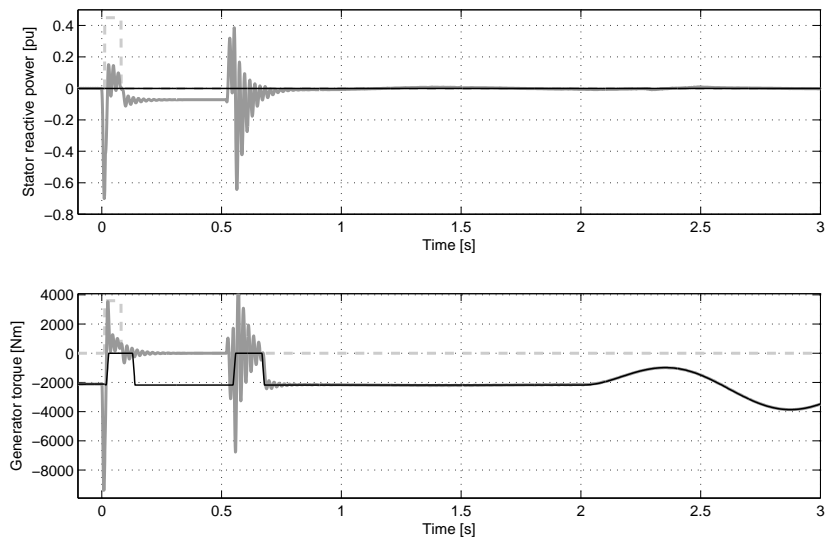


Figure 6.18: Stator reactive power and generator torque during the voltage sag. The continuous grey line corresponds to the output value, the continuous black line corresponds to the reference value and the grey dashed line corresponds to the crowbar connection state.

Chapter 6 Conventional DFIG vector control

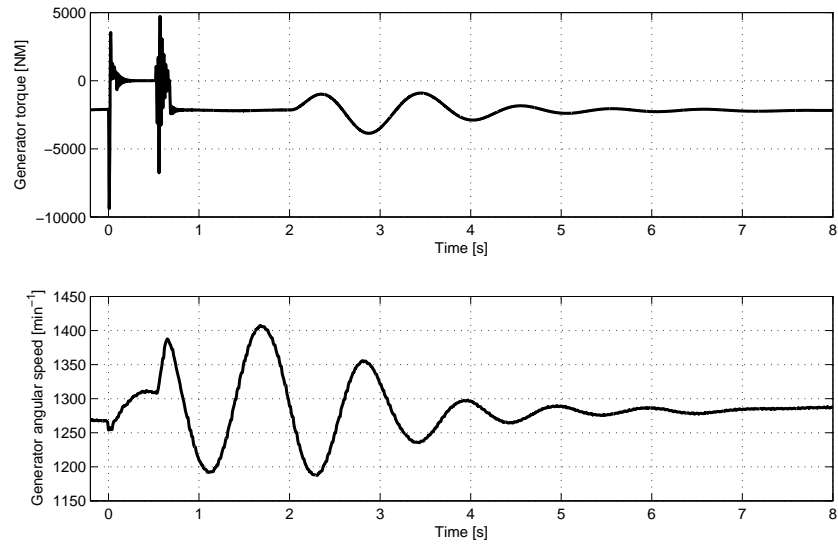


Figure 6.19: Generator torque and angular speed during the voltage sag.

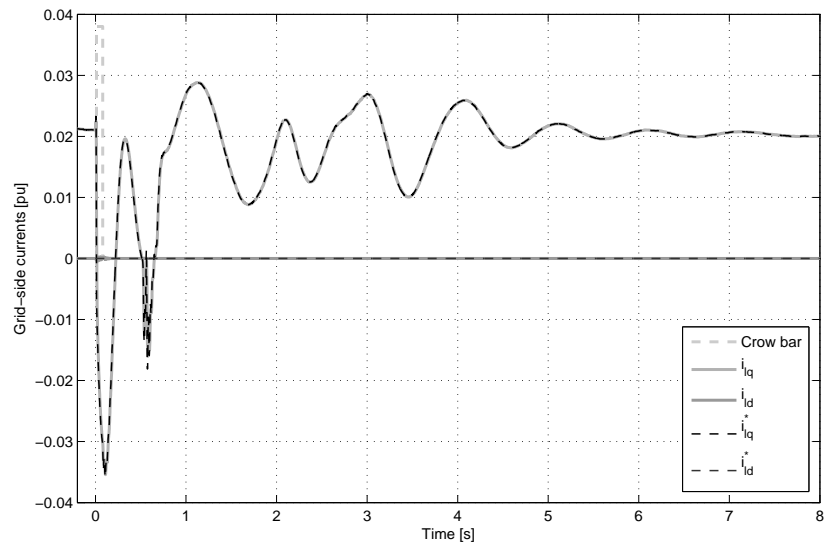


Figure 6.20: Grid-side inverter output current during the voltage sag.

6.4 Validation of the simulation model using experimental results

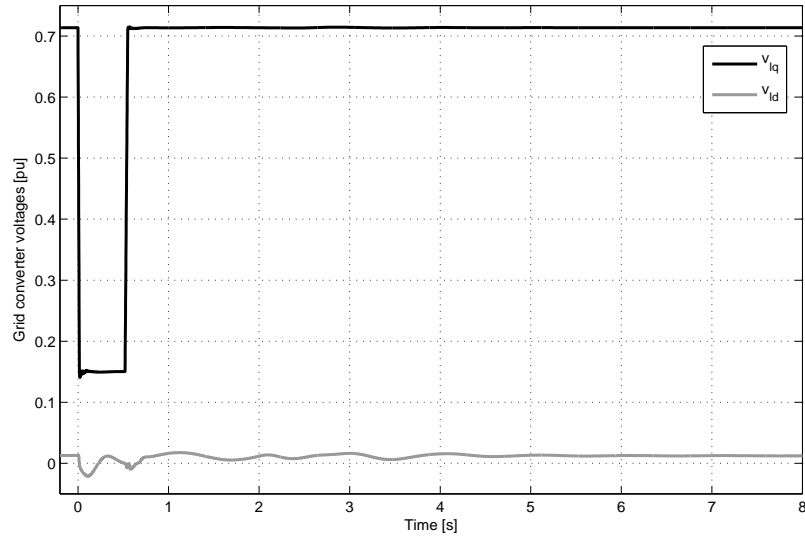


Figure 6.21: Grid-side inverter output voltages during the voltage sag.

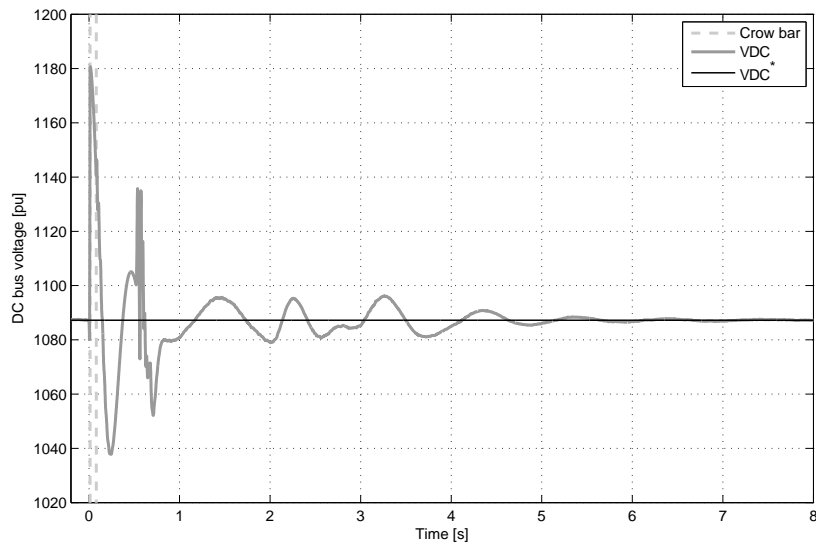


Figure 6.22: DC bus voltage during the voltage sag.

Chapter 6 Conventional DFIG vector control

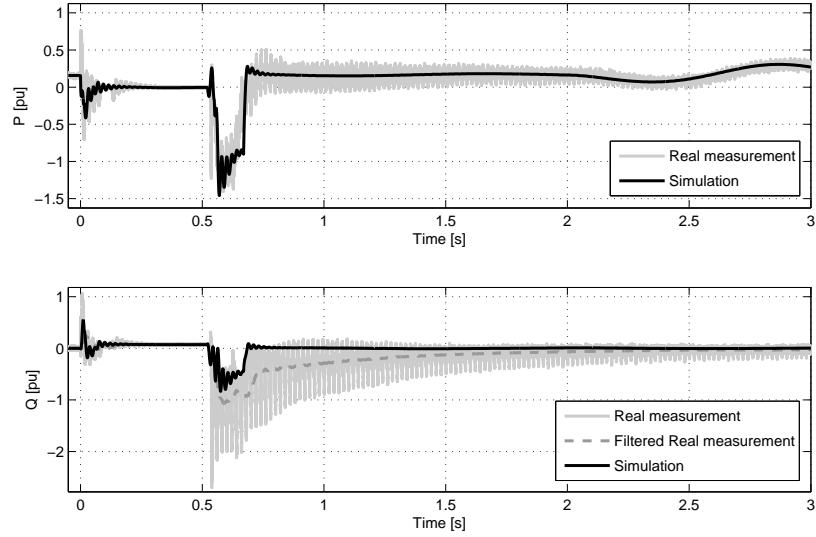


Figure 6.23: Active and reactive power output of the WTGS measured on the MV-side of the transformer

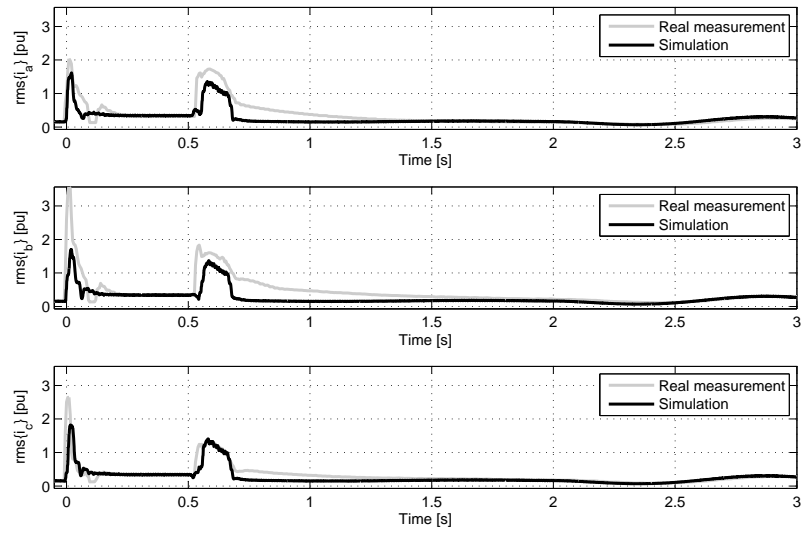


Figure 6.24: RMS value of the abc currents of the MV-side of the transformer

Chapter 7

Dual synchronous reference frame DFIG vector control

7.1 Introduction

This chapter analyzes the use of a dual synchronous vector control design for the control of a DFIG-based WTGS to make the system able to operate under grid voltage unbalances due to unbalanced voltage sags.

As mentioned in the previous chapter, the conventional vector control is meant for the operation under balanced conditions. This restriction is usually not an important issue as in most common vector control applications with squirrel cage induction motors or synchronous permanent magnet motors, the machine is isolated from the grid by the converter. In the case of the DFIG, though, the stator is connected to the grid, thus the voltages seen by the machine can no longer be assumed to be balanced.

The former DFIG wind turbines which used conventional vector control, usually assumed the network unbalances to be small. In such case, when an unbalanced voltage sag occurred, if the negative sequence grid voltage was small compared to the positive sequence, the effect on the performance of the current control would be small and the system would be able to remain connected during the fault. However, if the voltages are very unbalanced, the current control was likely to be unable to properly control the machine and it would be needed to disconnect the machine from the grid.

The dual synchronous reference frame is an extension of the conventional vector control which solves the restriction imposed by the conventional vector control to operate under balanced conditions. To do so, it uses the Fortescue transformation to split the system in two decoupled systems corresponding to the positive and negative sequence, which are both balanced, and controlling them separately by using two independent vector controllers.

The chapter is organized as follows: first the design of a dual synchronous reference frame vector controller for the DFIG is analyzed in Section 7.2.

Chapter 7 Dual synchronous reference frame DFIG vector control

Later, in Section 7.3, the same design principle is used to extend the vector controller of the AC grid side of the converter.

7.2 Machine side control

As it was shown in Section 3.4, considering a general unbalanced condition, the Park transformation is no longer capable of transforming the time varying steady state system magnitudes into constant vectors because of the loss of symmetry between the three phases. However due to the linear nature of the system, the analysis tools for balanced systems can be extended to the unbalanced systems by decomposing the system as a sum of the so called positive, negative and zero sequences. To do so, the so called Fortescue variable complex transformation matrix, introduced in [26], must be applied to the variables. This transformation is defined as¹:

$$\begin{bmatrix} \underline{X}^+ \\ \underline{X}^- \\ \underline{X}^0 \end{bmatrix} \triangleq \frac{1}{3} \begin{bmatrix} 1 & a & a^2 \\ 1 & a^2 & a \\ 1 & 1 & 1 \end{bmatrix} \begin{bmatrix} \underline{X}_a \\ \underline{X}_b \\ \underline{X}_c \end{bmatrix} \quad (7.1)$$

where $a \triangleq e^{j\frac{2\pi}{3}}$ and $\underline{X}_a, \underline{X}_b, \underline{X}_c$ are the phasors associated to the magnitudes of each phase and can be related to the abc time signal as:

$$\begin{aligned} x^{abc}(t) &= \begin{bmatrix} \sqrt{2}X_a \cos(\omega_e t + \varphi_{xa}) \\ \sqrt{2}X_b \cos(\omega_e t + \varphi_{xb}) \\ \sqrt{2}X_c \cos(\omega_e t + \varphi_{xc}) \end{bmatrix} = \begin{bmatrix} \Re \{ \sqrt{2}X_a e^{-j\omega_e t} e^{-j\varphi_{xa}} \} \\ \Re \{ \sqrt{2}X_b e^{-j\omega_e t} e^{-j\varphi_{xb}} \} \\ \Re \{ \sqrt{2}X_c e^{-j\omega_e t} e^{-j\varphi_{xc}} \} \end{bmatrix} \\ &= \begin{bmatrix} \Re \{ \sqrt{2}\underline{X}_a e^{-j\omega_e t} \} \\ \Re \{ \sqrt{2}\underline{X}_b e^{-j\omega_e t} \} \\ \Re \{ \sqrt{2}\underline{X}_c e^{-j\omega_e t} \} \end{bmatrix} \quad (7.2) \end{aligned}$$

and thus

$$\begin{cases} \underline{X}_a e^{-j\omega_e t} = X_a (\cos(\varphi_{xa}) + j \sin(\varphi_{xa})) e^{-j\omega_e t} \\ \underline{X}_b e^{-j\omega_e t} = X_b (\cos(\varphi_{xb}) + j \sin(\varphi_{xb})) e^{-j\omega_e t} \\ \underline{X}_c e^{-j\omega_e t} = X_c (\cos(\varphi_{xc}) + j \sin(\varphi_{xc})) e^{-j\omega_e t} \end{cases} \quad (7.3)$$

Note that these signals are complex and only the real part correspond to a physical magnitude which can be measured in the real system. However,

¹Note that to be consistent with the definition of the positive and negative sequence phasors introduced in (3.58) and (3.59), \underline{X}^- appears in (7.1) as a complex conjugate.

7.2 Machine side control

the signal is a so called analytical signal as the imaginary part is equal to the real part with a phase shift of 90 degrees. Thus, the imaginary part can be obtained from the real part by using a Hilbert transform filter, which is a filter with a unit gain and a phase of 90 degrees for all the frequencies of the spectrum:

$$\begin{cases} \underline{X}_a e^{-j\omega_e t} = \frac{1}{\sqrt{2}} (x_a(t) - j(H(t) * x_a(t))) \\ \underline{X}_b e^{-j\omega_e t} = \frac{1}{\sqrt{2}} (x_b(t) - j(H(t) * x_b(t))) \\ \underline{X}_c e^{-j\omega_e t} = \frac{1}{\sqrt{2}} (x_c(t) - j(H(t) * x_c(t))) \end{cases} \quad (7.4)$$

where $H(t)$ is the impulse response of the Hilbert transform filter and $*$ is the convolution operator.

This suggests that the Fortescue transformation can be used in conjunction with a series of Hilbert transform filters to decompose the measured signal into positive and negative sequence and apply a synchronous reference frame controller to control the variables of each sequence.

Considering the case of a three wire system where the 0 sequence can be eliminated from the equations, (7.1) can also be combined with the Clarke transformation matrix $T(0)$ to put the variables as a function of the $\alpha\beta$ components suppressing the 0 sequence:

$$\begin{aligned} \begin{bmatrix} \underline{X}^+ e^{-j\omega_e t} \\ \underline{X}^- e^{-j\omega_e t} \end{bmatrix} &= \frac{1}{3} \begin{bmatrix} 1 & a & a^2 \\ 1 & a^2 & a \end{bmatrix} T^{-1}(0) \begin{bmatrix} \underline{X}_\alpha e^{-j\omega_e t} \\ \underline{X}_\beta e^{-j\omega_e t} \end{bmatrix} \\ &= \frac{1}{3} \begin{bmatrix} 1 & a & a^2 \\ 1 & a^2 & a \end{bmatrix} T^{-1}(0) \begin{bmatrix} 1 & -j & 0 & 0 \\ 0 & 0 & 1 & -j \end{bmatrix} \begin{bmatrix} x_\alpha(t) \\ H(t) * x_\alpha(t) \\ x_\beta(t) \\ H(t) * x_\beta(t) \end{bmatrix} \end{aligned} \quad (7.5)$$

Then, the $\alpha\beta$ components of the positive and negative sequence can be obtained as:

$$\begin{cases} x_\alpha^+(t) = \Re \{ \underline{X}^+ e^{-j\omega_e t} \} \\ x_\beta^+(t) = -\Im \{ \underline{X}^+ e^{-j\omega_e t} \} \\ x_\alpha^-(t) = \Re \{ \underline{X}^- e^{j\omega_e t} \} \\ x_\beta^-(t) = \Im \{ \underline{X}^- e^{j\omega_e t} \} \end{cases} \quad (7.6)$$

Finally, as the former transformations are linear, an equivalent multivariable transformation filter transfer function can be obtained by combining its equations:

Chapter 7 Dual synchronous reference frame DFIG vector control

$$\begin{bmatrix} x^{\alpha\beta+}(s) \\ x^{\alpha\beta-}(s) \end{bmatrix} = \frac{1}{2} \underbrace{\begin{bmatrix} 1 & -H(s) \\ H(s) & 1 \\ 1 & H(s) \\ -H(s) & 1 \end{bmatrix}}_{J(s)} x^{\alpha\beta}(s) \quad (7.7)$$

Note that, as the number of degrees of freedom remains two, there exist the following equivalences:

$$\begin{cases} x_{\beta}^{+}(s) = H(s)x_{\alpha}^{+}(s) \\ x_{\beta}^{-}(s) = -H(s)x_{\alpha}^{-}(s) \end{cases} \quad (7.8)$$

As $J(s)$ is not square, it is not possible to invert it. However, a 1-inverse matrix can be found for it. As $J(s)$ is full column rank, its Moore-Penrose pseudoinverse $J(s)^{\dagger}$ can be found as:

$$J(s)^{\dagger} = (J(s)^T J(s))^{-1} \quad (7.9)$$

This matrix is the so called left inverse of $J(s)$, thus:

$$J(s)^{\dagger} J(s) = I_4 \quad (7.10)$$

where I_4 is a 4x4 identity matrix.

Taking the DFIG machine equations in (3.21) for $\theta \equiv 0$, the following equations are obtained:

$$\begin{aligned} \begin{bmatrix} v_s^{\alpha\beta} \\ v_r^{\alpha\beta} \end{bmatrix} &= \begin{bmatrix} L_s & 0 & M & 0 \\ 0 & L_s & 0 & M \\ M & 0 & L_r & 0 \\ 0 & M & 0 & L_r \end{bmatrix} \frac{d}{dt} \begin{bmatrix} i_s^{\alpha\beta} \\ i_r^{\alpha\beta} \end{bmatrix} \\ &+ \begin{bmatrix} r_s & 0 & 0 & 0 \\ 0 & r_s & 0 & 0 \\ 0 & -\omega_r M & r_r & -\omega_r L_r \\ \omega_r M & 0 & \omega_r L_r & r_r \end{bmatrix} \begin{bmatrix} i_s^{\alpha\beta} \\ i_r^{\alpha\beta} \end{bmatrix} \quad (7.11) \end{aligned}$$

Transforming this equation by Laplace, we obtain:

$$\begin{bmatrix} v_s^{\alpha\beta}(s) \\ v_r^{\alpha\beta}(s) \end{bmatrix} = \begin{bmatrix} L_s s + r_s & 0 & M s & 0 \\ 0 & L_s s + r_s & 0 & M s \\ M s & -\omega_r M & L_r s + r_r & -\omega_r L_r \\ \omega_r M & M s & \omega_r L_r & L_r s + r_r \end{bmatrix} \begin{bmatrix} i_s^{\alpha\beta}(s) \\ i_r^{\alpha\beta}(s) \end{bmatrix} \quad (7.12)$$

7.2 Machine side control

The variable transformation is then introduced to the stator and rotor variables using the following 8x4 variable change matrix:

$$N(s) \triangleq \begin{bmatrix} J(s) & 0_{4,2} \\ 0_{4,2} & J(s) \end{bmatrix} \quad (7.13)$$

which has the following 4x8 pseudoinverse:

$$N(s)^\dagger = \begin{bmatrix} J^\dagger(s) & 0_{2,4} \\ 0_{2,4} & J^\dagger(s) \end{bmatrix} \quad (7.14)$$

Multiplying (7.12), we obtain:

$$N(s) \begin{bmatrix} v_s^{\alpha\beta}(s) \\ v_r^{\alpha\beta}(s) \end{bmatrix} = N(s) \begin{bmatrix} L_s s + r_s & 0 & M s & 0 \\ 0 & L_s s + r_s & 0 & M s \\ M s & -\omega_r M & L_r s + r_r & -\omega_r L_r \\ \omega_r M & M s & \omega_r L_r & L_r s + r_r \end{bmatrix} N(s)^\dagger \cdot N(s) \begin{bmatrix} i_s^{\alpha\beta}(s) \\ i_r^{\alpha\beta}(s) \end{bmatrix} \quad (7.15)$$

Replacing the machine magnitudes by their transformations the following is then transformed into:

$$\begin{bmatrix} v_s^{\alpha\beta+}(s) \\ v_s^{\alpha\beta-}(s) \\ v_r^{\alpha\beta+}(s) \\ v_r^{\alpha\beta-}(s) \end{bmatrix} = N(s) \begin{bmatrix} L_s s + r_s & 0 & M s & 0 \\ 0 & L_s s + r_s & 0 & M s \\ M s & -\omega_r M & L_r s + r_r & -\omega_r L_r \\ \omega_r M & M s & \omega_r L_r & L_r s + r_r \end{bmatrix} N(s)^\dagger \cdot \begin{bmatrix} i_s^{\alpha\beta+}(s) \\ i_s^{\alpha\beta-}(s) \\ i_r^{\alpha\beta+}(s) \\ i_r^{\alpha\beta-}(s) \end{bmatrix} \quad (7.16)$$

Substituting $N(s)$ and $N^\dagger(s)$ in this equation and applying the equivalences shown in (7.8), the following equations are obtained:

Chapter 7 Dual synchronous reference frame DFIG vector control

$$\begin{bmatrix} v_s^{\alpha\beta+}(s) \\ v_s^{\alpha\beta-}(s) \\ v_r^{\alpha\beta+}(s) \\ v_r^{\alpha\beta-}(s) \end{bmatrix} = \begin{bmatrix} L_s s + r_s & 0 & 0 & 0 & 0 & 0 & 0 & 0 \\ 0 & L_s s + r_s & 0 & 0 & 0 & 0 & 0 & 0 \\ 0 & 0 & L_s s + r_s & 0 & 0 & 0 & 0 & 0 \\ sM & -\omega_r M & 0 & L_r s + r_r & -\omega_r L_r & 0 & 0 & 0 \\ \omega_r M & sM & 0 & \omega_r L_r & L_r s + r_r & 0 & 0 & 0 \\ 0 & 0 & sM & -\omega_r M & 0 & L_r s + r_r & -\omega_r L_r & 0 \\ 0 & 0 & \omega_r M & sM & 0 & \omega_r L_r & L_r s + r_r & 0 \end{bmatrix} \begin{bmatrix} i_s^{\alpha\beta+}(s) \\ i_s^{\alpha\beta-}(s) \\ i_r^{\alpha\beta+}(s) \\ i_r^{\alpha\beta-}(s) \end{bmatrix} \quad (7.17)$$

note that this system of equations has rank eight whereas the rank of the previous was four. The reason for that is that these equations are true if and only if the constraints in (7.8) are met.

The former equation can be split in two separate equations, one for each sequence:

$$\begin{bmatrix} v_s^{\alpha\beta+} \\ v_r^{\alpha\beta+} \end{bmatrix} = \begin{bmatrix} L_s & 0 & M & 0 \\ 0 & L_s & 0 & M \\ M & 0 & L_r & 0 \\ 0 & M & 0 & L_r \end{bmatrix} \frac{d}{dt} \begin{bmatrix} i_s^{\alpha\beta+} \\ i_r^{\alpha\beta+} \end{bmatrix} + \begin{bmatrix} r_s & 0 & 0 & 0 \\ 0 & r_s & 0 & 0 \\ 0 & -\omega_r M & r_r & -\omega_r L_r \\ \omega_r M & 0 & \omega_r L_r & r_r \end{bmatrix} \begin{bmatrix} i_s^{\alpha\beta+} \\ i_r^{\alpha\beta+} \end{bmatrix} \quad (7.18)$$

$$\begin{bmatrix} v_s^{\alpha\beta-} \\ v_r^{\alpha\beta-} \end{bmatrix} = \begin{bmatrix} L_s & 0 & M & 0 \\ 0 & L_s & 0 & M \\ M & 0 & L_r & 0 \\ 0 & M & 0 & L_r \end{bmatrix} \frac{d}{dt} \begin{bmatrix} i_s^{\alpha\beta-} \\ i_r^{\alpha\beta-} \end{bmatrix} + \begin{bmatrix} r_s & 0 & 0 & 0 \\ 0 & r_s & 0 & 0 \\ 0 & -\omega_r M & r_r & -\omega_r L_r \\ \omega_r M & 0 & \omega_r L_r & r_r \end{bmatrix} \begin{bmatrix} i_s^{\alpha\beta-} \\ i_r^{\alpha\beta-} \end{bmatrix} \quad (7.19)$$

7.2 Machine side control

The split positive and negative sequence vectors can then be transformed to a synchronous reference frame by using a rotation matrix $R(\theta)$ as:

$$\begin{cases} x^{qd+} = R(\omega_e t + \varphi^+) x^{\alpha\beta+} \\ x^{qd-} = R(-\omega_e t - \varphi^-) x^{\alpha\beta-} \end{cases} \quad (7.20)$$

The equation for the positive sequence becomes:

$$\begin{aligned} \begin{bmatrix} v_s^{qd+} \\ v_r^{qd+} \end{bmatrix} &= \begin{bmatrix} L_s & 0 & M & 0 \\ 0 & L_s & 0 & M \\ M & 0 & L_r & 0 \\ 0 & M & 0 & L_r \end{bmatrix} \frac{d}{dt} \begin{bmatrix} i_s^{qd+} \\ i_r^{qd+} \end{bmatrix} \\ &+ \begin{bmatrix} r_s & L_s \omega_e & 0 & M \omega_e \\ -L_s \omega_e & r_s & -M \omega_e & 0 \\ 0 & M(\omega_e - \omega_r) & r_r & L_r(\omega_e - \omega_r) \\ -M(\omega_e - \omega_r) & 0 & -L_r(\omega_e - \omega_r) & r_r \end{bmatrix} \begin{bmatrix} i_s^{qd+} \\ i_r^{qd+} \end{bmatrix} \end{aligned} \quad (7.21)$$

while the negative sequence equation becomes:

$$\begin{aligned} \begin{bmatrix} v_s^{qd-} \\ v_r^{qd-} \end{bmatrix} &= \begin{bmatrix} L_s & 0 & M & 0 \\ 0 & L_s & 0 & M \\ M & 0 & L_r & 0 \\ 0 & M & 0 & L_r \end{bmatrix} \frac{d}{dt} \begin{bmatrix} i_s^{qd-} \\ i_r^{qd-} \end{bmatrix} \\ &+ \begin{bmatrix} r_s & -L_s \omega_e & 0 & -M \omega_e \\ L_s \omega_e & r_s & M \omega_e & 0 \\ 0 & -M(\omega_e + \omega_r) & r_r & -L_r(\omega_e + \omega_r) \\ M(\omega_e + \omega_r) & 0 & L_r(\omega_e + \omega_r) & r_r \end{bmatrix} \begin{bmatrix} i_s^{qd-} \\ i_r^{qd-} \end{bmatrix} \end{aligned} \quad (7.22)$$

The structure of the current controller for each sequence is based on the same principle as in the conventional vector control. It combines a decoupling feedback loop which also eliminates the dependency of the dynamics on the machine speed and a feedback controller fed with the error between the measured current and the reference value. The equation for the positive sequence voltage applied to control the positive sequence current is:

$$\begin{bmatrix} v_{rq+} \\ v_{rd+} \end{bmatrix} = \begin{bmatrix} \hat{v}_{rq+} + (\omega_e - \omega_r) M i_{sd+} + (\omega_e - \omega_r) L_r i_{rd+} \\ \hat{v}_{rd+} - (\omega_e - \omega_r) M i_{sq+} - (\omega_e - \omega_r) L_r i_{rd+} \end{bmatrix} \quad (7.23)$$

Chapter 7 Dual synchronous reference frame DFIG vector control

where \hat{v}_{rq+} and \hat{v}_{rd+} are the outputs for the $q+$ and $d+$ positive sequence current controllers. Also, for the negative sequence the voltage equation is:

$$\begin{bmatrix} v_{rq-} \\ v_{rd-} \end{bmatrix} = \begin{bmatrix} \hat{v}_{rq-} - (\omega_e + \omega_r) M i_{sd-} - (\omega_e + \omega_r) L_r i_{rd-} \\ \hat{v}_{rd-} + (\omega_e + \omega_r) M i_{sq-} + (\omega_e + \omega_r) L_r i_{rd-} \end{bmatrix} \quad (7.24)$$

where \hat{v}_{rq-} and \hat{v}_{rd-} are the outputs for the $q-$ and $d-$ positive sequence current controllers.

To test the performance of the decoupling loops, a simulation of the response to a step change of 50 V in the \hat{v}_{rq+} control action is applied for two different machine speeds (1.000 and 1.900 min^{-1}) the same way it was done for the conventional vector control in the previous chapter (see Figure 6.1). Figure 7.1 shows the evolution of the applied rotor voltage, which contains the controller output \hat{v}_r plus the decoupling terms for both the positive and negative sequence synchronous reference frames. Notice that although the negative sequence voltage is not zero, it is smaller than the positive sequence voltage, thus proving the proper decoupling between both sequences. This is further confirmed by the evolution of the rotor current which is shown in Figure 7.2.

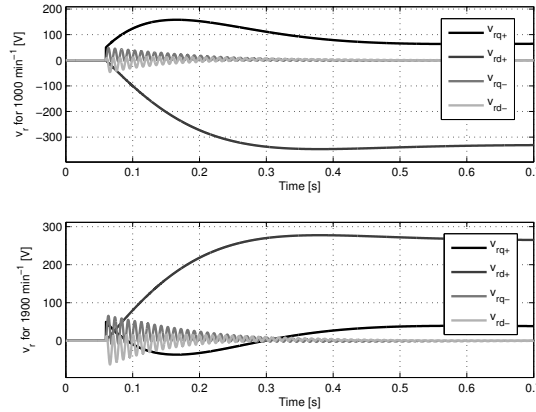


Figure 7.1: Rotor voltage applied to test the decoupling feedback loop used by the double synchronous reference frame vector controller of the DFIG

From the evolution of the current (Figure 7.2), it can also be seen that the dependence on the rotor speed is suppressed. On the other hand, comparing the evolution of the current to that obtained for the same test with the

7.2 Machine side control

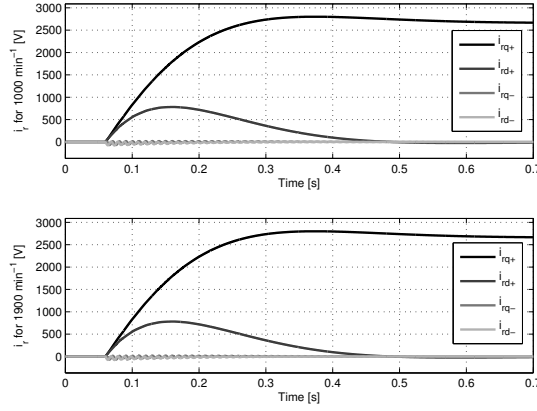


Figure 7.2: Evolution of the rotor current for the test of the decoupling feedback loop used by the double synchronous reference frame vector controller of the DFIG

conventional vector control (Figure 6.3), it can be seen that the decoupling between q and d is bad during the transients although it works well in steady state. This is due to the use of Hilbert transform filters with a limited bandwidth which only provide the proper phase delay for frequencies close to the nominal grid frequency as will be explained later. This suggests that the performance obtained from this system will be worse than that of the original conventional vector control for a balanced operating point.

As in the conventional vector controller, a PI controller can be used in the current control loop and its parameters can be tuned the same way as in the conventional vector control case using (6.11).

The output voltage of the controller to be applied on the machine, which is usually fed to a PWM scheme to generate the switching signal for the semi-conductors, is obtained by transforming the positive and negative sequence voltages to a common reference frame. This is accomplished by inverting the rotation matrices as:

$$x^{\alpha\beta} = R(-\omega_e t - \varphi^+)x^{qd+} + R(\omega_e t + \varphi^-)x^{qd-} \quad (7.25)$$

In order to test the performance of the controller, a simulation of the response of the current control is performed for a constant grid voltage equal to the nominal voltage and a step from 0 to the nominal torque for the same two operating points tested for the conventional vector control (1.000 and

Chapter 7 Dual synchronous reference frame DFIG vector control

1.900 min⁻¹). The evolution of the current is shown in Figure 7.3, notice that the response is similar to that of the conventional vector controller (Figure 6.4) although the effect on the d component of the current is greater as the performance of the decoupling loop is worse. Figure 7.4 shows the response of torque of the machine, notice that although there exists a small ripple in the torque, it reaches the final value in almost the same time as the rotor current.

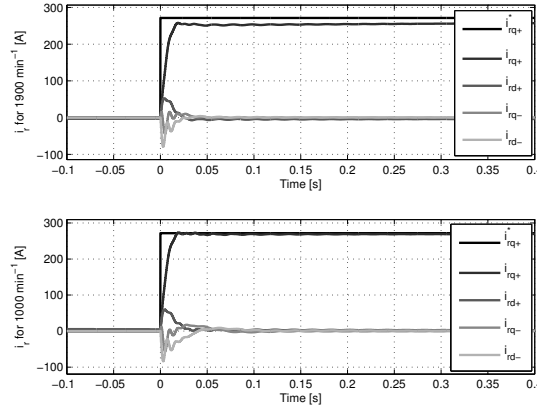


Figure 7.3: Evolution of the rotor current of the DFIG to a step reference change when using dual vector control

Finally, the design of the Hilbert transform filter $H(s)$ must be discussed. Several options exist, here a first order allpass filter is used. This filter has the following transfer function:

$$H(s) = \frac{s - \omega_e}{s + \omega_e} \quad (7.26)$$

Although the ideal Hilbert transformation filter should have a unitary gain and a phase delay of -90° for all the frequencies, the first order all-pass filter has a phase delay that goes from -180° at the DC frequency to 0° at infinite frequency and it only has the correct delay of -90° for a frequency of 50 Hz. Thus, in steady state the electrical magnitudes may be properly transformed using this filter if the frequency of the grid magnitudes is exactly the same as the frequency for which the filter is designed. However, if the distortion caused on the signals by a wrong delay of the filter may cause the overall performance of the system to be worse in comparison to the performance obtained under balanced conditions using a conventional vector

7.2 Machine side control

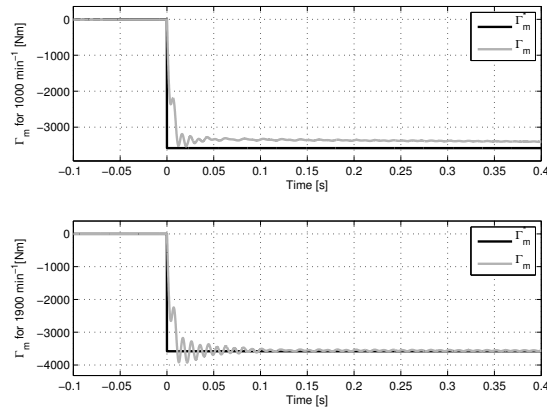


Figure 7.4: Evolution of the DFIG torque to a step reference change when using dual vector control

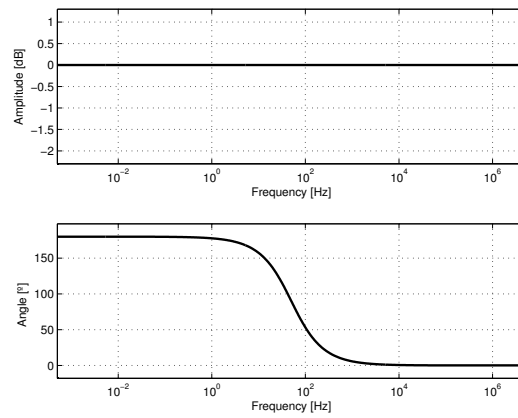


Figure 7.5: Bode plot of the first order allpass Hilbert transformation filter.

Chapter 7 Dual synchronous reference frame DFIG vector control

control scheme. This may force to reduce the performance specifications for the current controllers as the current measure used to calculate the error fed to the controller may have a small bandwidth around the grid nominal frequency.

7.3 Grid-side current control

7.3.1 AC side current control

According to Chapter 5, the equations that describe the AC side current dynamics of the converter (5.17), can be written for the stationary reference frame with $\theta \equiv 0$ as:

$$v_l^{\alpha\beta} = \begin{bmatrix} r_l & 0 \\ 0 & r_l \end{bmatrix} i_l^{\alpha\beta} + L_l \frac{d}{dt} i_l^{\alpha\beta} + v_z^{\alpha\beta} \quad (7.27)$$

By applying the Laplace transformation to these equations, the following is obtained:

$$v_l^{\alpha\beta}(s) = \begin{bmatrix} L_l s + r_l & 0 \\ 0 & L_l s + r_l \end{bmatrix} i_l^{\alpha\beta}(s) + v_z^{\alpha\beta}(s) \quad (7.28)$$

Then, as in the previous section, the equation is multiplied by $J(s)$ to obtain the equations for the positive and negative sequence:

$$J(s)v_l^{\alpha\beta}(s) = J(s) \begin{bmatrix} L_l s + r_l & 0 \\ 0 & L_l s + r_l \end{bmatrix} J(s)^\dagger J(s) i_l^{\alpha\beta}(s) + J(s)v_z^{\alpha\beta}(s) \quad (7.29)$$

This can be easily proven to be equivalent to the following if and only if the constraints in (7.8) are met:

$$\begin{bmatrix} v_l^{\alpha\beta+} \\ v_l^{\alpha\beta-} \end{bmatrix} = \begin{bmatrix} L_l s + r_l & 0 & 0 & 0 \\ 0 & L_l s + r_l & 0 & 0 \\ 0 & 0 & L_l s + r_l & 0 \\ 0 & 0 & 0 & L_l s + r_l \end{bmatrix} \begin{bmatrix} i_l^{\alpha\beta+} \\ i_l^{\alpha\beta-} \end{bmatrix} + \begin{bmatrix} v_z^{\alpha\beta+} \\ v_z^{\alpha\beta-} \end{bmatrix} \quad (7.30)$$

These equations are decoupled between the positive and the negative sequence, thus they can be controlled separately. the equations for each sequence can be obtained by splitting the previous equations as two different systems as:

7.3 Grid-side current control

$$v_l^{\alpha\beta+}(s) = \begin{bmatrix} L_l s + r_l & 0 \\ 0 & L_l s + r_l \end{bmatrix} i_l^{\alpha\beta+}(s) + v_z^{\alpha\beta+}(s) \quad (7.31)$$

$$v_l^{\alpha\beta-}(s) = \begin{bmatrix} L_l s + r_l & 0 \\ 0 & L_l s + r_l \end{bmatrix} i_l^{\alpha\beta-}(s) + v_z^{\alpha\beta-}(s) \quad (7.32)$$

By applying the inverse Laplace transform to these equations, the corresponding differential equations are obtained:

$$v_l^{\alpha\beta+} = \begin{bmatrix} r_l & 0 \\ 0 & r_l \end{bmatrix} i_l^{\alpha\beta+} + L_l \frac{d}{dt} i_l^{\alpha\beta+} + v_z^{\alpha\beta+} \quad (7.33)$$

$$v_l^{\alpha\beta-} = \begin{bmatrix} r_l & 0 \\ 0 & r_l \end{bmatrix} i_l^{\alpha\beta-} + L_l \frac{d}{dt} i_l^{\alpha\beta-} + v_z^{\alpha\beta-} \quad (7.34)$$

As in the previous section, the equations for the positive and negative sequence can be transformed using a conventional rotation to synchronous reference frame by defining the new transformed variables as:

$$\begin{cases} x^{qd+} = R(\omega_e t + \varphi^+) x^{\alpha\beta+} \\ x^{qd-} = R(-\omega_e t - \varphi^-) x^{\alpha\beta-} \end{cases} \quad (7.35)$$

By applying this transformation to the split stationary frame equations the following is obtained:

$$v_l^{qd+} = \begin{bmatrix} r_l & \omega_e L_l \\ -\omega_e L_l & r_l \end{bmatrix} i_l^{qd+} + L_l \frac{d}{dt} i_l^{qd+} + v_z^{qd+} \quad (7.36)$$

and

$$v_l^{qd-} = \begin{bmatrix} r_l & -\omega_e L_l \\ \omega_e L_l & r_l \end{bmatrix} i_l^{qd-} + L_l \frac{d}{dt} i_l^{qd-} + v_z^{qd-} \quad (7.37)$$

As these equations are coupled between q and d and depend on the grid frequency and the grid voltage, as in the conventional vector control, a decoupling feedback loop plus a feed-forward is added by defining the voltage applied by the converter as:

$$v_l^{qd+} = \begin{bmatrix} \hat{v}_{lq+} + \omega_e L_l \dot{i}_{ld+} + v_{zq+} \\ \hat{v}_{ld+} - \omega_e L_l \dot{i}_{lq+} \end{bmatrix} \quad (7.38)$$

whilst for the negative sequence:

Chapter 7 Dual synchronous reference frame DFIG vector control

$$v_l^{qd-} = \begin{bmatrix} \hat{v}_{lq-} - \omega_e L_l i_{ld-} + v_{zq-} \\ \hat{v}_{ld-} + \omega_e L_l i_{lq-} \end{bmatrix} \quad (7.39)$$

To test the proper operation of the decoupling loop, the step response of the system is simulated. In this simulation, a step of 50 V is applied on the control action for the q component of the positive sequence current \hat{v}_{lq}^+ while keeping the control action for the other loops equal to zero. The evolution of the voltage vector applied by the decoupling loop plus the control action is shown in Figure 7.6 and the response of the current is shown in Figure 7.7. From the evolution of the current, it can be seen that although the step is applied to the q component of the positive sequence, neither the decoupling between both sequences nor the decoupling between the q and d components are perfect. Also, comparing this simulation to the one performed to test the decoupling loop of the conventional vector control of the grid side converter (Figure 6.8), the decoupling between q and d is worse. Thus, the performance that can be obtained from this system can be expected to be worse than that of the conventional vector control for balanced operation.

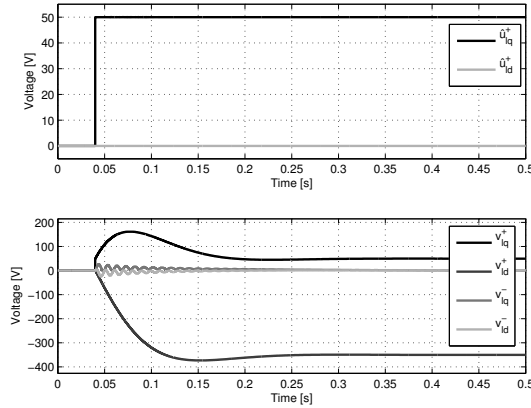


Figure 7.6: Simulated voltage step to test the decoupling feedback loop used by the dual synchronous reference frame vector controller of the AC side current control. *Upper graph*: evolution of \hat{v}_l^{qd} . *Lower graph*: evolution of v_l^{qd} including the voltage applied by the decoupling feedback loop.

Then, assuming the compensation to be perfect, the equations of the decoupled system become:

7.3 Grid-side current control

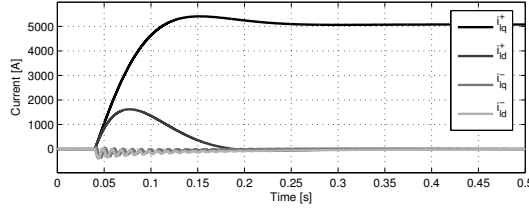


Figure 7.7: Evolution of the AC side current for the test of the decoupling feedback loop used by the dual synchronous reference frame vector controller of the AC side current control.

$$\hat{v}_l^{qd+} = \begin{bmatrix} r_l & 0 \\ 0 & r_l \end{bmatrix} i_l^{qd+} + L_l \frac{d}{dt} i_l^{qd+} \quad (7.40)$$

and

$$\hat{v}_l^{qd-} = \begin{bmatrix} r_l & 0 \\ 0 & r_l \end{bmatrix} i_l^{qd-} + L_l \frac{d}{dt} i_l^{qd-} \quad (7.41)$$

where \hat{v}_l^{qd+} and \hat{v}_l^{qd-} are the control action output of the current feedback controllers for the positive and negative sequences.

A pair of PI current controller can then be used to control the current for each component of each sequence. The parameters for these controllers can be adjusted following the same procedure developed for the conventional vector control from (6.24).

To test the performance of this controllers, a simulation of the response to a reference step change is performed. In this simulation, a step in the q component of the positive sequence current is performed while keeping the other components zero. Figure 7.8 shows the evolution of the current compared to the reference value. Note that the performance can be considered as acceptable although it is worse than that obtained from the conventional vector control for the same situation (Figure 6.9). However, by plotting the evolution of the current in the natural abc variables, Figure 7.9, it can be seen that the evolution doesn't differ a lot from that obtained from the conventional controller, Figure 6.10. Finally, the evolution of the applied voltage by the qd components of both positive and negative sequences is shown in Figure 6.11. Note that the evolution of the control action does not exceed the acceptable limits of the applied voltage and the negative sequence voltage is 60 times smaller than that of the positive sequence during

Chapter 7 Dual synchronous reference frame DFIG vector control

the transient, thus confirming that the decoupling between both sequences is good.

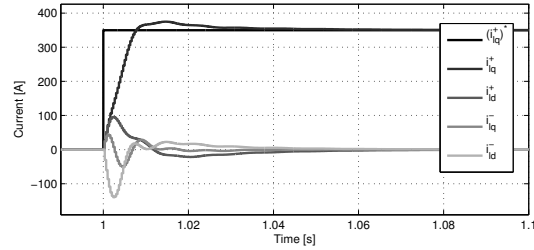


Figure 7.8: Evolution of the AC side current of the grid side inverter in the qd reference frame to a step reference change when using dual synchronous reference frame vector control

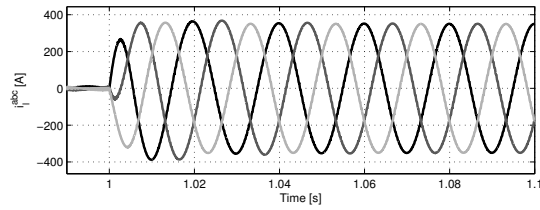


Figure 7.9: Evolution of the AC side current of the grid side inverter in the abc reference frame to a step reference change when using dual synchronous reference frame vector control

7.3 Grid-side current control

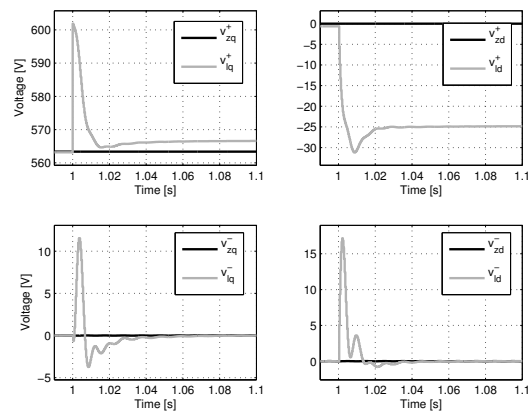


Figure 7.10: Evolution of the voltage applied on the AC side of the grid side inverter due to a step change in the current reference when using dual synchronous reference frame vector control

Chapter 8

Stationary reference frame DFIG control

8.1 Introduction

This chapter presents a stationary reference frame current control design for a DFIG-based WTGS which allows the machine to operate under unbalanced conditions.

As mentioned in the previous chapter, the dual synchronous reference frame vector control allows to extend the principles of the conventional vector control to the more general unbalanced case by using two vector controllers plus a filter which separates the positive from the negative sequence. The drawback of this design, as mentioned in the previous chapter, is that the complexity of the resulting controller is increased while the robustness and the performance obtained from the control is decreased in comparison to a conventional vector control design under balanced conditions.

The idea behind the stationary reference frame control is that by using the stationary reference frame, taking the derivative of the Park reference angle used by the controller as constant, the advantage of transforming the system magnitudes into constant values in steady state is lost but the design of controllers to operate under both balanced and unbalanced conditions is simplified and the resulting scheme can be compared in complexity and performance to those of the conventional vector control under balanced conditions.

The chapter is organized as follows: first the design of a stationary reference frame controller for the DFIG is analyzed in Section 8.2, then the same design procedure is used in Section 8.3 to control the AC grid side.

Chapter 8 Stationary reference frame DFIG control

8.2 Machine side control

To obtain the stationary reference frame equations of the DFIG, $\dot{\theta}$ is chosen as $\dot{\theta} \equiv 0$ in (3.21). This way, the Park transformation matrix $T(\theta)$ becomes a constant matrix which corresponds to the so called Clarke transformation matrix. Here, the qd notation will be replaced by $\alpha\beta$, which is a common way to tell the Clarke transformed variables from the synchronous reference frame Park transformed variables.

The machine equations become:

$$\begin{bmatrix} v_s^{\alpha\beta} \\ v_r^{\alpha\beta} \end{bmatrix} = \begin{bmatrix} L_s & 0 & M & 0 \\ 0 & L_s & 0 & M \\ M & 0 & L_r & 0 \\ 0 & M & 0 & L_r \end{bmatrix} \frac{d}{dt} \begin{bmatrix} i_s^{\alpha\beta} \\ i_r^{\alpha\beta} \end{bmatrix} + \begin{bmatrix} r_s & 0 & 0 & 0 \\ 0 & r_s & 0 & 0 \\ 0 & -\omega_r M & r_r & -\omega_r L_r \\ \omega_r M & 0 & \omega_r L_r & r_r \end{bmatrix} \begin{bmatrix} i_s^{\alpha\beta} \\ i_r^{\alpha\beta} \end{bmatrix} \quad (8.1)$$

From this equation, it can be seen that there exist a coupling between the electrical and mechanical variables because some terms in the equation depend on the mechanical speed of the machine. Also this dependance makes the system be nonlinear as there are products between state variables. Fortunately, as it was previously shown in Chapter 2, the mechanical dynamics are very slow, thus the generator speed can arguably be considered constant when studying the generator equations to design its current controllers.

Assuming the mechanical speed to have very slow dynamics compared to the electrical variables, there exist different possible ways to design the controller. Here, a decoupling feedback will be introduced in the control action which ideally will suppress the dependance of the electrical dynamics in the mechanical speed while also suppressing the existing coupling between the α and β variables. To do this, the voltage applied to the rotor windings will be computed as:

$$v_r^{\alpha\beta} = \hat{v}_r^{\alpha\beta} + \begin{bmatrix} 0 & -\omega_r M & 0 & -\omega_r L_r \\ \omega_r M & 0 & \omega_r L_r & 0 \end{bmatrix} \begin{bmatrix} i_s^{\alpha\beta} \\ i_r^{\alpha\beta} \end{bmatrix} \quad (8.2)$$

where $\hat{v}_r^{\alpha\beta}$ is the output of a current controller fed with the current error.

To verify the proper compensation of the terms which depend on ω_r and decouple α and β a simulation of the rotor current response when voltage

8.2 Machine side control

is applied to the stator windings of the machine in the direction of $v_{s\alpha}$. The simulation is performed in an averaged model of the system and the controllers are implemented as discrete time controllers with a sampling time of 3 kHz. The stator voltage input $v_s^{\alpha\beta}$ can be seen in Figure 8.1, the evolution of the rotor current and the voltage applied by the decoupling feedback are shown in Figure 8.2 and 8.3. The simulation is also performed for a range of generator speeds.

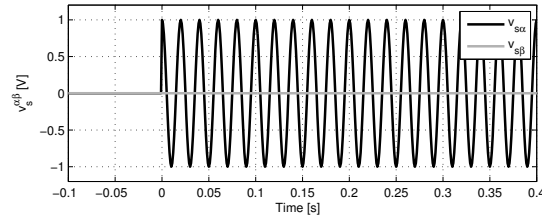


Figure 8.1: Stator voltage applied to test the decoupling feedback loop

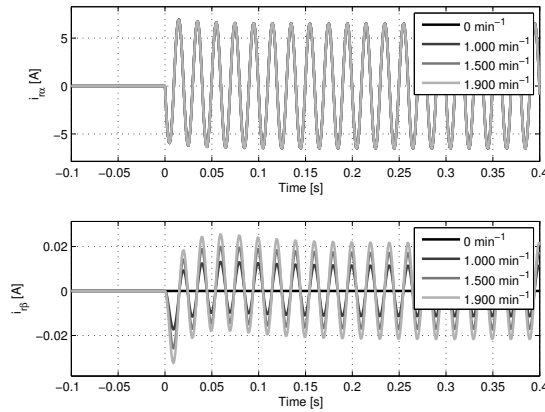


Figure 8.2: Rotor current evolution during the simulated test of the decoupling feedback loop

The simulation results show that although the compensation of the coupling terms is not perfect and certain dependance on the machine speed still exists which increases with the machine speed, the gain between $v_{s\alpha}$ and $i_{r\beta}$ is 50 dB lower than the gain between $v_{s\alpha}$ and $i_{r\alpha}$ in all cases. Thus the α and β components can arguably be considered to be decoupled when the

Chapter 8 Stationary reference frame DFIG control

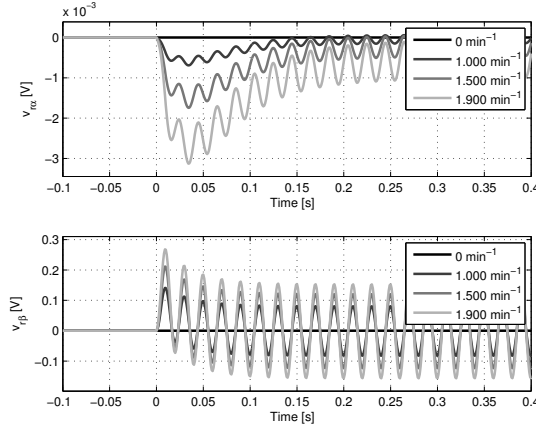


Figure 8.3: Rotor voltage applied by the decoupling feedback loop during its test simulation

decoupling loop is present and decoupled SISO controllers may be used to control them independently.

Doing the assumption that the compensation completely suppresses the coupling between α and δ , the machine equations (8.1) can be rewritten as:

$$\begin{bmatrix} v_s^{\alpha\beta} \\ \hat{v}_r^{\alpha\beta} \end{bmatrix} = \begin{bmatrix} L_s & 0 & M & 0 \\ 0 & L_s & 0 & M \\ M & 0 & L_r & 0 \\ 0 & M & 0 & L_r \end{bmatrix} \frac{d}{dt} \begin{bmatrix} i_s^{\alpha\beta} \\ i_r^{\alpha\beta} \end{bmatrix} + \begin{bmatrix} r_s & 0 & 0 & 0 \\ 0 & r_s & 0 & 0 \\ 0 & 0 & r_r & 0 \\ 0 & 0 & 0 & r_r \end{bmatrix} \begin{bmatrix} i_s^{\alpha\beta} \\ i_r^{\alpha\beta} \end{bmatrix} \quad (8.3)$$

The derivatives of the current can be put as a explicit function of the current and the voltage applied to the machine thus obtaining the usual state space representation of the equations:

$$\begin{aligned} \frac{d}{dt} \begin{bmatrix} i_s^{\alpha\beta} \\ i_r^{\alpha\beta} \end{bmatrix} &= \frac{1}{L_s L_r - M^2} \begin{bmatrix} r_s l_r & 0 & -r_r M & 0 \\ 0 & r_s L_r & 0 & -r_r M \\ -r_s M & 0 & r_r L_s & 0 \\ 0 & -r_s M & 0 & r_r L_s \end{bmatrix} \begin{bmatrix} i_s^{\alpha\beta} \\ i_r^{\alpha\beta} \end{bmatrix} \\ &+ \frac{1}{L_s L_r - M^2} \begin{bmatrix} L_r & 0 & -M & 0 \\ 0 & L_r & 0 & -M \\ -M & 0 & L_s & 0 \\ 0 & -M & 0 & L_s \end{bmatrix} \begin{bmatrix} v_s^{\alpha\beta} \\ \hat{v}_r^{\alpha\beta} \end{bmatrix} \quad (8.4) \end{aligned}$$

8.2 Machine side control

Transforming by Laplace the equations and solving for the current, the transfer function between the current and the voltage is obtained:

$$\begin{bmatrix} i_s^{\alpha\beta}(s) \\ i_r^{\alpha\beta}(s) \end{bmatrix} = \frac{1}{D(s)} \begin{bmatrix} L_r s + r_r & 0 & -Ms & 0 \\ 0 & L_r s + r_r & 0 & -Ms \\ -Ms & 0 & L_s s + r_s & 0 \\ 0 & -Ms & 0 & L_s s + r_s \end{bmatrix} \begin{bmatrix} v_s^{\alpha\beta}(s) \\ \hat{v}_r^{\alpha\beta}(s) \end{bmatrix} \quad (8.5)$$

with

$$D(s) = (L_s L_r - M^2) s^2 + (L_s r_r + L_r r_s) s + r_r r_s \quad (8.6)$$

Note that although α and β are decoupled, there exists a coupling between the stator and rotor variables.

The Laplace transform of the rotor current is:

$$i_r^{\alpha\beta}(s) = \frac{1}{D(s)} \begin{bmatrix} L_s s + r_s & 0 \\ 0 & L_s s + r_s \end{bmatrix} \hat{v}_r^{\alpha\beta}(s) + \frac{1}{D(s)} \begin{bmatrix} -Ms & 0 \\ 0 & -Ms \end{bmatrix} v_s^{\alpha\beta}(s) \quad (8.7)$$

Note that as α and β are decoupled and symmetrical, they can be controlled independently and the same controller can be used for both, thus from now on only the α equations will be displayed for the sake of simplicity.

The Laplace transform of $i_{r\alpha}$ is:

$$i_{r\alpha}(s) = \underbrace{\frac{L_s s + r_s}{(L_s L_r - M^2) s^2 + (L_s r_r + L_r r_s) s + r_r r_s}}_{G(s)} \hat{v}_{r\alpha}(s) - \underbrace{\frac{M}{(L_s L_r - M^2) s^2 + (L_s r_r + L_r r_s) s + r_r r_s}}_{G_d(s)} \hat{v}_{s\alpha}(s) \quad (8.8)$$

where $G(s)$ is the transfer function between $\hat{v}_{r\alpha}$ and $i_{r\alpha}$,
 $G_d(s)$ is the transfer function between $\hat{v}_{s\alpha}$ and $i_{r\alpha}$.

As $v_{s\alpha}$ is a exogenous signal that does not depend on the state of the system, it can be thought as an external disturbance when designing the current controller.

Chapter 8 Stationary reference frame DFIG control

To control the rotor current, a two degrees of freedom controller consisting in a feedback controller $K(s)$ fed with the error between the current reference signal $i_{r\alpha}^*$ and its actual value $i_{r\alpha}$ plus a feed-forward controller $K_d(s)$ fed with the measured disturbance $v_{s\alpha}$. The purpose of the feed-forward controller is to speed up and improve the compensation of the effect of the disturbance $v_{s\alpha}$. The diagram of the proposed controller is shown if Figure 8.4, note that the notation used in the diagram corresponds to a commonly used notation in control theory which identifies the reference signals as r , the system output as y , the disturbances as d , the error as e and the control action as u .

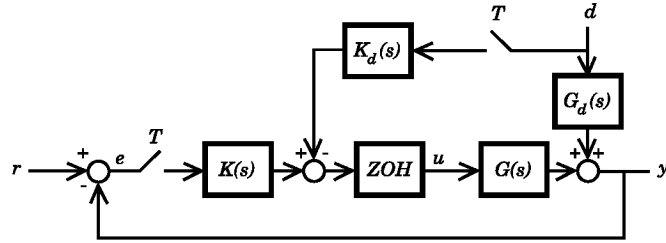


Figure 8.4: Proposed current control structure for the stationary reference frame controller of the DFIG.

In order to take into account the effect of the discrete time nature of the controller while using the continuous time controller design tools, the effect of the zero order hold will be approximated by a time delay of half a sampling period [31]. Figure 8.5 shows the resulting simplified scheme.

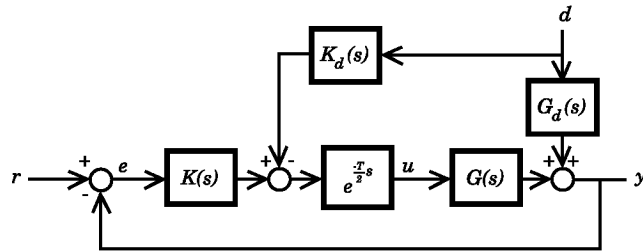


Figure 8.5: Simplified model of the generator control.

8.2.1 K_d feed-forward compensation design

When designing a feed-forward compensation to minimize the effect of the stator voltage disturbances on the current control of the machine, a common approach is to assume the stator resistance r_s to be small and the stator current to not have any influence in the rotor current. Then, from the equations of the generator (8.4) it is found that in order to completely suppress the effect of v_s on i_r , a very simple K_d , which will be referred as K_{d0} , can be used:

$$K_{d0} = -\frac{M}{L_s} \quad (8.9)$$

In order to verify the effectiveness of this compensator, a simulation of the response of the system to a change in the stator voltage is performed. Figure 8.6 shows the applied voltage disturbance and the effect that it has on the rotor current when no compensator is used. Figure 8.7 shows the evolution of the current when K_{d0} is used. Note that this simulations are performed using a controller which besides the feed-forward compensator, only contains the decoupling feedback loop previously designed. From the simulation results, it can be seen that the compensator greatly diminishes the effect of the stator voltage by reducing the gain of the stator voltage to the rotor current to one tenth. On the other hand, it gives a very slow transient.

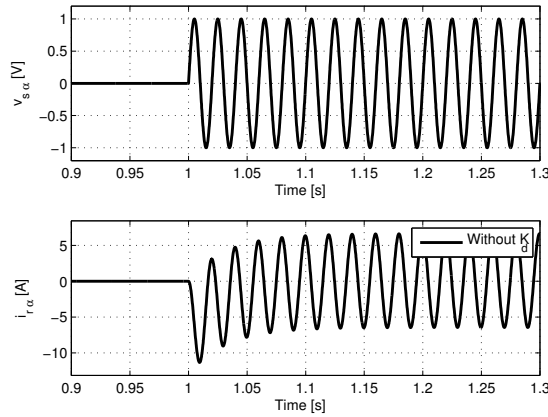


Figure 8.6: Simulated stator voltage disturbance to test the feed-forward compensator used by the stationary frame controller of the DFIG

Chapter 8 Stationary reference frame DFIG control

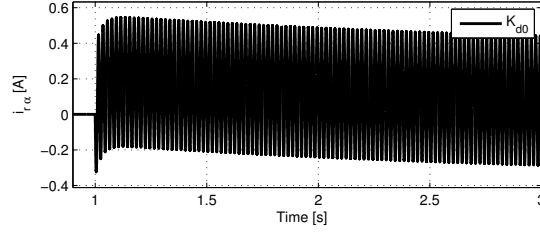


Figure 8.7: Simulated evolution of the rotor current under a stator voltage disturbance using the K_{d0} feed-forward controller

In order to improve the performance of the system, the effect of the stator current must be taken into account to properly compensate it. Considering a general feed-forward compensator $K_d(s)$ fed with the measured stator voltage, the transfer function between the current error and the stator voltage can be written as:

$$\frac{e(s)}{d(s)} = 1 - G(s)e^{-\frac{T}{2}s}K_d(s)G_d^{-1}(s) \quad (8.10)$$

From this equation it can be seen that in order to completely compensate the effect of $d(s)$, the desired feed-forward compensator transfer function $K_d(s)^*$ is:

$$K_d(s)^* = G_d(s)G^{-1}(s)e^{\frac{T}{2}s} \quad (8.11)$$

Note that this controller is acausal hence it is impossible to realize. Thus it can be stated that the effect of the stator voltage disturbances can not be completely suppressed by using a feed-forward controller. On the other hand, this function can be approximated using realizable transfer functions and a better approximation of this function will lead to better rejection of the disturbance.

The first possible approximation of (8.11) is obtained by suppressing its time delay:

$$K_{d1}(s) = G_d(s)G^{-1}(s) = \frac{-Ms}{L_s s + r_s} \quad (8.12)$$

This controller can be transformed into a difference equation using the Tustin bilinear transformation. This transformation maps the s plane of the Laplace transformation into the z plane of the Z transformation by using the following approximation:

8.2 Machine side control

$$z \approx \frac{1 - \frac{T_s}{2}s}{1 + \frac{T_s}{2}s} \quad (8.13)$$

Substituting the numerical values of the parameters of the system, the following transfer function in z is obtained:

$$K_{d1}(z) = \frac{-0,3921 + 0,3921z^{-1}}{1 - 0,9997z^{-1}} \quad (8.14)$$

In order to test the performance of this controller, a simulation is performed under the same conditions that were used to test K_{d0} . The resulting evolution of the current can be seen in Figure 8.8. It can be seen that K_{d1} improves the transient response of K_{d0} although in steady state the gain of the stator voltage over the rotor current is the same for both compensators.

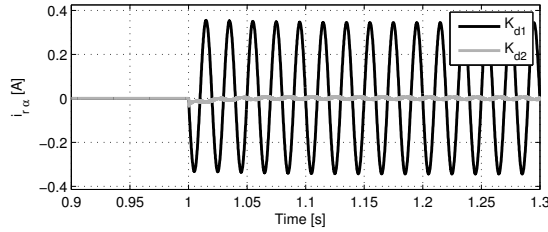


Figure 8.8: Current response for the stator voltage disturbance test of the feed-forward controllers K_{d1} and K_{d2} .

To explain this phenomenon a frequency analysis is performed on the transfer function of the ideal feed-forward compensator and its approximation. The bode plot of $K_d^*(s)$, $K_{d0}(s)$ and $K_{d1}(s)$ is shown in Figure 8.9 (note that the inverse of these functions is represented instead as the Matlab tools used to draw the bode plots require the transfer functions to be causal).

From the bode plot of these functions, it can be seen that both K_{d0} and K_{d1} provide the same degree of approximation of K_d^* around the grid frequency (50 Hz) whilst K_{d1} approximation is better for low frequencies, which explains why K_{d1} gives provides a better transient response.

One thing to note from the graph is that because of the phase delay caused by the zero order hold, the phase of K_{d0} and K_{d1} differs from K_d^* at the grid frequency, thus making the steady state response worse. In order to improve that, a phase advance controller can be put in series with the feed-forward in order to compensate the phase delay of the zero order hold. A new transfer function K_{d2} is then obtained:

Chapter 8 Stationary reference frame DFIG control

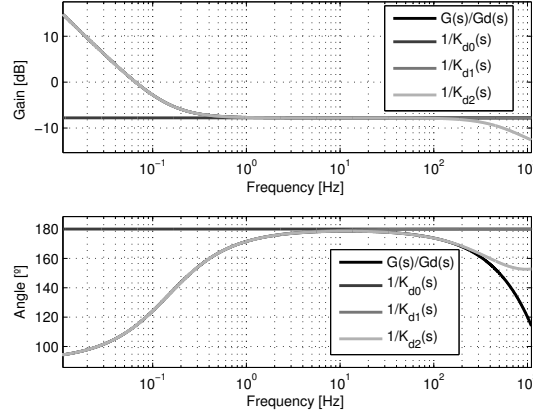


Figure 8.9: Bode plot of the inverse of the transfer function between the stator voltage and the rotor current along with the proposed feed-forward compensators.

$$K_{d2}(s) = \frac{2,7e-4s + 1}{1e-4s + 1} K_{d1}(s) \quad (8.15)$$

The bode plot of K_{d2} is shown in Figure 8.9. Notice that although the adjustment of the gain curve of K_{d2} becomes worse than K_{d1} due to the distortion caused by the phase advance controller, the adjustment of the phase is greatly improved.

In order to test the adequacy of the new controller, a simulation is performed under the same conditions as in the previous tests of K_{d0} and K_{d1} . As in the previous cases, the transfer function in the z domain of K_{d2} is obtained using the bilinear transformation:

$$K_{d2}(z) = \frac{-0,6421 + 0,794z^{-1} - 0,1519z^{-2}}{1 - 0,7497z^{-1} - 0,2499z^{-2}} \quad (8.16)$$

The controller response can be seen in Figure 8.8. The simulation results suggest that the addition of the phase advance controller greatly improves the performance of the compensator. Notice that as $K_d(s)$ is a feed-forward controller and it works in open loop, its performance is related to the adjustment of the model of the system used to design the controller to the actual dynamics of the system. The fact that the phase advance improves the response that much suggests that the adjustment of the phase in $K_d(s)$ is critical. Hence in order for $K_d(s)$ to be useful in a real implementation of

8.2 Machine side control

the controller, the different phase delays in the real system due to sensing of the system magnitudes, the communications and the modulation used to control the switching devices should be carefully measured and considered in the design of this controller.

8.2.2 K feedback controller design

The design of the feedback controller $K(s)$ will be done using an inverse-based loop shaping approach. This method is closely related to the so called Internal Model Control (IMC) [29]. The idea behind this method is that as the controller is connected in series with the system, the dynamics of the plant can be suppressed by including the inverse of the plant in the controller. Then, the controller transfer function can be obtained in a systematic way by multiplying the inverse of the plant transfer function by the desired open loop transfer function. On the other hand, care must be taken when the system transfer function contains non-invertible elements as unstable poles and zeros and time delays.

Considering the dynamics of the DFIG described by (8.8), neglecting the time delay due to the time discretization, the transfer function between the controller output voltage $\hat{v}_{r\alpha}$ and the rotor current $i_{r\alpha}$ is stable with no zeros with positive real part. Then, the controller can be obtained as:

$$K(s) = G^{-1}(s)L^*(s) \quad (8.17)$$

where $G^{-1}(s)$ is the inverse of the plant transfer function,
 $L^*(s)$ is the desired open loop transfer function.

The choice of $L^*(s)$ depends on the desired system performance and must be chosen so that the $K(s)$ is causal, that is, the degree of the denominator of $K(s)$ must be greater or equal to that of the numerator.

As an example of choice for $L^*(s)$, in case of need to have a good tracking of constant reference values, a common choice would be [32]:

$$L_1^*(s) = \frac{\omega_c}{s} \quad (8.18)$$

This open loop transfer function has a crossing frequency of ω_c , an infinite gain at 0 frequency, a gain tending to 0 as the frequency tends to infinite and a phase going from 0 degrees at zero frequency to 90 degrees for infinite frequency. The corresponding closed loop transfer function would be:

$$T_1^*(s) = \frac{i_{r\alpha}(s)}{i_{r\alpha}^*(s)} = \frac{1}{\frac{1}{\omega_c}s + 1} \quad (8.19)$$

Chapter 8 Stationary reference frame DFIG control

That would mean that for a constant reference value, the steady state error would be 0 and the close loop bandwidth would be approximately ω_c .

One drawback of this controller is that it would have an infinite gain at zero frequency and thus would require an anti-windup loop to avoid limit cycles and unwanted hard to predict nonlinear behavior due to the saturation of the control action. A possible solution for that is to limit the gain at zero frequency by replacing the integrator of $L_1^*(s)$ by a pole:

$$L_2^*(s) = \frac{\omega_c}{s + a} \quad (8.20)$$

In that case, if $\omega_c \gg a$, the crossing frequency would be approximately ω_c and the gain at 0 frequency would be:

$$\|L_2^*(0)\| \approx \frac{\omega_c}{a} \quad (8.21)$$

As the current reference signals in the stationary reference frame are sinusoidal time-varying of 50 Hz, it is wanted to have a high gain around 50 Hz instead of 0 [33]. To obtain a suitable transfer function a low-pass to band-pass frequency transformation, which is commonly used for filter design, can be applied to the previous equation, obtaining:

$$L^*(s) = L_2^*(s) \Big|_{s=\frac{s^2+\omega_0^2}{2s}} = \frac{\frac{2\omega_c}{\omega_0^2}s}{\frac{1}{\omega_0^2}s^2 + \frac{2a}{\omega_0^2}s + 1} = \frac{\frac{2\omega_c}{\omega_0^2}s}{\frac{1}{\omega_0^2}s^2 + \frac{2\zeta}{\omega_0}s + 1} \quad (8.22)$$

where ω_0 is the transformation frequency (here it is $2\pi 50$ rad s^{-1}),

ω_c is the approximate equivalent low pass crossing frequency of $L^*(s)$,

ζ is the damping of the poles of $L^*(s)$ which allows to tune the gain at ω_0 frequency ($\zeta = \frac{a}{\omega_0}$).

Here, the bandwidth is chosen to approximately match the bandwidth needed for the torque actuator considered when designing the speed control, which is 20 Hz. The gain at ω_0 is chosen to give a steady state error of 0,1%, by taking $\zeta = 4e-4$. The resulting controller is:

$$K(s) = \frac{0,2846s^3 + 9,088s^2 + 4,158s}{s^3 + 1,173s^2 + 9,87e4s + 9,119e4} \quad (8.23)$$

This transfer function is then transformed to z using the Tustin bilinear transformation for a sampling frequency of 3 kHz:

8.3 Grid-side current control

$$K(z) = \frac{0,2853 - 0,8528z^{-1} + 0,8498z^{-2} - 0,2823z^{-3}}{1 - 2,989z^{-1} + 2,988z^{-2} - 0,9996z^{-3}} \quad (8.24)$$

The Bode plot of $K(z)$ is shown in Figure 8.10 and the resulting closed loop transfer function $T(s)$ can be seen in Figure 8.11. Notice that the gain of the closed loop transfer function is approximately 0 dB around 50 Hz, which means that the controller provides a good tracking of the current reference signals. Also, the gain of $T(s)$ is always less than 0 dB, which is also desirable as it is a measure of robustness of the system [32]. Finally, note that the gain of $T(s)$ drops below -25 dB at frequencies above 200 Hz, which is also required in order to avoid amplifying possible additive high frequency noise from the current measures.

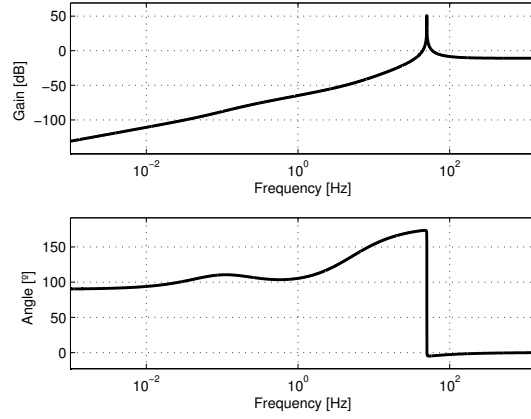


Figure 8.10: Bode plot of the DFIG feedback controller transfer function.

In order to test the performance of this controller, a simulation of the response of the system to a change in the reference current is performed. The evolution of the current compared to its reference value is shown in Figure 8.12. Notice that the system exhibits a damped response close to that of a first order system with a settling time which is approximately that of the specification.

8.3 Grid-side current control

In Chapter 5, the dynamical equations for the grid side system were obtained. From equation (5.19) we have that the relation between the grid

Chapter 8 Stationary reference frame DFIG control

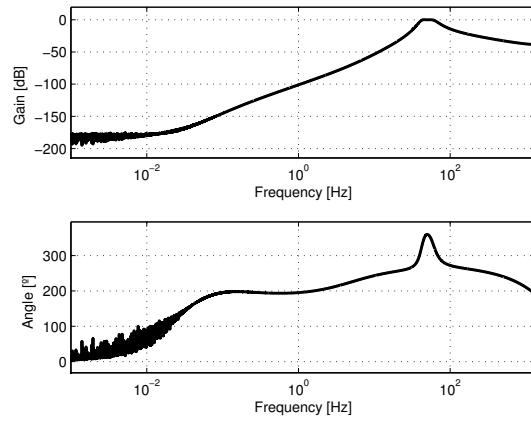


Figure 8.11: Bode plot of the closed loop transfer function of the current controller of the DFIG.

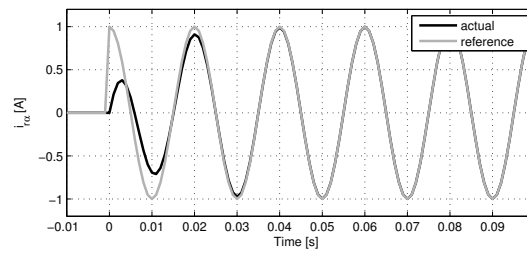


Figure 8.12: Simulated evolution of the DFIG rotor current for a current reference change.

8.3 Grid-side current control

side voltage and the current in the stationary reference frame can be written as:

$$v_l^{\alpha\beta} = r i_l^{\alpha\beta} + L \frac{d}{dt} i_l^{\alpha\beta} + v_z^{\alpha\beta} \quad (8.25)$$

This equation can be put in the conventional explicit state space representation as:

$$\frac{d}{dt} i_l^{\alpha\beta} = -\frac{r}{L} i_l^{\alpha\beta} + \frac{1}{L} v_l^{\alpha\beta} - \frac{1}{L} v_z^{\alpha\beta} \quad (8.26)$$

It can be seen that the dynamical equations are linear and decoupled between α and β , thus the controller design can be carried using single input single output (SISO) system design techniques. Also as the dynamics for both α and β are the same, for the sake of simplicity, from now on only α will be considered in the discussion as all the reasonings done for α can be directly transferred to β .

For the control design, the considered output variable will be the converter current i_l , the control variable will be the converter voltage v_l and the grid voltage v_z will be considered an exogenous disturbance signal which can be measured.

In Section 5.4 and 5.5 it was shown that in the stationary reference frame in both balanced and unbalanced conditions, the steady state magnitudes become time-varying sinusoidal signals. Thus for the controller design, unlike in the conventional regulation control design problems, here the frequency band of interest is located around the grid frequency instead of 0 frequency as both reference values and disturbances can no longer be considered constant values.

To design the controller, first the transfer functions in the Laplace domain for the system are obtained. By applying the Laplace Transformation to the α equation in (8.25) we obtain:

$$i_{l\alpha}(s) = \underbrace{\frac{1}{Ls + r}}_{G(s)} v_{l\alpha}(s) - \underbrace{\frac{1}{Ls + r}}_{G_d(s)} v_{z\alpha}(s) \quad (8.27)$$

where s is the Laplace variable,
 $G(s)$ is the plant transfer function,
 $G_d(s)$ is the disturbance transfer function.

The proposed control scheme is a two degrees of freedom controller consisting on a feed-forward disturbance rejection controller $K_d(s)$ fed with the

Chapter 8 Stationary reference frame DFIG control

grid voltage measurement plus a feedback controller $K(s)$ fed with the current error e . The proposed scheme is depicted on Figure 8.13. In order to use the conventional control theory signal notation, the current will be referred as the output variable y , whereas the current reference will be referred as r , the applied voltage will be referred as the control action u and the grid voltage will be referred as the disturbance d .

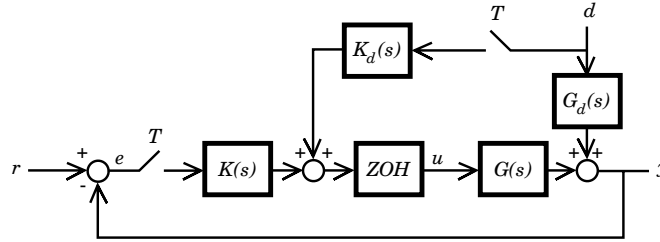


Figure 8.13: General current control system structure

In order to be able to use the continuous time linear systems analysis tools while taking into account the effect of discrete time nature of the digital implementation, there are a number of different possible well known strategies. The simplest approach is neglecting the effect of the time discretization, which is usually valid when the sampling frequency is reasonably high and the design bandwidth of the controller is low. A more accurate approach is the use of the so called Tustin bilinear transformation to map the z plane to the w plane in the discrete time system transfer function obtained by considering the zero order hold in series with the plant. Another common approach, which will be used here, is to approximate the effect of the zero order hold as a time delay of half the sampling period [31] as depicted on Figure 8.14.

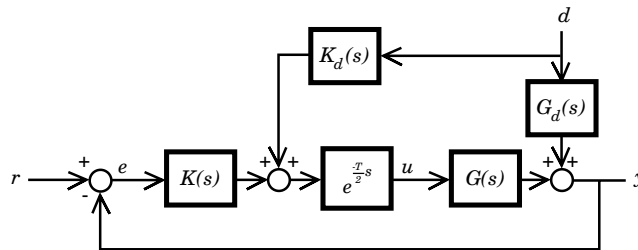


Figure 8.14: Simplified current control structure

8.3 Grid-side current control

8.3.1 K_d feed-forward compensation design

A feed-forward compensator is designed prior to the feedback controller to minimize the effect of the grid voltage disturbances to the current control. To design the feed-forward controller, first the transfer function between the system error and the disturbance is deduced from the simplified diagram (Figure 8.14) by suppressing the feedback controller:

$$\frac{e(s)}{d(s)} = -G_d(s) - G(s)e^{-\frac{T}{2}s}K_d(s) \quad (8.28)$$

For a good compensation the $K_d(s)$ is desired to be:

$$K_d(s) \approx -e^{\frac{T}{2}s}G(s)^{-1}G_d(s) \quad (8.29)$$

As in this system $G(s) = -G_d(s)$ according to (8.27), this can further be simplified to:

$$K_d(s) \approx e^{\frac{T}{2}s} \quad (8.30)$$

As $e^{\frac{T}{2}s}$ is not causal and thus it is not a realizable transfer function, the first obvious choice is to ignore the time delay due to the zero order hold and choose K_d to be 1. Thus the first compensator option to be evaluated will be $K_{d0} = 1$.

To be able to evaluate the performance of the feed-forward controller, the response of the grid current to a 50% grid voltage sag is simulated. The parameters for the simulation are shown on Table 8.1. The grid voltage is considered to not depend on the grid voltage and its forced evolution can be seen on Figure 8.15. The simulation is carried in two different models: the first model uses an averaged converter model by considering the voltage applied to be continuously varying according to the controller command, the second simulation is carried using a switching model where the voltage is applied by the converter by PWM.

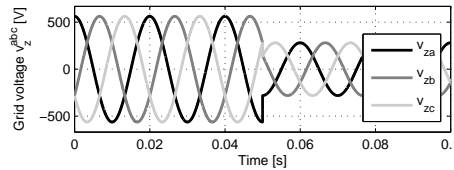
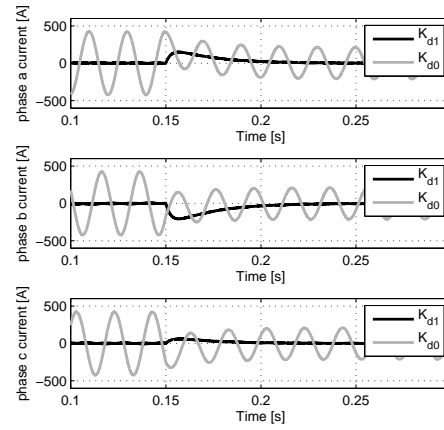
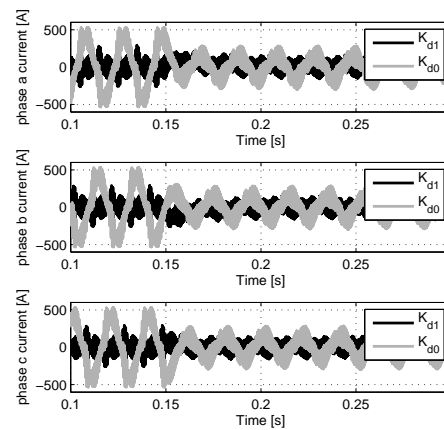


Figure 8.15: Grid voltage evolution for the K_d feed-forward controller simulation.

Chapter 8 Stationary reference frame DFIG control



(a) Averaged model simulation



(b) Switching model simulation

Figure 8.16: Current response to a voltage disturbance comparing K_{d0} and K_{d1} .

8.3 Grid-side current control

Symbol	Value	Units	Description
r	0,01	Ω	Grid connection inductance resistance
L	0,0069	Ω	Grid connection inductance
ω_e^N	50	s^{-1}	Grid nominal frequency
V_z^N	690	V	Nominal phase to phase rms grid voltage
α	50	%	Voltage sag amplitude
T_c	0,34	ms	Converter switching period (3 kHz)
T_s	T_c	1	Controller sampling period

Table 8.1: Grid connection converter parameters.

The obtained current evolution for the K_{d0} compensator can be seen on Figure 8.16 for both models.

Unlike in regulation problems with constant disturbances, here it is seen that the time delay produces a phase difference between the grid voltage and the applied compensation voltage which makes the feed-forward compensation less effective, even in steady state. As mentioned before, to obtain a better compensation, one should invert the time delay in the feed-forward controller, which would mean making a non-causal controller. This option is sometimes valid when the feed-forward input comes from the reference instead of the disturbance measurement as sometimes it is possible to have a prediction of the future value of the reference, thus this option is sometimes used in robot manipulator control loops [32]. Here, this option is not valid and the inverse of the time delay must be approximated by means of causal controllers. One possible way to do that is to use the transfer function of a phase-advance controller, which is well known from the classic linear control theory based on the frequency domain. The transfer function for a phase-advance controller can be written as:

$$K_{d1} = K \frac{s + \frac{1}{T}}{s + \frac{1}{aT}} \quad (8.31)$$

where K is a design parameter used to adjust the desired gain,
 a is a design parameter used to adjust the desired phase increase,
 T is a design parameter used to adjust the frequency for the phase increase.

If Φ is the desired phase increase, a can be calculated as:

$$a = \frac{1 - \sin \Phi}{1 + \sin \Phi} \quad (8.32)$$

Chapter 8 Stationary reference frame DFIG control

If ω_0 is the central frequency for the phase increase, it can be chosen as:

$$T = \frac{1}{\omega_0 \sqrt{a}} \quad (8.33)$$

Finally if it is wanted to have a unitary gain on K_{d1} for ω_0 , K can be adjusted as:

$$K = \frac{1}{\sqrt{a}} \quad (8.34)$$

To properly compensate the delay due to the zero order hold at the nominal grid voltage frequency, the phase increase at the nominal grid frequency should be:

$$\Phi(\omega_e^N) = \omega_e^N \frac{T_s}{2} \quad (8.35)$$

Choosing ω_0 and Φ to obtain the best approximation of $e^{\frac{T}{2}s}$ is a difficult task which can only be solved by using numerical optimization. One suboptimal choice which warrants the correct phase delay at the nominal frequency would be to choose $\omega_0 \equiv \omega_e^N$. In this case, the obtained controller is:

$$K_{d1}(s) = \frac{1,054s + 314,2}{s + 331,1} \quad (8.36)$$

To obtain the discrete time transfer function to be implemented in the digital controller, the Tustin bilinear transformation is applied to this transfer function as:

$$z \approx \frac{1 - \frac{T_s}{2}s}{1 + \frac{T_s}{2}s} \quad (8.37)$$

Thus obtaining:

$$K_{d1}(z) = \frac{1,048 - 0,9491z^{-1}}{1 - 0,8954z^{-1}} \quad (8.38)$$

The bode plots for both K_{d0} , K_{d1} and the desired ideal feed-forward compensator are plotted on Figure 8.17. Notice that K_{d1} gives a better approximation than K_{d0} which matches the gain and the phase of the desired compensator at the nominal grid frequency, which means that in steady state the compensator will provide a nearly perfect compensation of the disturbance whilst during the transients the small disadjustments between

8.3 Grid-side current control

the ideal compensator and K_{d1} will make the compensation less effective. Notice also that as mentioned before, one way to improve the compensation obtained with K_{d1} could be to make ω_0 slightly higher than ω_e^N in order to improve the adjustment of the phase around the nominal frequency thus improving the transient response of the compensator. As the adjustment of the gain would also change, numerical methods should be used to design the transfer function parameters.

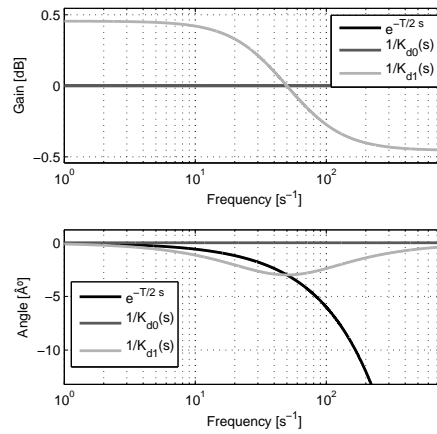


Figure 8.17: Bode plot comparing K_{d0} , K_{d1} and the ideal feed-forward compensator.

As with K_{d0} , the current response to a voltage variation is simulated in both averaged and switched models to test both the obtained steady and transient response. The obtained results can be seen on Figure 8.16 compared to the K_{d0} response. It is seen that K_{d1} provides a better compensation than K_{d0} although in the switching model the difference is less noticeable due to the presence of the switching noise which at low power levels become important due to the low mean value of the current.

8.3.2 K feedback controller design

For the feedback controller design an inverse based controller scheme will be used. The main idea of this approach is that for a system with invertible dynamics, it is possible to systematically design a controller $K(s)$ for it by choosing a desired $L(s)^*$ open loop transfer function and multiplying it by the inverse of the plant dynamics.

Chapter 8 Stationary reference frame DFIG control

One common problem of this approach is that when the system has unstable poles or non minimum phase zeros, the plant dynamics can no longer be inverted in order to avoid internal instability of the system. In this case, as mentioned in the previous section, a time delay has been used to approximate the effect of the time discretization of the controllers thus the dynamics of the plant cannot be inverted because of the non-causality of the resulting controller.

The effect of having a time delay in the control loop is that the phase of the open loop transfer function becomes worse and the system becomes less robust. Also depending on the amount of delay, the desired system performance may become impossible to obtain. In this case the time delay depends on the sampling period of the controller, which in turn depends on the switching frequency of the converter which is a design parameter of the converter which should be chosen according the expected performance of the converter among other things.

The first approach will be to ignore the time delay and expect the high gain of the controller to be able to compensate for it in closed loop on the band of interest. Thus $K(s)$ will be chosen as:

$$K(s) \approx G^{-1}(s)L^*(s) \quad (8.39)$$

Choosing $L^*(s)$ is complex task which depends on the desired system closed loop performance and the limitations of the actual system. Here the prototype function will be obtained by applying the filter design techniques to transform a regulation problem prototype function to the band of interest.

For regulation problems, where proportional integral (PI) controllers come in use, usually it is wanted to have a zero steady state error for constant references and a desired ω_c crossover frequency which is related to the bandwidth of the closed loop system. Both objectives can be obtained by having a open loop transfer function of the form:

$$L_1^*(s) = \frac{\omega_c}{s} \quad (8.40)$$

One disadvantage of this choice is that usually for systems of type 0, the controller must have an integrator and in some situations this might lead to control action saturation and windup effects. To avoid this problem, usually anti-windup modifications are used to limit the integrator values. One different choice is to limit the gain at 0 frequency of the controller by substituting the integrator by a non-zero stable pole of the form:

$$L_2^*(s) = \frac{\omega_c}{s + a} \quad (8.41)$$

8.3 Grid-side current control

as $\omega_c \gg a$, usually this maintains approximately the same crossover frequency.

In this case, it is wanted to follow sinusoidal time varying references instead of constant values, thus the aforementioned function prototypes are not valid. To obtain a valid prototype function, a low pass to band pass transfer function transformation from the well known classic linear filter design techniques will be applied to $L_2^*(s)$, obtaining:

$$L^*(s) = L_2^*(s) \Big|_{s=\frac{s^2+\omega_0^2}{2s}} = \frac{\frac{2\omega_c}{\omega_0^2}s}{\frac{1}{\omega_0^2}s^2 + \frac{2a}{\omega_0^2}s + 1} = \frac{\frac{2\omega_c}{\omega_0^2}s}{\frac{1}{\omega_0^2}s^2 + \frac{2\zeta}{\omega_0}s + 1} \quad (8.42)$$

- where
- ω_0 is the nominal frequency of the current references to be followed,
 - ω_c is the equivalent low-pass approximate crossover frequency of $L^*(s)$,
 - ζ is the damping ratio of the poles of $L^*(s)$ which can be used to adjust the gain at the nominal frequency.

For the controller design, the controller parameters are chosen as $\omega_0 = \omega_e^N = 2\pi \cdot 50 \text{ rad s}^{-1}$, $\omega_c = 20 \text{ Hz}$ and $\zeta = 4\text{e-}4$. In order to obtain a 0,1% of error and an approximate 50 ms settling time for 50 Hz current reference signals. The obtained transfer function is:

$$K(s) = \frac{1,398\text{e-}06s^2 + 6,366\text{e-}05s}{1,013\text{e-}05s^2 + 2,546\text{e-}06s + 1} \quad (8.43)$$

The bode plot of the obtained controller transfer function can be seen on Figure 8.18. Also the resulting open loop and the closed loop transfer functions can be seen on Figure 8.19. From the open loop bode plot it is found that the closed loop system has a gain margin of $GM = 20 \text{ dB}$, which is very good considering that usually it is recommended to be higher than 6 dB, and a phase margin of $PM = 83^\circ$ which is also good as usually it is recommended to be higher than 40° , thus according to this performance measures, the system is expected to be robust Notice also that the closed loop transfer function doesn't have any peak over 0 dB, that is $M_T \leq 0 \text{ dB}$ which is also a measure of robustness closely related to the GM and PM and it is recommended to be less than 2 dB [32].

Transforming this equation using the Tustin transformation the discrete time transfer function is obtained as:

$$K(z) = \frac{0,1387 - 0,2752z^{-1} + 0,1366z^{-2}}{1 - 1,989z^{-1} + 0,9999z^{-2}} \quad (8.44)$$

Chapter 8 Stationary reference frame DFIG control

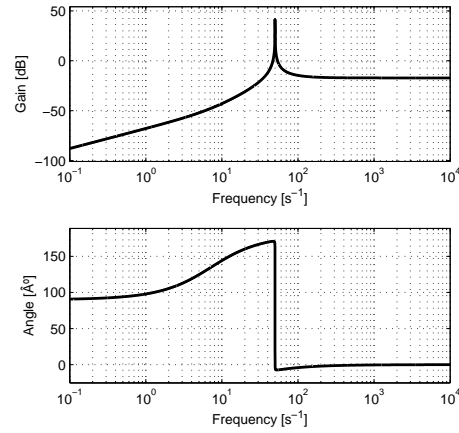


Figure 8.18: Bode plot of the controller transfer function $K(s)$.

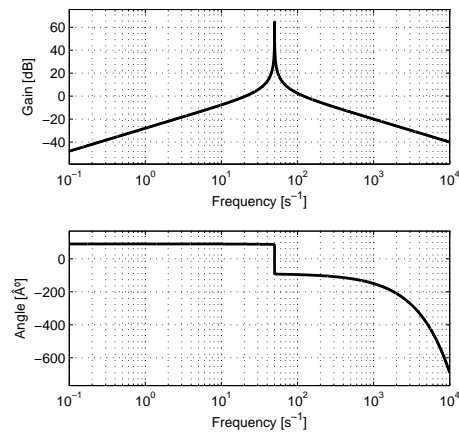
To evaluate the performance obtained with this controller a simulation of the response of the system to a change in the reference current is carried on both the averaged and the switching models. The parameters of the simulation are shown on Table 8.2.

Symbol	Value	Units	Description
V_z	690	V	Phase to phase rms grid voltage
$I_{l\alpha}(t_0)$	0	A	Rms of $i_{l\alpha}$ before the reference change
$I_{l\alpha}(t_f)$	420	A	Rms of $i_{l\alpha}$ after the reference change
$I_{l\beta}$	0	A	Rms of $i_{l\beta}$ for the whole the simulation

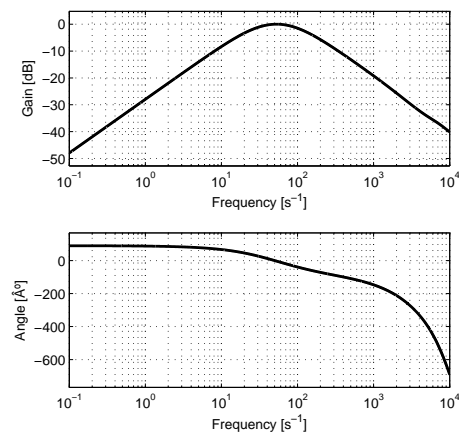
Table 8.2: Parameters for the simulation of the current reference value.

The simulated evolution of the grid currents is shown on Figure 8.20.

8.3 Grid-side current control



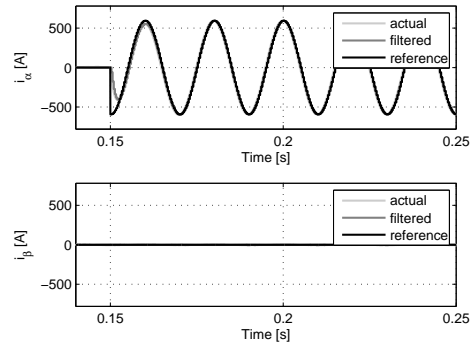
(a) Open loop transfer function



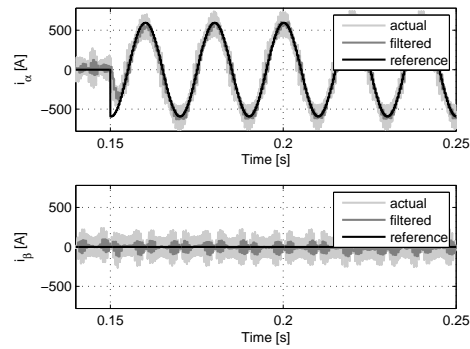
(b) Closed loop transfer function

Figure 8.19: Bode plots of the open loop and closed loop transfer functions.

Chapter 8 Stationary reference frame DFIG control



(a) Averaged model simulation



(b) Switching model simulation

Figure 8.20: Current response to a current reference change comparing the averaged and the switching model evolution. The light grey line on the graph corresponds to the actual current, the dark gray line corresponds to the current measurement sampled by the controller and the black line corresponds to the current reference value.

8.3 Grid-side current control

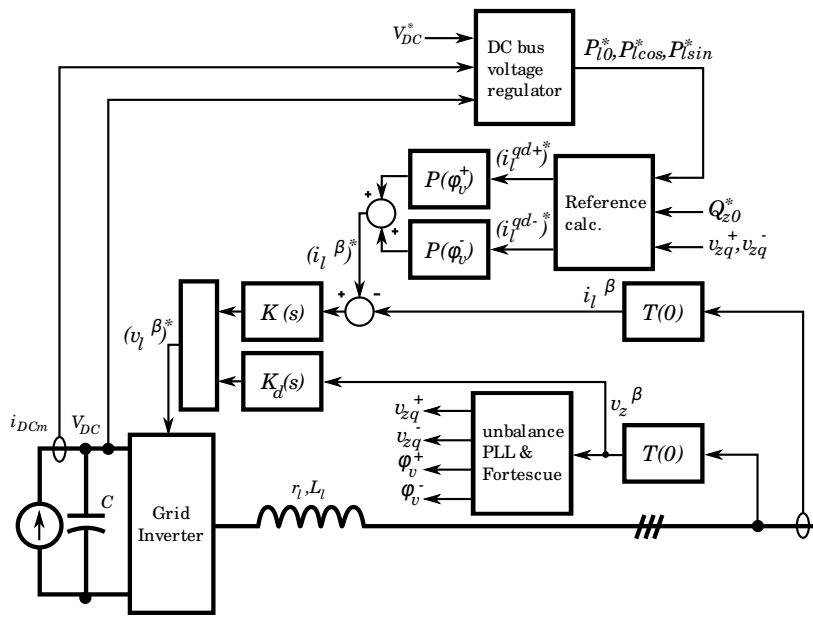


Figure 8.21: Scheme of the proposed controller

Chapter 9

VSC reference calculation issues for unbalanced operation

9.1 Introduction

VSCs are used in a number of applications ranging from low voltage microgrid applications [34] to large high voltage DC VSC for offshore wind generation [35]. VSC has been successfully used as a grid connection interface for most renewable energy sources as DFIG and PMSG wind turbines and photovoltaic panels.

The increasing penetration of renewable energy in the grid, has brought a need to develop new methodologies of control for this devices to allow them to remain connected to the grid during different types of grid disturbances and avoid having to disconnect, a feature which is commonly known as ride-through.

Voltage sags are the most frequent type of grid disturbances. They are reductions of the voltage amplitude and are usually classified between balanced, when the reduction of the voltage is the same for each phase, and unbalanced otherwise. Balanced voltage sags are usually caused by the starting transients of large machines and three phase short circuits. Unbalanced voltage sags are caused by single phase or two phase short-circuits and are the most common type of sags [36].

Ride-through capabilities for unbalanced voltage sags present a number of challenges. The existence of negative sequence components in the voltage causes a ripple in the power injected to the AC grid. This causes the DC bus voltage to also have a ripple which in some cases may be critical. Also, the existence of negative sequence voltage causes negative sequence current to appear which needs to be controlled. Conventional vector control is designed to control positive sequence currents and it exhibits poor performance when controlling negative sequence. Different choices for alternative designs of the current controllers exist such as the double synchronous reference frame vec-

Chapter 9 VSC reference calculation issues for unbalanced operation

tor control and the stationary frame current control described in the previous chapters. A number of different control methods can also be found in the literature: in [11] a current reference calculation scheme was proposed that enables suppressing the active power oscillations during unbalanced voltage sags using conventional SRFVC with enhanced current controllers able to track a reference current signals containing both positive and negative sequence. In [37] a different current control design with a double SRFVC and independent controllers for positive and negative components was introduced. In [38] and [7] this current control is used for a coordinated control of the back-to-back converter of a DFIG turbine to enable the suppression of the machine torque and the ripple of the DC bus voltage caused by the network unbalances. In [39] a double SRFVC using linear quadratic regulators (LQR) current controllers is proposed for the operation of a PMSG wind turbine under unbalanced voltage sags. In [40] and [41], coordinated control of the back-to-back converter of the DFIG using stationary frame current control with proportional-resonant controllers is proposed. Stationary frame control has also been proved to provide good performance under unbalance operation of VSC while simplifying the structure of the current controller [42].

The previously mentioned works use current reference calculation methods deriving from the one introduced in [11] which uses negative sequence current to compensate for the oscillation of the power due to the presence of negative sequence in the grid voltage. The present chapter analyzes this method and provides a critic analysis and some remarks on its limitations and some important weak points which to the best of the knowledge of the author have not been addressed in the past. Also, modifications of the method to solve for this problems are proposed.

This chapter is organized as follows: the equations of a VSC from Chapter 5 are used in Section 9.2 to analyze the steady state for balanced operation and to obtain the current reference calculation equations of the conventional vector control. In Section 9.3 the steady state equations for unbalanced operation are obtained and the current reference calculation formulas to control the power output of the converter are derived and discussed. Finally the conclusions drawn in the previous section are tested on a simulation model in Section 9.4 and on an experimental platform in Section 9.5.

9.2 Analysis of the current reference calculation for balanced operation

9.2 Analysis of the current reference calculation for balanced operation

According to [26], a generic $x^{abc}(t)$ three phase positive sequence signal is a function of time that can be described as:

$$x^{abc}(t) = \sqrt{2}X \begin{bmatrix} \cos(\omega_e t + \varphi_x) \\ \cos(\omega_e t + \varphi_x - \frac{2\pi}{3}) \\ \cos(\omega_e t + \varphi_x + \frac{2\pi}{3}) \end{bmatrix} \quad (9.1)$$

By choosing the $\frac{d}{dt}\theta = \omega_e$ for the Park reference angle, the transformed signal becomes a vector of constants:

$$x^{qd0}(t) = T(\omega_e t + \varphi)x^{abc} = \sqrt{2}X \begin{bmatrix} \cos(\varphi_x - \varphi) \\ -\sin(\varphi_x - \varphi) \\ 0 \end{bmatrix} \quad (9.2)$$

We define:

$$\begin{bmatrix} x_q^{ss} \\ x_d^{ss} \end{bmatrix} \triangleq \begin{bmatrix} \sqrt{2}X \cos(\varphi_x - \varphi) \\ -\sqrt{2}X \sin(\varphi_x - \varphi) \end{bmatrix} \quad (9.3)$$

Considering a balanced case where both the inverter voltage v_l^{abc} and the grid voltage v_z^{abc} are positive sequence signals, choosing θ to match the angle of v_{za} and assuming the derivatives of the current to become zero in steady state, the following relations can be obtained from (5.16):

$$\begin{cases} v_{lq}^{ss} - v_{zq}^{ss} = r_l i_{lq}^{ss} + L_l \omega_e i_{ld}^{ss} \\ v_{ld}^{ss} = r_l i_{ld}^{ss} - L_l \omega_e i_{lq}^{ss} \end{cases} \quad (9.4)$$

These equations can be used to solve for the current needed to have a certain steady state power. According to [43], active and reactive power can be calculated using the voltage and current in the qd form as:

$$\begin{cases} P &= \frac{3}{2} (v_q i_q + v_d i_d) = \frac{3}{2} \{v^{qd}\}^T \begin{bmatrix} 1 & 0 \\ 0 & 1 \end{bmatrix} i^{qd} \\ Q &= \frac{3}{2} (v_q i_d - v_d i_q) = \frac{3}{2} \{v^{qd}\}^T \begin{bmatrix} 0 & 1 \\ -1 & 0 \end{bmatrix} i^{qd} \end{cases} \quad (9.5)$$

Substituting for the grid connection point:

$$\begin{cases} P_z &= \frac{3}{2} v_{zq} i_{lq} \\ Q_z &= \frac{3}{2} v_{zq} i_{ld} \end{cases} \quad (9.6)$$

Chapter 9 VSC reference calculation issues for unbalanced operation

Assuming v_{zd} to be zero, which can be ensured by an adequate tracking of the grid voltage measure using a phase locked loop (PLL), (9.6) implies that active and reactive power are proportional to the i_{lq} and i_{ld} respectively. This is commonly used to calculate a current reference value for the current control from a power reference signal usually generated by the DC bus voltage regulator and a reactive power command:

$$\begin{cases} i_{lq}^* = \frac{2}{3} \frac{P_z^*}{v_{zq}} \\ i_{ld}^* = \frac{2}{3} \frac{Q_z^*}{v_{zq}} \end{cases} \quad (9.7)$$

One drawback of this reference calculation method is that it ignores the power loss due to the resistance of the converter filter and its dynamic behavior. Thus even having a perfect current control, the active power output of the converter P_l will not be equal to the power on the grid connection point P_z and the DC bus voltage regulator will need to be able to compensate for that difference. Usually this is not a important issue as the filter resistance is small and the regulators used to control the DC bus are designed for disturbance rejection. On the other hand, one possible workaround to match the DC bus voltage regulator power command to the actual power output by the inverter in steady state is to subtract the losses due to the filter to the active power reference value:

$$P_z^* = P_l^* - r_l \left((i_{lq}^*)^2 + (i_{ld}^*)^2 \right) \quad (9.8)$$

Note that i_{lq}^* and i_{ld}^* depend on the choice of P_z^* . As the losses due to filter resistance will be very small in comparison with P_l^* , the actual solution may be close to the initial guess P_l^* , thus one possible approach is to iteratively solve for the current as:

$$\begin{cases} \left(i_{lq}^* \right)_{n+1} = \frac{2}{3} \frac{(P_z^*)_n}{v_{zq}} \\ \left(i_{ld}^* \right)_{n+1} = \frac{2}{3} \frac{(Q_z^*)_n}{v_{zq}} \end{cases} \quad (9.9)$$

with

$$(P_z^*)_n = P_l^* - r_l \left((i_{lq}^*)_n^2 + (i_{ld}^*)_n^2 \right) \quad (9.10)$$

9.3 Analysis of the current reference calculation for unbalanced operation

According to [26] a three phase signal with positive and negative sequence components can be described as:

$$x^{abc}(t) = x_+^{abc}(t) + x_-^{abc}(t) \quad (9.11)$$

9.3 Analysis of the current reference calculation for unbalanced operation

where

$$x_+^{abc}(t) = \sqrt{2}X^+ \begin{bmatrix} \cos(\omega_e t + \varphi_x^+) \\ \cos(\omega_e t + \varphi_x^+ - \frac{2\pi}{3}) \\ \cos(\omega_e t + \varphi_x^+ + \frac{2\pi}{3}) \end{bmatrix} \quad (9.12)$$

$$x_-^{abc}(t) = \sqrt{2}X^- \begin{bmatrix} \cos(\omega_e t + \varphi_x^-) \\ \cos(\omega_e t + \varphi_x^- + \frac{2\pi}{3}) \\ \cos(\omega_e t + \varphi_x^- - \frac{2\pi}{3}) \end{bmatrix} \quad (9.13)$$

Unlike in the balanced case, here it is not possible to transform the time varying signal $x^{abc}(t)$ into a constant signal by using the Park variable change matrix. On the other hand it is possible to decompose the system in two decoupled systems corresponding to the positive and the negative sequence which can be analyzed using the same procedure as in the balanced case due to the linear properties of the dynamics of the system and the symmetrical nature of its impedances [26].

The positive sequence magnitudes can be transformed into constant signals by choosing a Park reference angle matching the angle of the a phase of the original signal:

$$x_+^{qd}(t) = T(\omega_e t + \varphi^+) x_+^{abc}(t) = \sqrt{2}X^+ \begin{bmatrix} \cos(\varphi_x^+ - \varphi^+) \\ -\sin(\varphi_x^+ - \varphi^+) \end{bmatrix} \quad (9.14)$$

while the negative sequence magnitudes can be transformed into constants by choosing θ to be equal to the angle of the a phase multiplied by -1:

$$x_-^{qd}(t) = T(-\omega_e t - \varphi^-) x_-^{abc}(t) = \sqrt{2}X^- \begin{bmatrix} \cos(\varphi_x^- - \varphi^-) \\ \sin(\varphi_x^- - \varphi^-) \end{bmatrix} \quad (9.15)$$

As in the balanced case we define the steady state components in the synchronous reference frame as:

$$\begin{bmatrix} x_q^+ \\ x_d^+ \end{bmatrix} \triangleq \begin{bmatrix} \sqrt{2}X^+ \cos(\varphi_x^+ - \varphi^+) \\ -\sqrt{2}X^+ \sin(\varphi_x^+ - \varphi^+) \end{bmatrix} \quad (9.16)$$

and

$$\begin{bmatrix} x_q^- \\ x_d^- \end{bmatrix} \triangleq \begin{bmatrix} \sqrt{2}X^- \cos(\varphi_x^- - \varphi^-) \\ \sqrt{2}X^- \sin(\varphi_x^- - \varphi^-) \end{bmatrix} \quad (9.17)$$

Also, as in the balanced case, the steady state equations can be obtained from (5.16) by assuming the derivatives of the current to be zero:

$$\begin{cases} v_{lq}^+ - v_{zq}^+ = r_l i_{lq}^+ + L_l \omega_e i_{ld}^+ \\ v_{ld}^+ = r_l i_{ld}^+ - L_l \omega_e i_{lq}^+ \end{cases} \quad (9.18)$$

Chapter 9 VSC reference calculation issues for unbalanced operation

and

$$\begin{cases} v_{lq}^- - v_{zq}^- = r_l i_{lq}^- - L_l \omega_e i_{ld}^- \\ v_{ld}^- = r_l i_{ld}^- + L_l \omega_e i_{lq}^- \end{cases} \quad (9.19)$$

As of the power equations (9.5), they include multiplications between voltage and current, thus they are not linear and it is no longer possible to separate positive and negative sequence, as there will be crossed products of terms from both. To calculate the power, the steady state positive and negative sequence magnitudes are transformed to a common reference frame with $\theta = 0$ as:

$$P = \frac{3}{2} \{ R(-\omega_e t - \varphi^+) v_+^{qd} + R(\omega_e t + \varphi^-) v_-^{qd} \}^T \cdot \begin{bmatrix} 1 & 0 \\ 0 & 1 \end{bmatrix} \left(R(-\omega_e t - \varphi^+) i_+^{qd} + R(\omega_e t + \varphi^-) i_-^{qd} \right) \quad (9.20)$$

and

$$Q = \frac{3}{2} \{ R(-\omega_e t - \varphi^+) v_+^{qd} + R(\omega_e t + \varphi^-) v_-^{qd} \}^T \cdot \begin{bmatrix} 0 & 1 \\ -1 & 0 \end{bmatrix} \left(R(-\omega_e t - \varphi^+) i_+^{qd} + R(\omega_e t + \varphi^-) i_-^{qd} \right) \quad (9.21)$$

where $R(\theta)$ is a rotation matrix defined as:

$$R(\theta) = \begin{bmatrix} \cos(\theta) & -\sin(\theta) \\ \sin(\theta) & \cos(\theta) \end{bmatrix} \quad (9.22)$$

Note that it can easily be proven that the following relation exists between $T(\theta)$ and $R(\theta)$:

$$T(\theta) \equiv \begin{bmatrix} R(\theta) & 0 \\ 0 & 1 \end{bmatrix} T(0) \quad (9.23)$$

The resulting equation of the active power can be written as:

$$P = P_0 + P_{\cos} \cos(2\omega_e t + \varphi^+ + \varphi^-) + P_{\sin} \sin(2\omega_e t + \varphi^+ + \varphi^-) \quad (9.24)$$

where

$$\begin{cases} P_0 = \frac{3}{2} (v_q^+ i_q^+ + v_d^+ i_d^+ + v_q^- i_q^- + v_d^- i_d^-) \\ P_{\cos} = \frac{3}{2} (v_q^+ i_q^- + v_d^+ i_d^- + v_q^- i_q^+ + v_d^- i_d^+) \\ P_{\sin} = \frac{3}{2} (-v_q^+ i_d^- + v_d^+ i_q^- + v_q^- i_d^+ - v_d^- i_q^+) \end{cases} \quad (9.25)$$

The reactive power expression can be written as:

$$Q = Q_0 + Q_{\cos} \cos(2\omega_e t + \varphi^+ + \varphi^-) + Q_{\sin} \sin(2\omega_e t + \varphi^+ + \varphi^-) \quad (9.26)$$

9.3 Analysis of the current reference calculation for unbalanced operation

where

$$\begin{cases} Q_0 = \frac{3}{2} (v_q^+ i_d^+ - v_d^+ i_q^+ + v_q^- i_d^- - v_d^- i_q^-) \\ Q_{\cos} = \frac{3}{2} (v_q^+ i_d^- - v_d^+ i_q^- + v_q^- i_d^+ - v_d^- i_q^+) \\ Q_{\sin} = \frac{3}{2} (v_q^+ i_q^- + v_d^+ i_d^- - v_q^- i_q^+ - v_d^- i_d^+) \end{cases} \quad (9.27)$$

Unlike the balanced case, the steady state active and reactive power contains a constant component plus time-varying sine components with a frequency of twice the grid frequency. Also, although six power magnitudes were defined, there only exist four independent currents. Thus it is only possible to decide the value of four of the six power terms while the rest depend on the choice of the previous ones. In this situation it is common to choose to constraint the value of the three components of the active power, which have a direct effect in the evolution of the DC bus voltage, and the mean value of the reactive power. Usually the reference value for the sine components of the active power is set to be zero to avoid the ripple in the DC bus voltage. However, it can also be set to match another time-varying power input as described in [7]. The equations to solve for the power on the grid connection point of the converter are:

$$\begin{cases} P_{z0} &= \frac{3}{2} (v_{zq}^+ i_{lq}^+ + v_{zq}^- i_{lq}^-) \\ P_{z \cos} &= \frac{3}{2} (v_{zq}^+ i_{lq}^- + v_{zq}^- i_{lq}^+) \\ P_{z \sin} &= \frac{3}{2} (-v_{zq}^+ i_{ld}^- + v_{zq}^- i_{ld}^+) \\ Q_{z0} &= \frac{3}{2} (v_{zq}^+ i_{ld}^+ + v_{zq}^- i_{ld}^-) \end{cases} \quad (9.28)$$

Solving to obtain the reference current for a given active and reactive power reference, the following relation is obtained:

$$\begin{cases} i_{lq}^+ = \frac{2}{3} \left(\frac{v_{zq}^+}{(v_{zq}^+)^2 - (v_{zq}^-)^2} P_{z0}^* - \frac{v_{zq}^-}{(v_{zq}^+)^2 - (v_{zq}^-)^2} P_{z \cos} \right) \\ i_{ld}^+ = \frac{2}{3} \left(\frac{v_{zq}^+}{(v_{zq}^+)^2 + (v_{zq}^-)^2} Q_{z0}^* + \frac{v_{zq}^-}{(v_{zq}^+)^2 + (v_{zq}^-)^2} P_{z \sin} \right) \\ i_{lq}^- = \frac{2}{3} \left(-\frac{v_{zq}^-}{(v_{zq}^+)^2 - (v_{zq}^-)^2} P_{z0}^* + \frac{v_{zq}^+}{(v_{zq}^+)^2 - (v_{zq}^-)^2} P_{z \cos} \right) \\ i_{ld}^- = \frac{2}{3} \left(\frac{v_{zq}^-}{(v_{zq}^+)^2 + (v_{zq}^-)^2} Q_{z0}^* - \frac{v_{zq}^+}{(v_{zq}^+)^2 + (v_{zq}^-)^2} P_{z \sin} \right) \end{cases} \quad (9.29)$$

As in the balanced case, this calculation neglects the difference between the active power in the grid connection point of the converter and the actual active power output of the inverter. The active power on the inverter terminals can be written as a function of the active power output to the grid

Chapter 9 VSC reference calculation issues for unbalanced operation

as:

$$P_{l0} = P_{z0} + r_l \left((i_{lq}^+)^2 + (i_{ld}^+)^2 + (i_{lq}^-)^2 + (i_{ld}^-)^2 \right) \quad (9.30)$$

$$P_{l \cos} = P_{z \cos} + 3r_l \left(i_{lq}^+ i_{lq}^- + i_{ld}^+ i_{ld}^- \right) + 3\omega_e L_l \left(-i_{lq}^+ i_{ld}^- + i_{ld}^+ i_{lq}^- \right) \quad (9.31)$$

$$P_{l \sin} = P_{z \sin} - 3r_l \left(i_{lq}^+ i_{ld}^- - i_{ld}^+ i_{lq}^- \right) - 3\omega_e L_l \left(i_{lq}^+ i_{lq}^- + i_{ld}^+ i_{ld}^- \right) \quad (9.32)$$

Note that unlike the balanced case, the voltage drop in the inductor not only affects the mean value of the active power, which can be properly compensated by the DC bus voltage controller, but also affects the time-varying terms of the active power, which sometimes are controlled in a open loop way by setting them to be zero.

As it was suggested in the balanced case, one workaround for this problem is to iteratively solve for the current reference by correcting the active power reference value:

$$(i_{lq}^+)_{n+1} = \frac{2}{3} \frac{v_{zq}^+}{(v_{zq}^+)^2 - (v_{zq}^-)^2} (P_{z0}^*)_n - \frac{2}{3} \frac{v_{zq}^-}{(v_{zq}^+)^2 - (v_{zq}^-)^2} (P_{z \cos}^*)_n \quad (9.33)$$

$$(i_{ld}^+)_{n+1} = \frac{2}{3} \frac{v_{zq}^+}{(v_{zq}^+)^2 + (v_{zq}^-)^2} Q_{z0}^* + \frac{2}{3} \frac{v_{zq}^-}{(v_{zq}^+)^2 + (v_{zq}^-)^2} (P_{z \sin}^*)_n \quad (9.34)$$

$$(i_{lq}^-)_{n+1} = -\frac{2}{3} \frac{v_{zq}^-}{(v_{zq}^+)^2 - (v_{zq}^-)^2} (P_{z0}^*)_n + \frac{2}{3} \frac{v_{zq}^+}{(v_{zq}^+)^2 - (v_{zq}^-)^2} (P_{z \cos}^*)_n \quad (9.35)$$

$$(i_{ld}^-)_{n+1} = \frac{2}{3} \frac{v_{zq}^-}{(v_{zq}^+)^2 + (v_{zq}^-)^2} Q_{z0}^* - \frac{2}{3} \frac{v_{zq}^+}{(v_{zq}^+)^2 + (v_{zq}^-)^2} (P_{z \sin}^*)_n \quad (9.36)$$

where

$$(P_{z0}^*)_n = P_{l0}^* - r_l \left((i_{lq}^+)_n^2 + (i_{ld}^+)_n^2 + (i_{lq}^-)_n^2 + (i_{ld}^-)_n^2 \right) \quad (9.37)$$

$$(P_{z \cos}^*)_n = P_{l \cos}^* - 3r_l \left((i_{lq}^+)_n (i_{lq}^-)_n + (i_{ld}^+)_n (i_{ld}^-)_n \right) - 3\omega_e L_l \left(-(i_{lq}^+)_n (i_{ld}^-)_n + (i_{ld}^+)_n (i_{lq}^-)_n \right) \quad (9.38)$$

9.3 Analysis of the current reference calculation for unbalanced operation

$$(P_{z\sin}^*)_n = P_{l\sin}^* + 3r_l \left((i_{lq}^+)_n (i_{ld}^-)_n - (i_{ld}^+)_n (i_{lq}^-)_n \right) + 3\omega_e L_l \left((i_{lq}^+)_n (i_{lq}^-)_n + (i_{ld}^+)_n (i_{ld}^-)_n \right) \quad (9.39)$$

Finally, one important result from (9.29), whose implications have not been addressed in previous works is that there exists a discontinuity that causes the reference current to become infinite when $v_{zq}^+ = v_{zq}^-$ i.e. when the magnitude of the positive sequence of the voltage is equal to that of the negative sequence (there is no dominant voltage component). To analyze this particular situation, this condition is introduced in the equation of a unbalanced three phase signal (9.13) yielding:

$$v_z^{abc}(t) = 2A \begin{bmatrix} \cos(\frac{\varphi^+ - \varphi^-}{2}) \cos(\omega_e t + \frac{\varphi^+ + \varphi^-}{2}) \\ \cos(\frac{\varphi^+ - \varphi^-}{2} - \frac{2\pi}{3}) \cos(\omega_e t + \frac{\varphi^+ + \varphi^-}{2}) \\ \cos(\frac{\varphi^+ - \varphi^-}{2} + \frac{2\pi}{3}) \cos(\omega_e t + \frac{\varphi^+ + \varphi^-}{2}) \end{bmatrix} \quad (9.40)$$

where $A \triangleq \sqrt{2}V_z^+ = \sqrt{2}V_z^-$.

From this equation it can be seen that under such condition, each phase of v_z^{abc} become zero at the same time and it is not possible to get a constant power output from the converter without the need of an infinite current.

One possible solution to this problem would be to limit the result of (9.29) to a certain value by modulus. One important drawback of this solution is that in that case, it is not possible to assure that the resulting current reference will lead to the desired mean value of the active power, which is critical to maintain the desired mean value of the DC bus voltage.

A different approach based on combining two different reference calculation formulas is possible. The reference calculation expression (9.29) can be

Chapter 9 VSC reference calculation issues for unbalanced operation

rewritten as:

$$\left\{ \begin{array}{l} i_{lq}^+ = \frac{2}{3} \frac{1}{v_{zq}^+} \left(P_{z0}^* + \alpha \frac{\left(\frac{v_{zq}^-}{v_{zq}^+}\right)^2 P_{z0}^* - \frac{v_{zq}^-}{v_{zq}^+} P_{z \cos}^*}{1 - \left(\frac{v_{zq}^-}{v_{zq}^+}\right)^2} \right) \\ i_{ld}^+ = \frac{2}{3} \frac{1}{v_{zq}^+} \left(Q_{z0}^* + \alpha \frac{-\left(\frac{v_{zq}^-}{v_{zq}^+}\right)^2 Q_{z0}^* + \frac{v_{zq}^-}{v_{zq}^+} P_{z \sin}^*}{1 + \left(\frac{v_{zq}^-}{v_{zq}^+}\right)^2} \right) \\ i_{lq}^- = \frac{2}{3} \frac{\alpha}{v_{zq}^+} \left(P_{z \cos}^* + \frac{\left(\frac{v_{zq}^-}{v_{zq}^+}\right)^2 P_{z \cos}^* - \frac{v_{zq}^-}{v_{zq}^+} P_{z0}^*}{1 - \left(\frac{v_{zq}^-}{v_{zq}^+}\right)^2} \right) \\ i_{ld}^- = \frac{2}{3} \frac{\alpha}{v_{zq}^+} \left(-P_{z \sin}^* + \frac{\left(\frac{v_{zq}^-}{v_{zq}^+}\right)^2 P_{z \sin}^* + \frac{v_{zq}^-}{v_{zq}^+} Q_{z0}^*}{1 + \left(\frac{v_{zq}^-}{v_{zq}^+}\right)^2} \right) \end{array} \right. \quad (9.41)$$

where α is a parameter that allows switching between two different reference calculation methods. For $\alpha = 1$, (9.41) becomes equivalent to (9.29) whereas for $\alpha = 0$ the reference calculation formula becomes:

$$\left\{ \begin{array}{l} i_{lq}^+ = \frac{2}{3} \frac{1}{v_{zq}^+} P_{z0}^* \\ i_{ld}^+ = \frac{2}{3} \frac{1}{v_{zq}^+} Q_{z0}^* \\ i_{lq}^- = 0 \\ i_{ld}^- = 0 \end{array} \right. \quad (9.42)$$

This equation is equivalent to the one used for the conventional vector control meant for balanced operation, thus the references for the negative sequence current are zero. From (9.28) it can be seen that this produces the desired mean value for the active and the reactive power but does not allow to control the sine time-varying terms of the active power.

One important remark that can be made by comparing (9.42) and (9.29) is that in general in the case of existence of negative sequence voltages in the grid, the suppression of the active power oscillation by injecting negative current leads to a reduction of the mean value of the active power. This in turn leads to the need of a higher positive sequence current to maintain the mean value of the active power. Thus, in case of a voltage sag, where usually the maximum allowed current becomes an issue, (9.29) is more likely to have problem to extract the needed active power to maintain the desired DC bus voltage. On the other hand, as the effect of the power oscillation on the DC bus voltage is directly related to the capacitance of the DC-side capacitor

9.4 Simulation testing of the proposed reference calculation scheme

filter, this suggests that systems which use a DC-side capacitor filter with a small value of capacitance, which may be the standard practice in HVDC link systems, it may be necessary to overrate the current capability of the inverter to be able to compensate for the oscillations in case of a network unbalance.

9.4 Simulation testing of the proposed reference calculation scheme

In order to test the performance of the proposed control methods, a simulation of the response of the system to an unbalanced voltage sag is performed. The characteristic parameters of the simulated converter and the operation point for the simulation can be found in Table 9.1. The rating of the converter and its switching frequency the same as the grid-side inverter of the rotor converter of the 1 MW DFIG wind turbine in [44]. The machine-side inverter has been modeled as a constant power input of 300 kW with no ripple. Thus the power references for P_{sin} and P_{cos} will be set to zero to avoid a ripple in the DC bus voltage.

Parameter	Units	Value	Description
V_z^N	690	V	Grid nominal voltage
P_l^N	300	kW	Nominal active power
Q_z^N	100	kVAr	Nominal reactive power
V_{DC}^N	1338	V	DC bus nominal voltage
r_l	0.05	Ω	Grid connection filter resistance
L_l	27	mH	Grid connection filter inductance
f_s	3	kHz	Inverter switching frequency
T_i	50	ms	Current control settling time
T_{PLL}	20	ms	Grid voltage PLL settling time

Table 9.1: Characteristic parameters of the simulated scenario.

The response of the system to a unbalanced voltage sag is simulated using three different calculation methods (see Figure 9.1). The first one, referred as I, uses the formula presented in (9.41) for $\alpha = 0$, the second one, referred as II, uses the presented formula in (9.41) for $\alpha = 1$ plus the iterative compensation of the filter impedance and the third one, referred as III, uses the same formula as II but without compensating the filter impedance.

The simulated voltage sag corresponds to a two phase to ground sag which

Chapter 9 VSC reference calculation issues for unbalanced operation

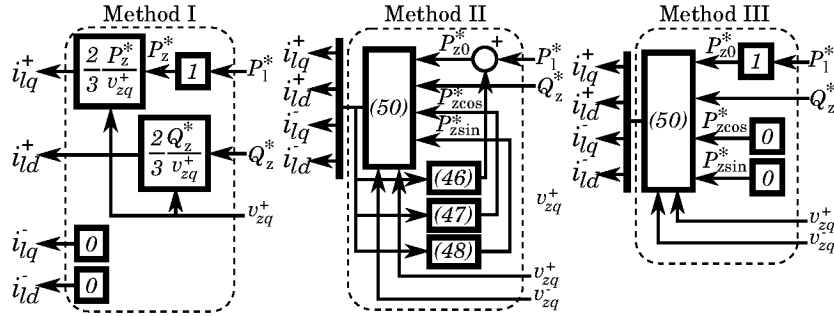


Figure 9.1: Current reference calculation methods.

causes the voltage of two of the phases to drop by a 65%. The waveform of the grid voltage seen by the inverter is shown in Figure 9.2 and the amplitude of the positive and negative sequence as measured by the phase locked loop (PLL) used by the controller is shown in Figure 9.3. Note this sag causes the positive sequence of the voltage to reduce to 0.36 pu and the negative sequence to appear with an amplitude of 0.30 pu, thus the ratio between the positive and the negative sequence amplitudes is 1.2 which is close to 1.0 which is the limit of the II and III methods.

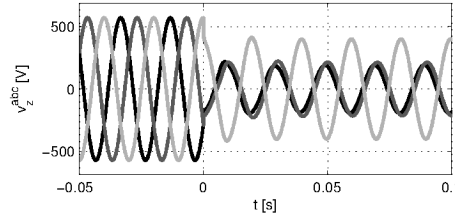


Figure 9.2: Voltage at the PCC of the converter.

The controller used in the simulation model uses the double synchronous reference frame (DSRF) current controller described in [7] and a PLL for unbalanced voltages described in [45]. The performance specifications for both parts of the controller can be found in Table 9.1.

Figure 9.4 shows the evolution of the voltage during the sag. Notice that the initial transient is the same for all the methods as expected but the steady state differs. Methods I and III produce a significant steady state ripple, the reason for that is that method I does not use negative sequence and method III does not compensate the difference between the power on the grid connection point and the power on the inverter terminals. This can

9.5 Experimental testing of the proposed reference calculation scheme

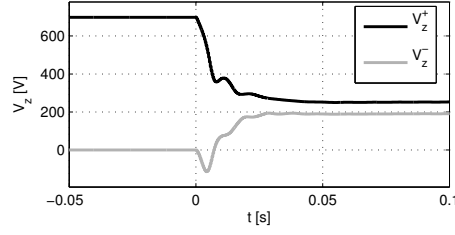


Figure 9.3: Amplitude of the positive and negative sequence of the voltage at the PCC measured by the PLL.

further be confirmed by plotting P_l and P_z (Figure 9.5). Notice that method III allows to suppress the ripple in P_z but causes an important ripple in P_l which makes the DC bus voltage to have a larger oscillation than method I.

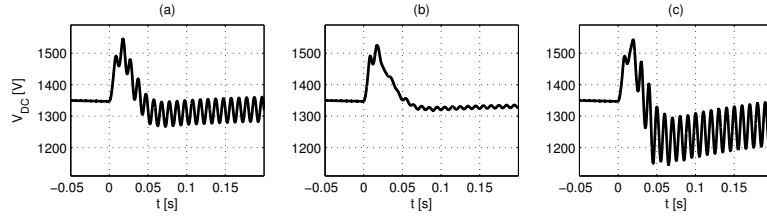


Figure 9.4: Comparison of the evolution of the DC bus voltage using I (a), II (b) and III (c) current reference calculation methods.

The evolution of the current is shown in Figure 9.6. Note that all methods require an increase of the current due to the reduction of the voltage and as noted before methods II and III require more current than I even though the oscillation in III is larger than in I.

9.5 Experimental testing of the proposed reference calculation scheme

In order to further verify the theoretical results, a test of the analyzed current reference calculation schemes is performed on an experimental platform. The test platform consists of two CDM2480 [46] low power voltage source three phase inverters fed by two independent 24V DC buses and connected by the AC side through a three phase inductor ($r = 0.1 \Omega$, $L = 4.9 \text{ mH}$). One of the inverters, referred as the generator grid side inverter, is used to emulate

Chapter 9 VSC reference calculation issues for unbalanced operation

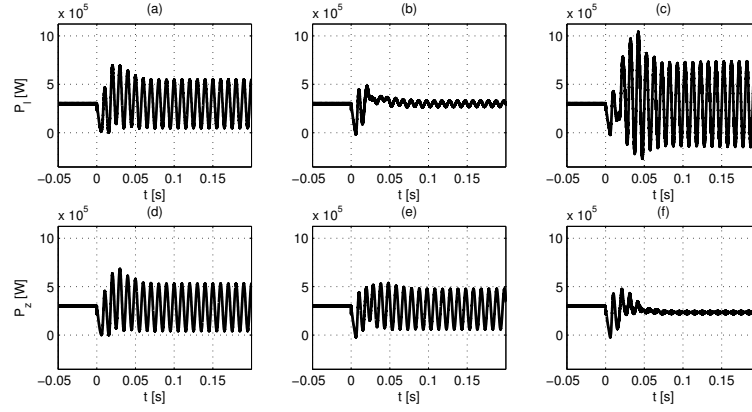


Figure 9.5: Comparison of the evolution of the converter output power measured on the inverter versus the power measured on the PCC using I (a,d), II (b,e) and III (c,f) current reference calculation methods.

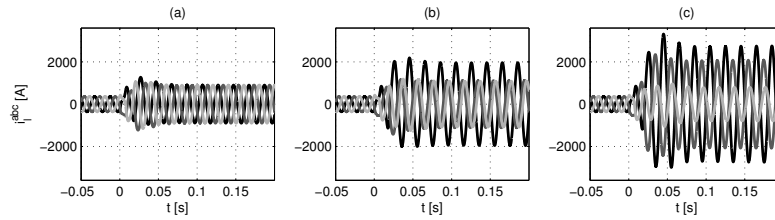


Figure 9.6: Comparison of the output current of the converter using I (a), II (b) and III (c) current reference calculation methods.

9.5 Experimental testing of the proposed reference calculation scheme

the grid side inverter of a grid connected power source and inject power from its DC bus to the other inverter, referred as the grid emulator, used to emulate the behaviour of the grid. A picture and a diagram of the different parts of the experimental setup can be seen in Figure 9.7. The voltage of the terminals of the generator side inverter and the grid emulator and the current flowing through the inductors are measured and recorded using a data acquisition device.

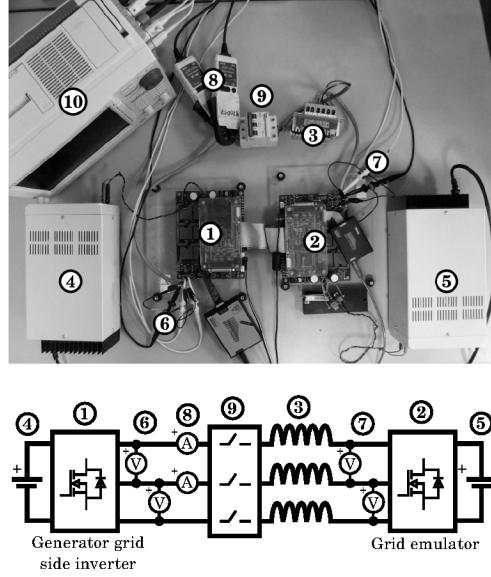


Figure 9.7: Picture and schematics of the experimental setup. (1) generator grid-side inverter, (2) grid emulator, (3) converter inductances, (4) generator-side DC power source, (5) grid emulator DC power source and load, (6) generator grid-side inverter voltage v_l^{abc} measurement, (7) grid emulator voltage v_z^{abc} measurement, (8) generator grid-side output current i_l^{abc} measurement, (9) grid connection switch, (10) data acquisition device.

Each inverter is controlled by a TMS320F2812 eZdsp™ control board which have been programmed for the test. The grid emulator inverter is programmed to apply three phase voltage waveforms on its AC side corresponding to those of the two phase fault used in the simulations in the previous section whilst the current flowing thorough the generator side inverter is controlled using a DSRF current controller as in the simulated scenario of the previous section.

Chapter 9 VSC reference calculation issues for unbalanced operation

Three different tests of the response of the system under the same unbalanced voltage sag are performed on the experimental platform using a different current reference calculation method each time. The evolution of the grid voltage, the current and the active power flowing through the converter and the active power injected to the grid for each scheme can be seen in Figures 9.8, 9.9 and 9.10. It can be seen that the voltage sag requires an increase of the current to keep the same average power output from the converter in any case. In the case of method I, which only injects positive sequence current, the increase is smaller and symmetrical for each phase, whereas methods II and III require asymmetrical currents which are higher in, at least, one of the phases. Regarding the power ripple, method I produces an important ripple both in the power injected to the grid and the converter output. Method III is able to compensate the ripple in the power injected to the grid but produces a higher ripple in the converter output power. By compensating the effect of the inductor impedance, method II is able to suppress that ripple but then produces a ripple in the power injected to the grid.

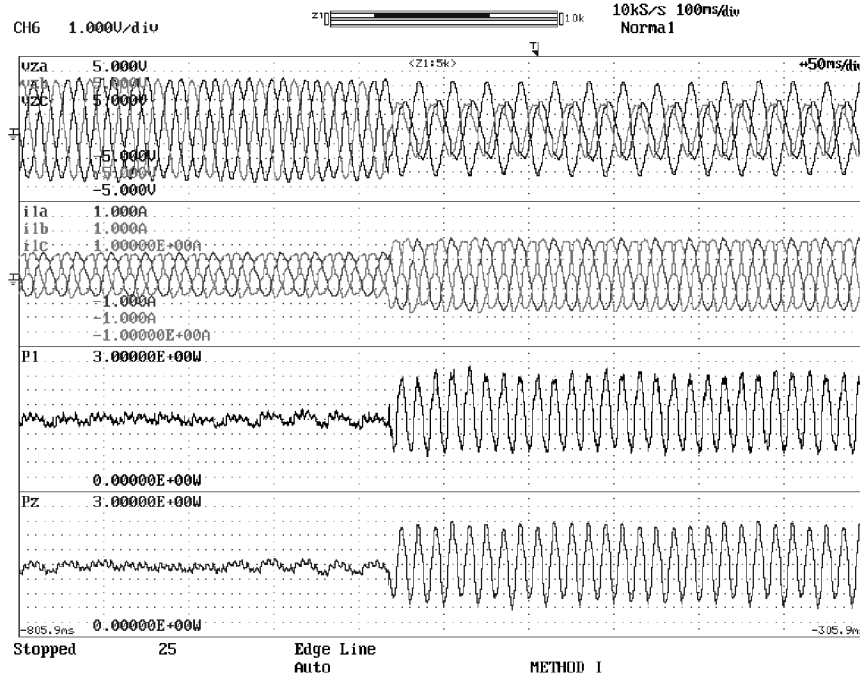


Figure 9.8: Experimental results for method I. From top to bottom: v_z^{abc} , i_l^{abc} , P_l and P_z .

9.6 Conclusions

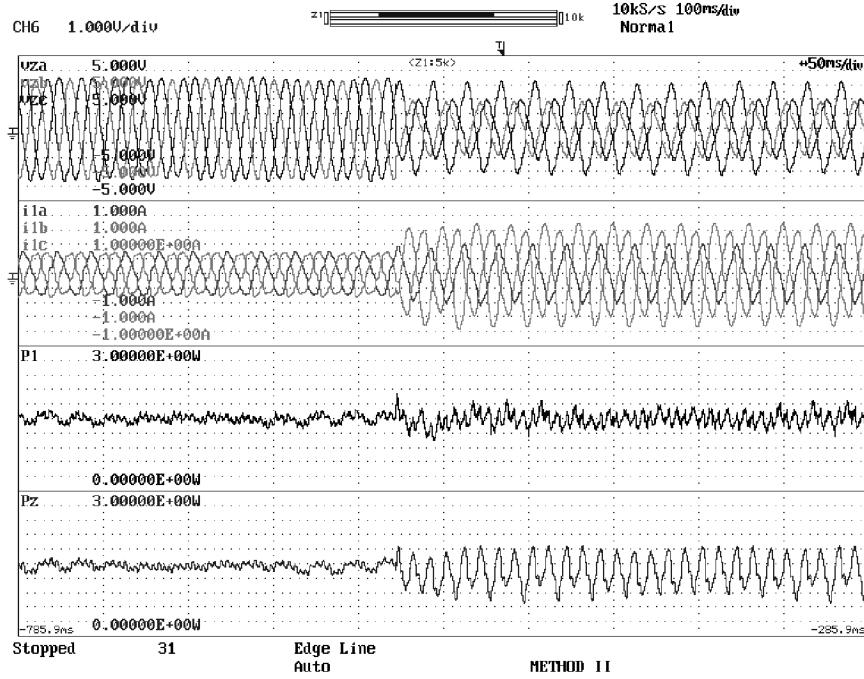


Figure 9.9: Experimental results for method II. From top to bottom: v_z^{abc} , i_l^{abc} , P_l and P_z .

9.6 Conclusions

The injection of negative sequence currents have been shown to allow to suppress the oscillation on the DC bus voltage due to the oscillation of the power injected to the grid during a unbalanced voltage sag. However, compared to the standard method of injecting only positive sequence current, this method have been found to require larger currents to maintain the same level of average active power. For deep voltage sags, this may lead to even higher oscillations of the DC bus voltage if the effect of the AC filter impedance on the converter power output is not properly compensated and a method has been proposed to do it. Also, a special condition has been identified which makes it impossible to control the oscillating terms of the active power and a solution for the calculation of the current references in that case has been proposed.

Chapter 9 VSC reference calculation issues for unbalanced operation

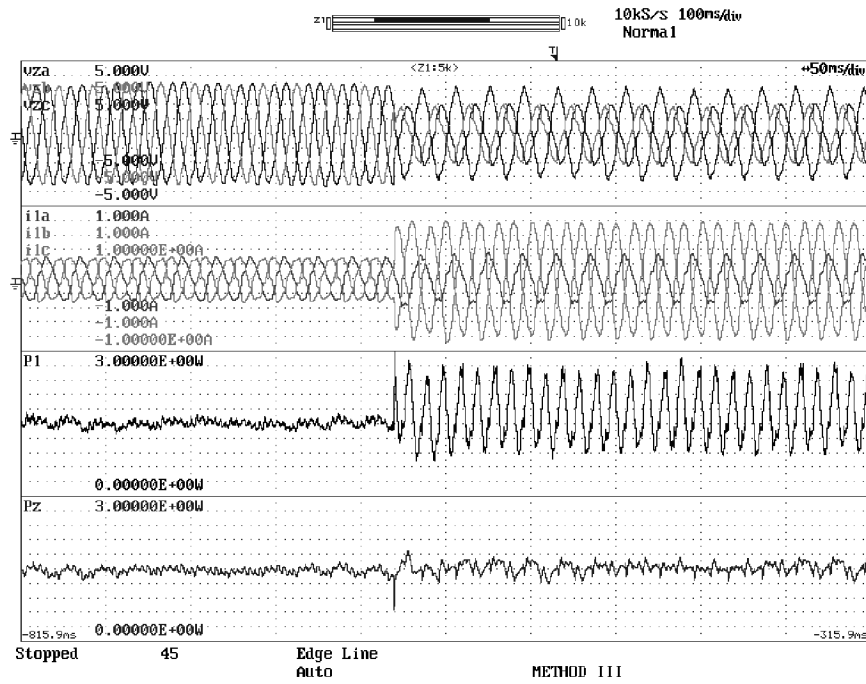


Figure 9.10: Experimental results for method III. From top to bottom: v_z^{abc} , i_l^{abc} , P_l and P_z .

Chapter 10

PMSG vector control

10.1 Introduction

This chapter analyzes the use of a vector control design for the current control of PMSG-based WTGS.

As the PMSG is isolated from the grid by the converter and the machine impedances can arguably be considered to be balanced, here there is no need to use the extensions of the vector control for unbalanced operation.

The control of the AC grid side of the converter of the PMSG is not presented in this chapter because the topology of the converter for this type of WTGS is equivalent to that of a DFIG wind turbine and can be controlled using the same the current control designs described in the previous chapters.

Section 10.2 describes the design of a vector current control of the PMSG. This control scheme will be used later in Chapter 11 in the simulation models and in the controller of the experimental system used to study a ride-through strategy for this type of WTGS.

10.2 Machine side control

From Chapter 4, we know that the relation between the voltage and the current in a permanent magnet synchronous machine can be written as:

$$v_s^{qd} = \begin{bmatrix} r_s & \omega_r (L_{ls} + \frac{3}{2} (L_A + L_B)) \\ -\omega_r (L_{ls} + \frac{3}{2} (L_A - L_B)) & r_s \end{bmatrix} i_s^{qd} + \begin{bmatrix} L_{ls} + \frac{3}{2} (L_A - L_B) & 0 \\ 0 & L_{ls} + \frac{3}{2} (L_A + L_B) \end{bmatrix} \frac{d}{dt} i_s^{qd} + \lambda_m \omega_r \begin{bmatrix} 1 \\ 0 \end{bmatrix} \quad (10.1)$$

From these equations, it can be seen that the q and d variables are coupled and the dynamic behavior of the current depends on the mechanical speed of the machine. In order to simplify the design of the current controller, a

Chapter 10 PMSG vector control

decoupling feedback is used which both decouples the q and d component and eliminates the dependency on the mechanical speed of the machine, thus eliminating a non-linearity of the dynamics [47]. To do that, a voltage is applied on the stator of the machine which compensates the coupling terms. This voltage can be written as:

$$\begin{Bmatrix} v_{sq} \\ v_{sd} \end{Bmatrix} = \begin{Bmatrix} \hat{v}_{sq} + \omega_r L_d i_{sd} + \lambda_m \omega_r \\ \hat{v}_{sd} - \omega_r L_q i_{sq} \end{Bmatrix} \quad (10.2)$$

where \hat{v}_{sq} and \hat{v}_{sd} are the control outputs of a linear current controller.

Assuming the compensation to be perfect, the dynamics become:

$$\hat{v}_s^{qd} = \begin{bmatrix} r_s & 0 \\ 0 & r_s \end{bmatrix} i_s^{qd} + \begin{bmatrix} L_q & 0 \\ 0 & L_d \end{bmatrix} \frac{d}{dt} i_s^{qd} \quad (10.3)$$

Note that these equations no longer depend on the mechanical speed and are decoupled. Thus, they can be split as two different systems for q and d . Applying the Laplace transform to these, the following transfer functions can be obtained:

$$\frac{i_{sq}}{\hat{v}_{sq}}(s) = \frac{1}{L_q s + r_s} \quad (10.4)$$

and

$$\frac{i_{sd}}{\hat{v}_{sd}}(s) = \frac{1}{L_d s + r_s} \quad (10.5)$$

One possible way of designing the current controllers which has been successfully used in the past is the so called IMC [29], where the controller transfer function is contain the inverse of the plant dynamics plus the desired open loop transfer function to obtain the desired closed loop dynamics.

Here, the pole of the system is suppressed by putting a matching zero in the controller transfer function plus an integrator so that the steady state error for step reference inputs is zero and the controller is causal. The closed loop transfer function becomes:

$$\begin{Bmatrix} i_{sq}(s) \\ i_{sd}(s) \end{Bmatrix} = \begin{bmatrix} \frac{1}{\alpha s + 1} & 0 \\ 0 & \frac{1}{\alpha s + 1} \end{bmatrix} \begin{Bmatrix} i_{sq}^*(s) \\ i_{sd}^*(s) \end{Bmatrix} \quad (10.6)$$

The controller transfer function corresponds to that of a PI controller with the transfer function:

$$K(s) = \frac{K_p s + K_i}{s} \quad (10.7)$$

10.2 Machine side control

where

$$\left. \begin{aligned} K_p &= \alpha L_q \\ K_i &= \alpha r_s \end{aligned} \right\} \quad (10.8)$$

and α is a design parameter which is proportional to the bandwidth of the system.

A wide bandwidth will result in a fast response, which is a desirable feature, but in turns makes the system more sensible to feedback measurement noise and will require a higher bandwidth of the control action. Note that when studying the system, an averaged model was used for the converter by neglecting its switching nature due to the use of a high frequency pulse width modulation and the assumption that the controller output was a low pass signal. A high bandwidth of the control action make these assumptions to be false, thus a balance between a fast controller response and a low bandwidth of the control action is needed for a proper design of the controller.

10.2.1 Discrete time implementation of the controller

For the sake of simplicity, the previous section describes a continuous time design of the system controller even though the real implementation of the controller must be done in a digital discrete time system. An approximation of the effect of the time discretization can be taken into account in the design of the controller by the addition of non minimum phase zeros to the open loop transfer function. Such approximation will be used here by using the so called bilinear transform to obtain a continuous time transfer function of the plant. To avoid the redundancy, as the q and d variables exhibit equivalent dynamics, only the results for q are shown.

A discrete time controller with a T sampling time and a zero order hold will be considered. In this case, the transfer function in z can be obtained for i_{sq} as a function of v_{sq} from the continuous time transfer function of the system (10.4)) as:

$$\frac{i_{sq}}{\hat{v}_{sq}}(z) = \frac{\frac{1}{r_s} \left(1 - e^{-\frac{r_s}{L_q} T}\right)}{z - e^{-\frac{r_s}{L_q} T}} \quad (10.9)$$

The bilinear transformation maps the z plane to the so called w plane, it is defined as:

$$w \triangleq \frac{2}{T} \frac{z - 1}{z + 1} \quad (10.10)$$

Chapter 10 PMSG vector control

By introducing the bilinear transformation to the previous transfer function, we obtain:

$$\frac{i_{sq}}{\hat{v}_{sq}}(w) = \frac{\frac{1}{r_s} \left(-\frac{T}{2}w + 1 \right)}{\frac{T}{2} \left(\frac{1+e^{-\frac{r_s T}{L_q}}}{1-e^{-\frac{r_s T}{L_q}}} \right) w + 1} \quad (10.11)$$

By comparing this transfer function to the transfer function of the plant without the zero order hold, it can be seen that a non minimum phase zero has been added at $2/T$ due to the time discretization. The existence of this zero puts an approximate upper bound to the bandwidth of the system at $1/T$ [32]. As the sampling frequency is usually chosen to match the frequency of the pulse width modulation used to trigger the switching devices of the converter and it is usually technology limitation, this sets an upper bound to the performance that can be obtained from the system.

On the other hand, the existence of a non minimum phase zero, also called unstable zero, makes it impossible to invert the plant dynamics in the controller in order to keep the system internally stable. Thus, the zero must be either kept or approximately compensated. Here, the zero is kept and the pole of the system is suppressed the same way as in the continuous time design by using a PI controller defined in w using the following parameters:

$$\left. \begin{aligned} K_p &= \alpha \frac{T}{2} \left(\frac{1+e^{-\frac{r_s T}{L_q}}}{1-e^{-\frac{r_s T}{L_q}}} \right) r_s \\ K_i &= \alpha r_s \end{aligned} \right\} \quad (10.12)$$

Note that for small sampling times, as $T \rightarrow 0$, K_p tends to αL_q which is the K_p parameter of the continuous time design in (10.8)).

The transfer function of the PI in w is:

$$G_c(s) = \frac{K_p w + K_i}{w} \quad (10.13)$$

By inverting the bilinear transformation, the corresponding transfer function in z is obtained:

$$G_c(z) = \frac{\left(K_p + \frac{T}{2} K_i \right) \left(z + \frac{-K_p + \frac{T}{2} K_i}{K_p + \frac{T}{2} K_i} \right)}{z - 1} \quad (10.14)$$

Chapter 11

Voltage sag ride-through of PMSG wind turbines using droop control

11.1 Introduction

Voltage sags are reductions of the voltage amplitude. These are the most common type of grid disturbances and they can be caused by short-circuits, overloads and starting transients of large machines [36]. WTGS are known to be very sensible to voltage sags as wind farms are usually installed on far locations leading to high network impedance and thus weak network connections. In the last decade the need for the WTGS to stay connected during this type of faults using the so called ride-through strategies have increased due to the rising penetration of wind farms on the network [4, 48].

Here a new strategy based on droop control is introduced which makes it possible to ride through voltage sags without the use of the so called DC bus chopper resistor by reducing the power extracted from the wind by the generator in case of a grid fault. This strategy also enables the independent control of the grid connection inverter and the generator rectifier and increases the robustness in case of communication failure between the control system of both sides of the back-to-back converter allowing to place both sides in different locations far from each other. Also, even though here a PMSM wind turbine with full power converter will be considered, the same procedure can be easily extended to other topologies of wind generators connected to the grid through full power converters.

11.2 Problem formulation

The power injected to the grid by the grid side inverter of a wind turbine, P_z , depends on the grid phase-to-neutral voltage V_z and the inverter output current I_l as: $P_z = 3V_z I_l \cos(\phi)$, where ϕ is the angle between the voltage and the current. Assuming a the efficiency of the inverter to be constant, P_z

Chapter 11 Voltage sag ride-through of PMSG wind turbines using droop control

can be considered to be proportional to the power extracted by the inverter from the DC bus, P_{DCI} :

$$P_z = \eta_l P_{DCI} \quad (11.1)$$

where η_l is the approximate efficiency of the inverter plus the filter. The different stages of the power conversion are depicted in Figure 11.1.

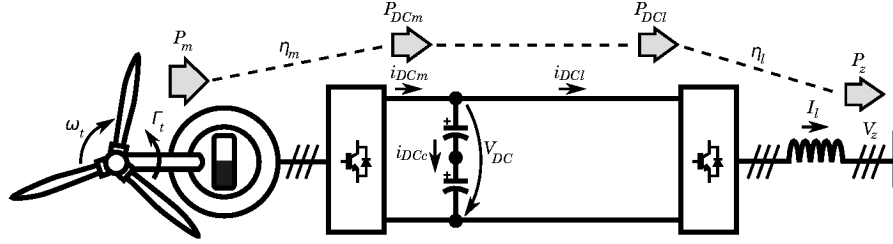


Figure 11.1: PMSG wind turbine with full power converter.

During a voltage sag, V_z is reduced. Therefore the voltage applied by the inverter, V_l , is also reduced and the current flowing through the grid side, I_l , must be increased in order to maintain the same power output. As voltage source converters (VSC) work in boost mode, there is no problem in reducing V_l . However, I_l is usually the limiting factor which makes the converter unable to output the desired power when the operating point before the fault is close to the rated power. Under such condition, a strategy to reduce the power injected to the DC bus by the machine rectifier is needed to avoid the DC bus voltage to increase due to the power imbalance.

The mechanical power extracted by the electric generator P_m depends on the torque and the turbine speed, ω_t , as: $P_m = \Gamma_t \omega_t$. Assuming the efficiency of the generator plus the machine rectifier to be constant, this power can be considered to be related to the power injected by the rectifier into the DC bus, P_{DCI} , through:

$$P_{DCm} = \eta_m P_m \quad (11.2)$$

where η_m is the efficiency of the generator plus the machine rectifier. Thus, when both sides of the back-to-back converter are controlled together, the desired power reduction can be achieved by simply reducing the torque reference value, Γ_t^* , of the generator control loops when the grid fault is detected.

The actual torque applied by the generator and the reference torque signal are related through the generator current control dynamics which will be approximated as a first order system with a time constant τ_e and zero steady

11.3 Generator control strategy formulation

state error:

$$\Gamma_t = \frac{1}{\tau_{es} + 1} \Gamma_t^* \quad (11.3)$$

Fast changes in the torque of the generator are possible due to the fast dynamics of the generator current control loops, while the turbine speed ω_t varies slowly due to the high inertia and the slow mechanical dynamics of the turbine. Thus, for short duration faults, the machine speed can arguably be considered to be constant and it is possible to rapidly reduce the power injected to the DC bus by the rectifier using this procedure.

In case the converter is split and the sides of the back-to-back are far from each other, it might not be possible or not desirable to reduce the torque reference signal from the grid side inverter control. In such case, a different strategy avoiding the need to communicate the controllers from both sides is preferred. This can be achieved by using the DC bus voltage value to trigger a power reduction in the machine side control.

11.3 Generator control strategy formulation

According to [22], optimal power extraction from the wind is achieved by using the so called constant tip-speed ratio control, which is a open loop speed control strategy which applies a generator torque Γ_t proportional to the square of the turbine speed ω_t as:

$$\Gamma_t^* = K_{C_P} \omega_t^2 \quad (11.4)$$

where K_{C_P} is a parameter which depends on the geometry of the wind wheel.

The reference torque Γ_t^* must be modified by the generator control in order to reduce the power extraction in case of need to limit the power input from the generator to the DC bus. This can be achieved by using the so called droop control which commands a power reduction proportional to the error of a measured variable which is inversely proportional to the power input. This technique has been successfully applied for the power regulation of AC grids using the frequency as the measured variable, as a small decrease in the load consumption diminishes the torque of the synchronous generators and makes them accelerate. In the case of the DC bus of the power converter of a grid connected power source, the DC bus voltage can be used as the trigger variable as a decrease in the power injected to the AC grid produces a power imbalance which makes the DC bus voltage to rise.

The equation of the torque reference becomes:

$$\Gamma_t^* = K_{C_P} \omega_t^2 - K_{droop} (V_{DC} - V_{DC}^*) \quad (11.5)$$

Chapter 11 Voltage sag ride-through of PMSG wind turbines using droop control

where V_{DC} and V_{DC}^* are the DC bus actual voltage and its reference value and K_{droop} is the so called droop constant. This working principle is depicted in Figure 11.2 where two different operating points 1 and 2 are depicted along with the corresponding steady states 1' and 2' for a generic voltage sag. Notice from Figure 11.2(a) that the maximum allowed power output of the converter diminishes linearly with the grid voltage. Thus, for a V_z^{fault} voltage lower than the grid nominal voltage V_z^N , the maximum power output becomes P_z^{fault} hence producing an imbalance, P_z^{1err} and P_z^{2err} , between the power output to the grid and the power input from the generator to the DC bus which produces a rise in the DC bus voltage. As the power input is reduced according to (11.5) in a proportional manner to the voltage error, the system tends to a state where the power input from the generator equals the maximum allowed power output as depicted in Figure 11.2(b).

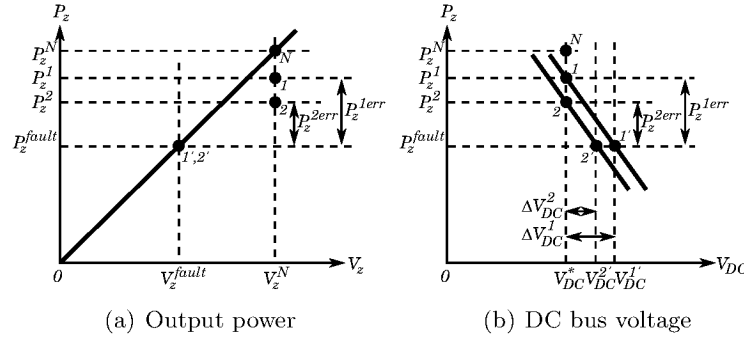


Figure 11.2: Droop control ride-through steady state.

11.4 Power reduction controller analysis and design

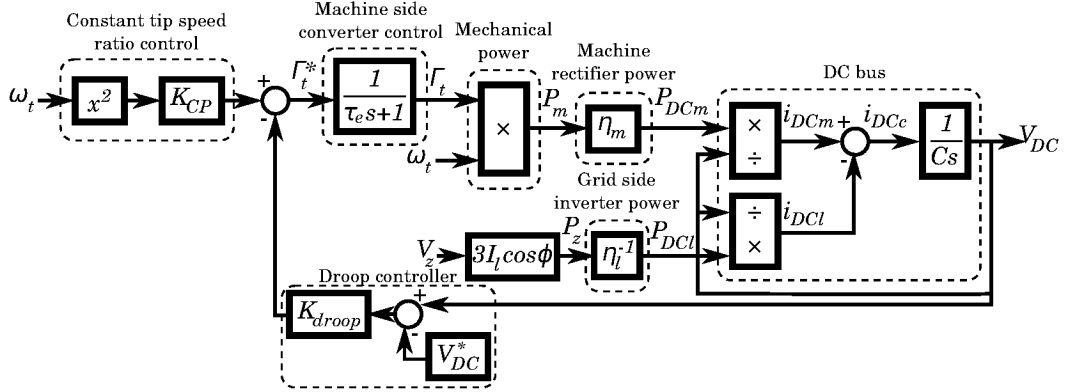
In order to obtain a procedure to design the droop constant from a performance specification, a dynamic model of the system must be obtained.

The DC bus is considered to have an equivalent capacitor C connected in parallel with the machine rectifier and the grid side inverter (Figure 11.1). The equation of the voltage of the DC bus is:

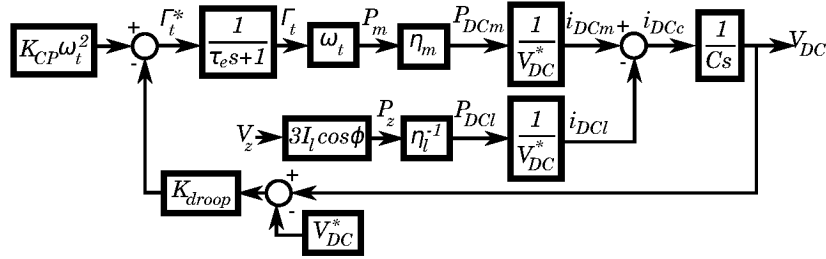
$$\frac{d}{dt}V_{DC} = \frac{1}{C}i_{DCc} = \frac{1}{C}(i_{DCm} - i_{DCI}) \quad (11.6)$$

where i_{DCc} is the current flowing through the capacitor, i_{DCm} is the current coming from the machine rectifier into the DC bus and i_{DCI} is the current

11.4 Power reduction controller analysis and design



(a) Non linear model



(b) Linearized model

Figure 11.3: Block diagrams of the DC bus dynamics.

going to the grid side inverter from the DC bus. i_{DCm} and i_{DCl} are related to P_{DCm} and P_{DCl} through: $P_{DCm} = V_{DC}i_{DCm}$ and $P_{DCl} = V_{DC}i_{DCl}$.

Combining the relations between the different magnitudes, a block diagram of the whole system shown in Figure 11.3(a) can be obtained. Note that the diagram contains several multiplications and divisions between system variables, thus the system is nonlinear. However, if the turbine speed is considered to be constant due to the short duration of the fault and the DC bus voltage is considered to be arguably close to its rated value V_{DC}^* , a linearization can be applied to the system in order to be able to use the well known linear system analysis tools to study its characteristics. The resulting diagram is shown in Figure 11.3(b).

In order to study the dynamics of the system in case of a voltage sag, a transfer function between the variation in the grid voltage, ΔV_z , and the variation of the DC bus voltage, ΔV_{DC} , can be easily obtained from the

Chapter 11 Voltage sag ride-through of PMSG wind turbines using droop control

linearized system:

$$\Delta V_{DC}(s) = -\frac{3I_l \cos(\phi)}{\eta_l} \frac{\tau_e s + 1}{\tau_e V_{DC} C s^2 + V_{DC} C s + \eta_m K_{droop} \omega_t} \Delta V_z(s) \quad (11.7)$$

From this transfer function, the steady state increase of the DC bus voltage for a given grid voltage drop can be easily obtained by applying the final value theorem:

$$\lim_{t \rightarrow \infty} \Delta V_{DC}(t) = \lim_{s \rightarrow 0} \Delta V_{DC}(s) = \frac{3I_l \cos(\phi)}{\eta_l} \frac{1}{\eta_m K_{droop} \omega_t} (V_z^N - V_z^{fault}) \quad (11.8)$$

where V_z^{fault} is the phase-to-neutral voltage during the fault and V_z^N is its rated value. Note that the steady state error of the voltage is proportional to the voltage drop and inversely proportional to the droop constant.

As the maximum allowed voltage of the DC bus is a technology limitation due to the maximum allowed voltage of the switching devices and the capacitor of the DC bus, one possible design criterion would be to choose K_{droop} to have a given voltage error for a given voltage sag depth and an operating speed:

$$K_{droop} = \frac{3I_l \cos(\phi)}{\eta_l \eta_m \omega_t} \frac{V_z^N - V_z^{fault}}{\Delta V_{DC}} \quad (11.9)$$

Regarding the dynamical behavior of V_{DC} , notice that (11.7) is a second order system with a stable zero and two poles which depend on the system parameters. As τ_e is likely to be small, it can be arguably approximated as $\tau_e \approx 0$ to simplify the understanding of the dynamics:

$$\Delta V_{DC}(s) \approx -\frac{3I_l \cos(\phi)}{\eta_l} \frac{\frac{1}{\eta_m K_{droop} \omega_t}}{\frac{V_{DC} C}{\eta_m K_{droop} \omega_t} s + 1} \Delta V_z(s) \quad (11.10)$$

By considering the generator current control loops to be very fast compared to the dynamics of the DC bus, the dynamics of the voltage become those of a first order system with a time constant τ_{DC} which can be calculated as:

$$\tau_{DC} = \frac{V_{DC} C}{\eta_m K_{droop} \omega_t} \quad (11.11)$$

Thus, the droop constant could also be set to have a desired settlement time ($t_{set} = 3\tau_{DC}$):

$$K_{droop} = \frac{3V_{DC} C}{\eta_m t_{set} \omega_t} \quad (11.12)$$

11.5 Simulation testing of the proposed scheme

Two possible design criteria to choose K_{droop} have already been shown, the one based in a specification of the maximum allowed increase in the DC bus voltage being the preferred one, as it is more likely to be a critical limitation of the system. It has also been shown that both criteria are not contradictory. Indeed, a high droop constant will produce a small steady state error and also a fast response, which are both desired features of the control.

11.5 Simulation testing of the proposed scheme

In order to test the performance of the proposed control scheme, two simulations of the system behaviour under different conditions are performed. The characteristic parameters of the system can be found in Table 11.1, note that they have been chosen to match those of the scale experimental platform which will be used in the next section to test a real implementation of the proposed control scheme.

The first simulated scenario is a symmetrical sudden 50% drop of the grid voltage (see Figure 11.4). The droop controller constant $K_{droop} = 0.21$ Nm/V is calculated from (11.9) so that for a voltage drop of 50% while extracting 1 kW at 2.000 min^{-1} , the voltage error is approximately 10 V. According to (11.11), this in turn would imply that the time constant of the voltage dynamics would be $\tau_{DC} = 26$ ms. As this value is very close to the current dynamics time constant ($\tau_e = 20$ ms), it is clear that the current control dynamics can not be neglected. Taking the non simplified second order system in (11.7), it can be seen that the poles of the system have a natural frequency $\omega_0 = 43.24$ rad/s and a damping coefficient $\zeta = 0.58$, which corresponds to an underdamped response with a settling time of $t_{set} = 120$ ms. The response of the system can be seen in Figure 11.4, notice that the transient response of the DC bus voltage corresponds to the predicted one and the system is able to adapt the power extracted from the mechanical system to match the power injected to the grid by the grid side inverter while keeping the DC bus voltage in the specified range.

The second simulated scenario corresponds to a dampened 50% voltage sag with a settling time of $t_{sag} = 500$ ms applied to the same system used in the first simulation scenario. The purpose of this simulation is to simulate the response of the system to the type of voltage sag that can be applied in the experimental setup. The response of the system is shown in Figure 11.5. Notice that as the evolution of the grid voltage is slow compared to the DC bus voltage dynamics, they can arguably be neglected, thus the transient

Chapter 11 Voltage sag ride-through of PMSG wind turbines using droop control

Parameter description	Symbol	Value	Units
Nominal grid voltage	U_z^N	230	V rms ph-ph
Nominal power factor	$\cos(\phi)$	1	1
Nominal active power	P_z^N	1	kW
Current control time constant	τ_e	20	ms
Power during the sag	P_z^{fault}	500	W
Nominal DC voltage	V_{DC}^N	490	V

Table 11.1: Simulated scenario parameters

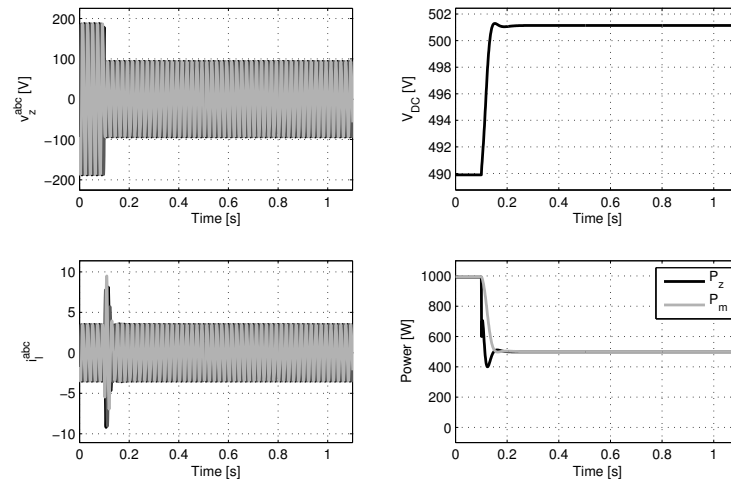


Figure 11.4: Simulation results for a sudden drop of the grid voltage.

11.6 Experimental results

evolution of the DC bus voltage matches the evolution of the grid voltage.

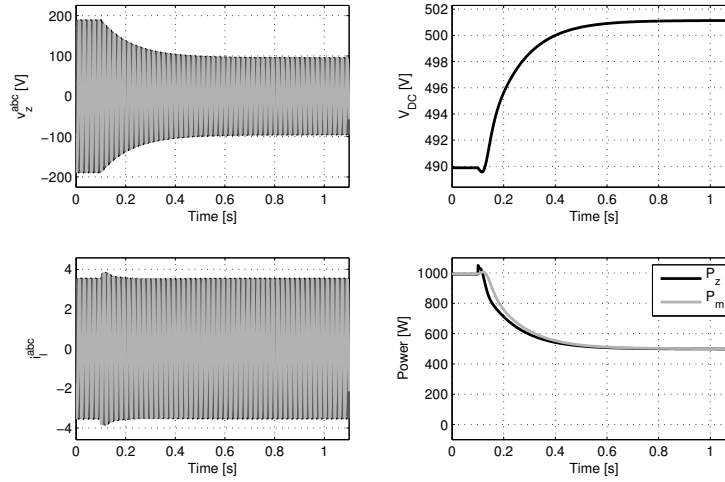


Figure 11.5: Simulation results for a dampened drop in the grid voltage.

11.6 Experimental results

To further test the performance of the proposed control law, a voltage sag test on a real platform controlled by an implementation of the proposed scheme has been performed. The platform setup is depicted in Figure 11.6. The setup consists of a back-to-back VSC converter connected to a PMSM used as the WTGS generator connected by the shaft to an identical PMSM machine which is used to emulate the wind turbine. A motor drive converter fed by a diode rectifier is used to power the turbine emulator machine. A three phase autotransformer is used to connect the back-to-back converter in order to be able to decrease the voltage seen by the converter to simulate a voltage sag[49]. A picture of the whole setup can be seen in Figure 11.7. The parameters of the system were used in the simulation model of the previous section and can be found in Table 11.1. The droop controller constant K_{droop} used in the real implementation is identical to the one designed for the simulation model.

A 50% voltage sag is applied to the converter while working on its nominal operating point. An oscilloscope capture of the most significant magnitudes

Chapter 11 Voltage sag ride-through of PMSG wind turbines using droop control

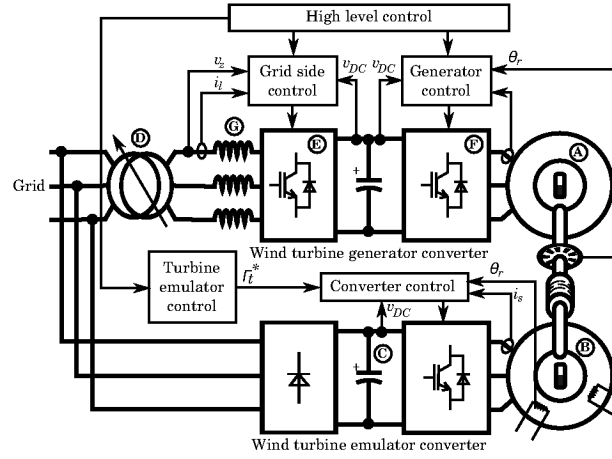


Figure 11.6: WTGS emulator setup

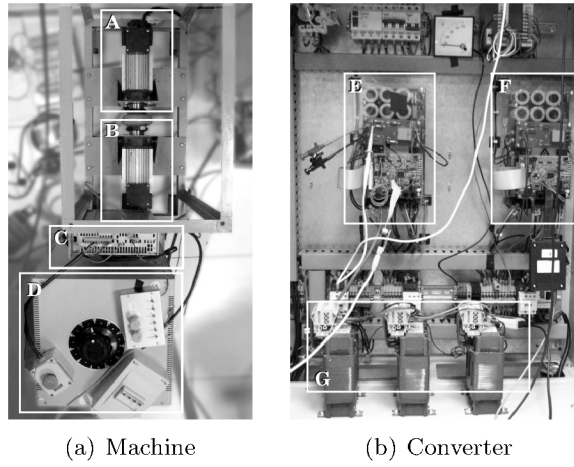


Figure 11.7: Picture of the real WTGS emulator setup. (A) PMSG generator, (B) PMSM turbine emulator, (C) Turbine emulator converter, (D) grid connection autotransformer, (E) grid side inverter, (F) generator side rectifier, (G) grid connection inductance.

11.6 Experimental results

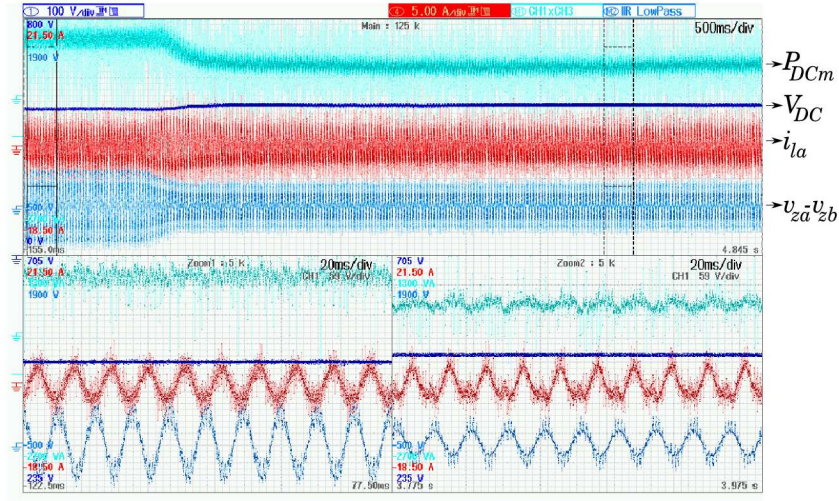


Figure 11.8: Oscilloscope capture of the voltage sag test. *Cyan* P_{DCm} power flowing to DC bus from the machine rectifier, *dark blue* DC bus voltage, *red* AC grid side current, *blue* grid voltage.

is plotted in Figure 11.8. During the fault, the current injected to the grid is kept constant as the current limitation has been set to match the nominal operating point. As the grid voltage is reduced, the power injected to the grid is reduced. The imbalance between the input and the output power of the DC bus makes the DC bus voltage to rise. The rise of the DC bus voltage triggers a reduction of the torque of the machine which reduces the power injected to the DC bus by the machine rectifier so that it matches the power injected to the grid and the system reaches a stable state where the DC bus voltage is kept constant. From the measurements it can be seen that the steady state DC bus voltage error is 11.75V which is slightly higher than the specification threshold. According to (11.8), a decrease in the efficiency of the grid inverter or the machine rectifier implies an increase of the error of the DC bus voltage. Thus, as the efficiency of the system has been neglected in the design step in the previous section, the steady state error is expected to be higher than in the simulated system and a proper identification of the system efficiency is needed if a more precise tuning of the controller is wanted.

11.7 Conclusions

A control strategy to allow to keep the wind turbine connected to the grid during voltage sags without the need of communication between the controller of the grid side inverter and the machine rectifier has been presented. Design rules for different design criteria have been proposed and the performance of the control scheme has been successfully tested in both simulation and in an implementation of the controller in a small scale experimental platform.

Chapter 12

Conclusions

12.1 Contributions

The operation of DFIG and VSC under unbalanced voltage sags have been extensively analyzed. Under such condition, the existence of negative sequence grid voltage has been shown to require the current control loops to be able to control at will the negative sequence current. The conventional vector control is not capable to control negative sequence current. Two different alternative control schemes which allow to control the negative sequence current have been analyzed, being the stationary reference frame current control the preferred one as several drawbacks of the dual reference frame vector control have been found.

Regarding the VSC operation under unbalanced voltage sags, several options have been shown to exist when calculating the reference current. One possible method is to inject only positive sequence current, which has been shown to allow to inject the desired power to the grid to keep the DC bus voltage from becoming unstable but implies a ripple in the power output. Another option, which can be found in the literature, is to compensate the oscillation of the power injected to the grid by using negative sequence current. This has been shown to require a higher current which in turn will produce a higher ripple in the power output of the converter. Also, a special situation has been found where this method can not be used as it would require an infinite current. In order to deal with these limitations, two modifications of this method have been presented which allow to avoid this special situation and to compensate the effect of the converter output filter impedance so that the ripple of the power output of the converter is suppressed. However, this method has been shown to require a larger current than the method which only injects positive sequence current. Therefore, either method should be chosen depending on the need to suppress the ripple in the power or to minimize the required current.

Finally, a ride-through strategy for power reduction during voltage sags

Chapter 12 Conclusions

has been presented for PMSG-based wind turbines. This strategy has the advantage that it can be implemented without the need of communication between the generator control and the AC grid connection control, rendering the system more robust to communication failures and enabling the use of new configurations of wind turbines where the machine rectifier and the grid side inverter are located far from each other.

12.2 Future work

The present work have arisen a number of interesting topics for further research:

- Application of the proposed control schemes for VSC to High Voltage Direct Current (HVDC) inverters.
- Extension of the proposed current control designs for islanded and weak grid operation.
- Study of new topologies of inverters for high power applications.

Bibliography

- [1] Z. Lubosny, *Wind Turbine Operation in Electric Power Systems*. Springer, 2003. xix, 12, 13, 32
- [2] “Global wind report: Annual market update 2010,” Global Wind Energy Council, Tech. Rep., 2010. 1
- [3] R. Pena, J. J.C. Clare, and G. Asher, “Doubly fed induction generator using back-to-back PWM converters and its application to variable-speed wind-energy generation,” *IEE Proceedings Electric Power Applications*, vol. 143, no. 3, pp. 231–241, 1996. 2, 16, 69, 77
- [4] J. Morren and S. de Haan, “Ride-through of wind turbines with doubly-fed induction generator during a voltage dip,” *IEEE Transactions on Energy Conversion*, vol. 20, no. 2, pp. 435–441, 2005. 2, 159
- [5] A. D. Hansen and G. Michalke, “Fault ride-through capability of DFIG wind turbines,” *Renewable Energy*, vol. 32, no. 9, pp. 1594–1610, July 2007. 2
- [6] L. Xu and Y. Wang, “Dynamic modeling and control of DFIG-based wind turbines under unbalanced network conditions,” *IEEE Transactions on Power Systems*, vol. 22, no. 1, pp. 314–323, Feb. 2007. 2
- [7] O. Gomis-Bellmunt, A. Junyent-Ferre, A. Sumper, and J. Bergas-Jané, “Ride-through control of a doubly fed induction generator under unbalanced voltage sags,” *IEEE Transactions on Energy Conversion*, vol. 23, pp. 1036–1045, 2008. 2, 138, 143, 148
- [8] S. J. Lee, J. K. Kang, and S. L. Sul, “A new phase detecting method for power conversion systems considering distorted conditions in power system,” in *Proc. Industry Applications Conf.*, 1999. 2
- [9] P. Rodriguez, R. Teodorescu, I. Candela, A. Timbus, M. Liserre, and F. Blaabjerg, “New positive-sequence voltage detector for grid synchronization of power converters under faulty grid conditions,” *Power Electronics Specialists Conference, 2006. PESC '06. 37th IEEE*, pp. 1–7, 18–22 June 2006. 2

Bibliography

- [10] T. K. A. Brekken and N. Mohan, “Control of a doubly fed induction wind generator under unbalanced grid voltage conditions,” *IEEE Transaction on Energy Conversion*, vol. 22, no. 1, pp. 129–135, March 2007. 2, 3
- [11] P. Rioual, H. Pouliquen, and J.-P. Louis, “Regulation of a pwm rectifier in the unbalanced network state using a generalized model,” *IEEE Transactions on Power Electronics*, vol. 11, no. 3, pp. 495–502, May 1996. 3, 138
- [12] E. Spooner and A. Williamson, “Direct coupled, permanent magnet generators for wind turbine applications,” *Electric Power Applications, IEE Proceedings* -, vol. 143, no. 1, pp. 1–8, jan 1996. 3
- [13] F. Blaschke, “The principle of field orientation applied to the new transvector closed-loop control system for rotating field machines,” *Siemens Rev*, vol. 39, pp. 17–220, 1972. 4
- [14] D. W. Novotny and T. A. Lipo, *Vector Control and Dynamics of AC Drives (Vector Control & Dynamics of AC Drives)*. Oxford University Press, USA, 1996. 4
- [15] P. Vas, *Vector Control of AC Machines (Monographs in Electrical and Electronic Engineering)*. Oxford University Press, USA, 1990. 4
- [16] S. Heier, *Grid Integration of Wind Energy Conversion Systems*. John Wiley and Sons, 1998. 7, 8, 9
- [17] J. G. Slootweg, *Wind Power in Power Systems*. Wiley, 2005, ch. Reduced-order Modelling of Wind Turbines, pp. 555–585. 7, 11
- [18] E. Hau, *Wind Turbines: Fundamentals, Technologies, Application, Economics*. Springer, 2005. 7, 8
- [19] H. A. Panofsky and J. A. Dutton, *Atmospheric Turbulence*. Wiley-Interscienc, 1984. 11
- [20] M. Shinozuka and C.-M. Jan, “Digital simulation of random processes and its applications,” *Journal of Sound and vibration*, vol. 25(1), pp. 111–128, 1972. 12
- [21] N. E. Chazly, “Static and dynamic analysis of wind turbine blades using the finite element method,” *Renewable Energy*, vol. 3, no. 6-7, pp. 705–724, 1993. 13

Bibliography

- [22] D. Goodfellow and G. Smith, “Control strategy for variable speed wind energy recovery,” in *Proc. of 8th BWEA Conference*, Cambridge, 1986, pp. 219–228. 16, 161
- [23] R. Leidhold, G. Garcia, and M. Valla, “Maximum efficiency control for variable speed wind driven generators with speed and power limits,” *IECON 02 [Industrial Electronics Society, IEEE 2002 28th Annual Conference of the]*, vol. 1, pp. 157–162 vol.1, Nov. 2002. 16
- [24] P. C. Krause, *Analysis of Electric Machinery*, S. Rao, Ed. McGraw-Hill, 1986. 21, 23, 41, 42, 44
- [25] H. Akagi, Y. Kanazawa, and A. Nabae, “Instantaneous reactive power compensators comprising switching devices without energy storage components,” *IEEE Transaction on Industry Applications*, vol. 20, pp. 625–631, 1984. 27, 58
- [26] C. L. Fortescue, “Method of symmetrical coordinates applied to the solution of polyphase networks,” *Trans. AIEE*, vol. 37, pp. 1027–1140, 1918. 28, 33, 57, 58, 92, 139, 140, 141
- [27] P. Perera, “Sensorless control of permanent-magnet synchronous motor drives,” Ph.D. dissertation, AAU-IET, 2002. 41
- [28] J. Pedra, F. Sainz, L. and Corcoles, R. Lopez, and M. Salichs, “Pspice computer model of a nonlinear three-phase three-legged transformer,” *IEEE Transactions on Power Delivery*, vol. 19, pp. 200–207, 2004. 64
- [29] L. Harnefors and H.-P. Nee, “Model-based current control of ac machines using the internal model control method,” *IEEE Transactions on Industry Applications*, vol. 34, no. 1, pp. 133–141, Jan.-Feb. 1998. 71, 79, 119, 156
- [30] J. Chan, A. Vladimirescu, X.-C. Gao, P. Liebmann, and J. Valainis, “Nonlinear transformer model for circuit simulation,” *Computer-Aided Design of Integrated Circuits and Systems, IEEE Transactions on*, vol. 10, no. 4, pp. 476–482, apr 1991. 86
- [31] B. C. Kuo, *Sistemas de Control Digital*. CECSA, 2000. 114, 124
- [32] S. Skogestad and I. Postlethwaite, *Multivariable Feedback Control*, J. W. . Sons, Ed. Wiley, 2005. 119, 121, 127, 131, 158

Bibliography

- [33] D. N. Zmood and D. G. Holmes, “Stationary frame current regulation of pwm inverters with zero steady-state error,” *IEEE Transactions on Power Electronics*, vol. 18, no. 3, pp. 814–822, May 2003. 120
- [34] C. Sao and P. Lehn, “Control and power management of converter fed microgrids,” *Power Systems, IEEE Transactions on*, vol. 23, no. 3, pp. 1088–1098, 2008. 137
- [35] O. Gomis-Bellmunt, J. Liang, J. Ekanayake, R. King, and N. Jenkins, “Topologies of multiterminal hvdc-vsc transmission for large offshore wind farms,” *Electric Power Systems Research*, vol. 81, pp. 271–281, 2011. 137
- [36] M. H. Bollen, *Understanding Power Quality Problems: Voltage Sags and Interruptions*. Wiley-IEEE Press, 1999. 137, 159
- [37] H. Song and K. Nam, “Dual current control scheme for PWM converter under unbalanced input voltage conditions,” *IEEE Transactions on Industrial Electronics*, vol. 46, no. 5, pp. 953–959, Oct. 1999. 138
- [38] L. Xu, “Coordinated control of dfig’s rotor and grid side converters during network unbalance,” *IEEE Transactions on Power Electronics*, vol. 23, pp. 1041–1049, 2008. 138
- [39] S. Alepuz, S. Busquets-Monge, J. Bordonau, J. Martinez-Velasco, C. C.A. Silva, J. Pontt, and J. Rodriguez, “Control strategies based on symmetrical components for grid-connected converters under voltage dips,” *IEEE Transactions on Industrial Electronics*, vol. 56, pp. 2162–2173, 2009. 138
- [40] Y. Zhou, P. Bauer, J. Ferreira, and J. Pierik, “Operation of grid connected dfig under unbalanced grid voltage condition,” *IEEE Transactions on Energy Conversion*, vol. 24, pp. 240–246, 2009. 138
- [41] J. Hu, Y. He, L. Xu, and B. Williams, “Improved control of dfig systems during network unbalance using pir current regulators,” *IEEE Transactions on Industrial Electronics*, vol. 56, pp. 439–451, 2009. 138
- [42] Z. Li, Y. Li, P. Wang, H. Zhu, C. Liu, and W. Xu, “Control of three-phase boost-type pwm rectifier in stationary frame under unbalanced input voltage,” *Power Electronics, IEEE Transactions on*, vol. 25, no. 10, pp. 2521–2530, oct. 2010. 138

Bibliography

- [43] H. Akagi, E. H. Watanabe, and M. Aredes, *Instantaneous Power Theory and Applications to Power Conditioning (IEEE Press Series on Power Engineering)*. Wiley-IEEE Press, 2007. 139
- [44] A. Junyent-Ferré, O. Gomis-Bellmunt, A. Sumper, M. Sala, and M. Mata, “Modeling and control of the doubly fed induction generator wind turbine,” *Simulation Modelling Practice and Theory*, vol. 18, no. 9, pp. 1365 – 1381, 2010. 147
- [45] M. Karimi-Ghartemani and H. Karimi, “Processing of symmetrical components in time-domain,” *IEEE Transactions on Power Systems*, vol. 22, pp. 572–579, 2007. 148
- [46] D. Montesinos, S. Galceran, A. Sudria, and O. Gomis, “A laboratory test bed for pm brushless motor control,” in *Power Electronics and Applications, 2005 European Conference on*, 0-0 2005, pp. 6 pp. –P.6. 149
- [47] J.-J. E. Slotine and W. Li, *Applied Nonlinear Control*, Wenzel, Ed. Prentice Hall International Inc., 1991. 156
- [48] L. Peng, F. Colas, B. Francois, and Y. Li, “A modified vector control strategy for dfig based wind turbines to ride-through voltage dips,” in *Power Electronics and Applications, 2009. EPE '09. 13th European Conference on*, 2009, pp. 1 –10. 159
- [49] S. Hu, J. Li, and H. Xu, “Comparison of voltage sag generators for wind power system,” in *Power and Energy Engineering Conference, 2009. APPEEC 2009. Asia-Pacific*, 2009, pp. 1 –4. 167

Appendix A

Publications

This chapter presents the publications related to the specific topics of this thesis the author has contributed to.

Journal papers

Published

2011

L. Trilla, O. Gomis-Bellmunt, A. Junyent-Ferre, M. Mata, J. Sanchez, A. Sudria-Andreu. “Modeling and validation of DFIG 3 MW wind turbine using field test data of balanced and unbalanced voltage sags”, *IEEE Trans. Sustainable Energy*, vol. PP, No. 99, May 2011.

2010

A. Junyent-Ferré, O. Gomis-Bellmunt, A. Sumper, M. Sala-Lluma, M. Mata-Dumenjó. “Modeling and Control of the Doubly Fed Induction Generator Wind Turbine”, *Simulation Modelling Practice and Theory*, vol. 18, No. 9, October 2010.

2008

O. Gomis-Bellmunt, A. Junyent-Ferré, A. Sumper, J. Bergas-Jané. “Ride-Through Control of a Doubly Fed Induction Generator Under Unbalanced Voltage Sags”, *IEEE Trans. Energy Conversion*, vol. 23, No.4, December 2008.

Submitted and under revision

A. Junyent-Ferré, O. Gomis-Bellmunt, T.C. Green, D.E. Soto-Sanchez. “Current control reference calculation issues for VSC operation under unbalanced

Appendix A Publications

grid voltages”, *IEEE Trans. Power Electronics.*. Under revision since May 2011.

A. Junyent-Ferré, O. Gomis-Bellmunt, E. Valsera-Naranjo, S. Galceran-Arellano. “Stationary frame control of doubly fed induction wind generators for unbalanced voltage operation”, *Energy Conversion and Management*. Under revision since October 2010.

Other journal contributions

2011

O. Gomis-Bellmunt, A. Junyent-Ferré, A. Sumper, J. Bergas-Jané. “Control of a wind farm based on synchronous generators with a central HVDC-VSC converter”, *IEEE Trans. Power Systems*. Due to publication, available online.

2010

O. Gomis-Bellmunt, A. Junyent-Ferré, A. Sumper, S. Galceran-Arellano. “Maximum generation power evaluation of variable frequency offshore wind farms when connected to a single power converter”, *Applied Energy*, vol. 87, No. 10, October 2010.

E. Valsera-Naranjo, A. Sumper, O. Gomis-Bellmunt, A. Junyent-Ferré. “Pitch Control System Design to Improve Frequency Response Capability of Fixed-Speed Wind Turbine Systems”, *European Transactions on Electrical Power*.

2009

A. Colet-Subirachs, O. Gomis-Bellmunt, D. Clos-Costa, G. Martín-Segura¹, A. Junyent-Ferré, R. Villafáfila-Robles, L. Ferrer-Martí. “Electromechanical Modelling and Control of a micro-wind generation system for isolated low power DC micro grids”, *EPE Journal.*, vol. 20, No.2, Ju. 2010.

Book chapters

O. Gomis-Bellmunt, A. Junyent-Ferré. “Control of doubly fed induction generators under balanced and unbalanced voltage sags”, *Handbook of Renewable Energy Technology*, World Scientific Publishing Co. 2011.

A. Junyent-Ferré, O. Gomis-Bellmunt. “Wind turbine generation systems modelling for integration in power systems”, *Handbook of Renewable Energy Technology*, World Scientific Publishing Co. 2011.

Conference papers

Presented

2010

A. Junyent-Ferré, O. Gomis-Bellmunt, L. Trilla-Romero, M. Mata-Dumenjó. “Operation of DFIG wind turbines under unbalanced voltage sags using stationary frame control”, *EPE Wind Energy Seminar 2010*, Stafford, April 2010.

2009

M. Mata-Dumenjó, J. Sanchez-Navarro, M. Sala-Lluma, Adrià Junyent-Ferré, Oriol Gomis-Bellmunt. “Integrated Simulation of ECO100, a Doubly Fed Induction Generator Wind Turbine”, *China Wind Power 2009*, Beijing, October 2009.

O. Gomis-Bellmunt, A. Junyent-Ferré, A. Sumper, M. Mata-Dumenjó, M. Sala-Lluma. “Control of a doubly-fed induction generator under unbalanced conditions considering the converter limits”, *European Conference on Power Electronics and Applications (EPE 2009)*, Barcelona, September 2009.

M. Mata-Dumenjó, J. Sánchez-Navarro, M. Rosetti, O. Gomis-Bellmunt, A. Junyent-Ferré. “Simulation of Doubly Fed Induction Generator Wind Turbine”, *European Conference on Power Electronics and Applications (EPE 2009)*, Barcelona, September 2009.

Gomis-Bellmunt, A. Junyent-Ferré, A. Sumper, A. Sudria-Andreu. “DFIG control under unsymmetrical conditions”, *EPE Wind Energy Chapter*, Stockholm, April 2009.

2007

A. Junyent-Ferré, O. Gomis-Bellmunt, A. Sumper, M. Sala, M. Mata. “Digital Simulation of Voltage Dip Characteristics of Wind Turbine Systems”,

Appendix A Publications

Int. Conf. Electric Power Quality and Utilisation (EPQU'07), Barcelona, October 2007.

Submitted

A. Junyent-Ferré, O. Gomis-Bellmunt, E. Prieto-Araujo. “Voltage sag ride-through of PMSG wind turbines using droop control stabilization”, *European Conference on Power Electronics and Applications (EPE 2009)*, Birmingham, August 2011.